2000

Towards chip-scale liquid chromatography and high-throughput immunosensing

Jing Ni
Iowa State University

INFORMATION TO USERS

This manuscript has been reproduced from the microfilm master. UMI films the text directly from the original or copy submitted. Thus, some thesis and dissertation copies are in typewriter face, while others may be from any type of computer printer.

The quality of this reproduction is dependent upon the quality of the copy submitted. Broken or indistinct print, colored or poor quality illustrations and photographs, print bleedthrough, substandard margins, and improper alignment can adversely affect reproduction.

In the unlikely event that the author did not send UMI a complete manuscript and there are missing pages, these will be noted. Also, if unauthorized copyright material had to be removed, a note will indicate the deletion.

Oversize materials (e.g., maps, drawings, charts) are reproduced by sectioning the original, beginning at the upper left-hand corner and continuing from left to right in equal sections with small overlaps.

Photographs included in the original manuscript have been reproduced xerographically in this copy. Higher quality 6" x 9" black and white photographic prints are available for any photographs or illustrations appearing in this copy for an additional charge. Contact UMI directly to order.

Bell & Howell Information and Learning
300 North Zeeb Road, Ann Arbor, MI 48106-1346 USA
800-521-0600

Towards chip-scale liquid chromatography and high-throughput immunosensing

by

Jing Ni

A dissertation submitted to the graduate faculty

in partial fulfillment of the requirements for the degree of

DOCTOR OF PHILOSOPHY

Major: Analytical Chemistry

Major Professor: Marc D. Porter

Iowa State University

Ames, Iowa

2000

Graduate College
Iowa State University

This is to certify that the Doctoral dissertation of

Jing Ni

has met the dissertation requirements of Iowa State University

Signature was redacted for privacy.

Major Professor

Signature was redacted for privacy.

For the Major Program

Signature was redacted for privacy.

For the Graduate College

TABLE OF CONTENTS

ACKLOWLEDGEMENTS

I would like to take this opportunity to express my deepest appreciation to several people who have contributed to my growth both personally and professionally during my years in graduate school.

To my major professor Marc Porter, I give my heartfelt appreciation for his guidance in many aspects of my life. Thanks for accepting me to the Porter research group four years ago, where I found my extended family after traveling half of the world. Thanks for understanding me when I didn't know how to express myself, and for always believing in my abilities even when I doubted them.

I want to give special thanks to professor Edward Yeung, who has taken me out of so many research puzzles and brought me the light whenever my research was in the dark. Appreciation is also extended to Professor Dennis Johnson; I want to thank him for his constant encouragement and kindness. From them, I realize the joy of being a great scientist.

I would also like to personally thank Dr. Chuan-Jian Zhong and Dr. Robert Lipert, who gave me much guidance and enjoyment during my exploration in a new research field; and Becky Staedtler, who is always so kind and willing to handle all those last minute jobs with a smile. Thanks are also extended to all the Porter group members, past and present, for the many insightful discussions and their warmest friendships. I can say nothing but wish you all the best in your life. To many of those who work at the Ames Lab machine shop and everyone in the chemistry department machine and glass shops, I thank you for your incredible work in helping me make my designs a reality.

I want to thank my parents for releasing me from the family to fulfill my dream, my uncle and aunt, whom I grew up with, for treating me as their own daughter, and my three

grandparents who are watching over me from heaven. Most importantly, I hope my grandma can recover from her struggle with disease and get healthier every year.

Finally, I would like to thank my husband Zhiyang Du for his understanding, sacrifice, and unconditional love. Thanks for holding our family together through the many difficult times in these years. Without your support, this work would not have been possible.

This work was performed at the Microanalytical Instrumentation Center and Ames Laboratory under Contract No. W-7405-eng-82 with the U.S. Department of Energy. The work is supported by NASA (Grant NAG5-6353) and by an American Chemical Society Analytical Division Summer Fellowship sponsored by Eastman Chemical Co.

ABSTRACT

This work describes several research projects aimed towards developing new instruments and novel methods for high throughput chemical and biological analysis. Approaches are taken in two directions.

The first direction takes advantage of well-established semiconductor fabrication techniques and applies them to miniaturize instruments that are workhorses in analytical laboratories. Specifically, the first part of this work focused on the development of micropumps and microvalves for controlled fluid delivery. The mechanism of these micropumps and microvalves relies on the electrochemically-induced surface tension change at a mercury/electrolyte interface. A miniaturized flow injection analysis device was integrated and flow injection analyses were demonstrated. In the second part of this work, microfluidic chips were also designed, fabricated, and tested. Separations of two fluorescent dyes were demonstrated in microfabricated channels, based on an open-tubular liquid chromatography (OTLC) or an electrochemically-modulated liquid chromatography (EMLC) format. A reduction in instrument size can potentially increase analysis speed, and allow exceedingly small amounts of sample to be analyzed under diverse separation conditions.

The second direction explores the surface enhanced Raman spectroscopy (SERS) as a signal transduction method for immunoassay analysis. It takes advantage of the improved detection sensitivity as a result of surface enhancement on colloidal gold, the narrow width of Raman band, and the stability of Raman scattering signals to distinguish several different species simultaneously without exploiting spatially-separated addresses on a biochip. By labeling gold nanoparticles with different Raman reporters in conjunction with different detection antibodies, a simultaneous detection of a dual-analyte immunoassay was demonstrated. Using this scheme for quantitative analysis was also studied and preliminary

dose-response curves from an immunoassay of a model antigen were obtained. Simultaneous detection of several analytes at the same address can potentially increase the analysis speed, and can further expand the analysis capability of a microarray chip.

GENERAL INTRODUCTION

Dissertation Organization

This work explores new approaches for high throughput chemical and biological analysis. Two approaches, miniaturizing widely used analytical instrumentation and increasing information readout from each analysis, were pursued in parallel to achieve this goal.

The introduction section to this dissertation provides a brief overview of the research that will be described in each of the chapters and a literature review of the on-going research efforts in high throughput analysis. A list of references is attached at the end of this section. Five data chapters, each of which is presented as a separate manuscript with a different research focus, follow the general introduction.

The first three data chapters describe work towards integrating a liquid chromatography (LC) device on a chip. Chapter 1 presents the proof-of-concept design of a mercury pump and summarizes the flow rate, pressure and power consumption results obtained from theoretical modeling as well as experimental characterization. Chapter 2 is an extension of the work in Chapter 1, where the pump is reconfigured to function as valves for sample injection as well as for control of flow rate and direction. In addition, flow injection analyses using a system integrated from such components are also presented. Finally, Chapter 3 summarizes the design and fabrication of a chip-scale electrochemically-modulated LC (EMLC) device, and presents some preliminary separation results obtained from these efforts.

The last two data chapters describe the development of a multianalyte immunoassay readout scheme using surface enhanced Raman scattering (SERS) signals of reporter molecules co-immobilized with biospecific species on gold colloids. The simultaneous

multianalyte detection concept is demonstrated in Chapter 4, and an in-depth study of this approach for quantitative analysis is presented in Chapter 5. The dissertation ends with general conclusions regarding the work presented in each chapter and speculates on possible extensions.

Literature Review

The human genome initiative has increased significantly the rate at which disease-causing genes are being mapped and sequenced.[1] With the mapping of the human genome proceeding rapidly, scientists also recognize the need to characterize the corresponding gene products, namely proteins, in order to better understand the chemical composition of biological systems. The new term, proteome, describes all the proteins expressed by a genome, and proteomics defines the large-scale study of proteome.[2, 3] The combined genomic and proteomic information is used by the pharmaceutical industry to search for new drug targets and to screen a library of drug candidates against a certain disease.[4] Both genome and proteome as well as drug library contain enormous quantities of information. Therefore robust, reproducible, and accurate analysis protocols are required in the field of genomic and proteomic mapping to locate the gene or protein mutations that cause the disease, and in the field of drug screening to discover a drug that targets these mutations.

To obtain and handle this massive information, new analytical instrumentation and analysis methods have undergone rapid development in the past two decades. Among these new methods, massively parallel processing by using extremely miniaturized analytical systems[5-9] and massively parallel readout[10-12] by using multiple labels are two major approaches that have appeared most promising for providing the necessary level of throughput in the DNA, protein, and drug analysis realms.

Massively Parallel Processing

Research in many analytical analyses and clinical assays has been moving rapidly towards the development and use of miniaturized systems, which allows a limited amount of sample to be analyzed under diverse conditions and enables researchers to obtain more complete characterization of the sample. Miniaturized analytical systems, also commonly referred to as "labs-on-chip", can be classified generally into two categories: microfluidics, based on microchannel networks,[13] and microarrays, based on a microtitre plate format.

These systems have several potential advantages, including:

(i) down-sizing of instruments, which in some cases permits true portability for point-of-care testing;

(ii) increased automation with decreased sample handling, of particular importance with infectious samples;

(iii) increased throughput and efficiency; and

(iv) markedly decreased consumption of expensive reagents and of small-quantity samples.

Micromachining and microfabrication techniques have been applied to build the miniature elements in these systems. The techniques, based on decades of advancements in integrated circuit (IC) design, have produced low cost ICs and made personal computers affordable. There are now also established processes for the fabrication of micron-sized structures, sensors, and actuators in a booming research field called microelectromechanical systems (MEMS).[14] More recently, the traditional IC fabrication techniques, such as oxidation, photolithography, bulk and surface micromachining, and thin-film deposition and bonding, have been either directly adopted or further developed to pattern surfaces with dense arrays of biomolecules in microarray fabrication or to build three-dimensional fluidic networks in microfluidic devices.[15, 16]

Microfluidics

The demand for the high throughput analysis of complex mixtures has led technology towards the development and application of microfluidic devices, in which chemical or medical analyses are conducted in microchannel networks. Efforts are not only limited to the miniaturization of existing, widely used analytical instruments, rather, miniaturization of flow devices also opens a new research field in fluidics since the behavior of the fluids in microfabricated channels is much different from that observed at conventional scale.[17-19] For example, the Reynolds number (Re) in a microchannel is usually below 200, suggesting a laminar flow pattern in these channels, rather than turbulent as found in large pipes. Therefore, special designs and considerations are necessary to account for this unique flow characteristic when developing novel fluidic sensors and analyzers at extremely small dimensions. The ultimate goal of these efforts is to incorporate all sample processing steps into an analytical system, so called "micro total analysis system (μTAS)", to realize a reduction in sample and reagent consumption, a fast analysis time, and a large output of information.[6, 20, 21]

Device Components. In order to realize automatic chemical analysis and achieve effective sample handling, treatment and detection, the development and integration of device components are necessary.[22] Figure 1 shows a basic fluidic flow-based analytical system consisting of microfabricated flow channels, miniaturized chemical sensors or detectors, and flow control devices, including micropumps and microvalves.

Micropumps. The classification of micropumps is somewhat arbitrary. Figure 2 distinguishes them by the presence or absence of mechanical check valves, and by actuation principles. For micropumps containing check valves, the momentum of a piezoelectric,[23, 24] thermal pneumatic,[25] or electrostatic[26] actuations is transferred to

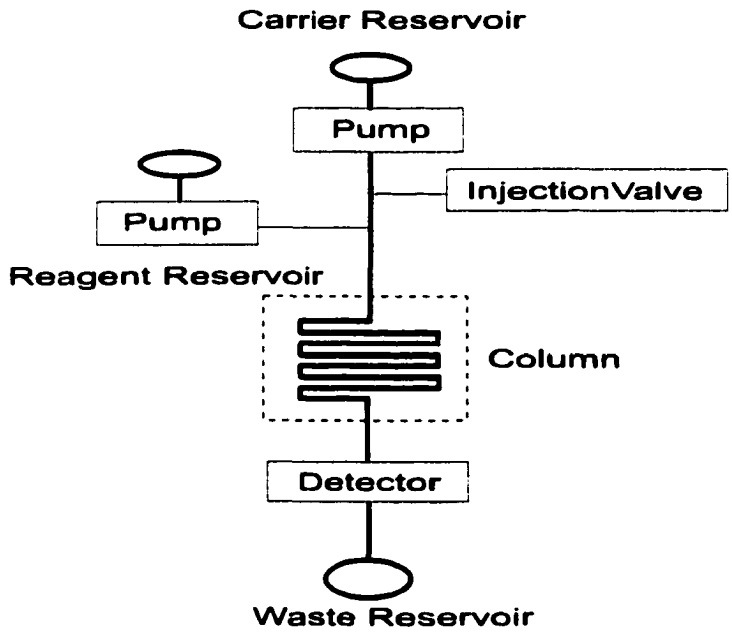

Figure 1. Schematic representation of a microfluidic device.

the solution, and causes fluid flow. However, continuous unidirectional fluidic flow can only be achieved from such pumps after connecting with check valves.

The diffuser pump consists of an actuated pump chamber and a pair of nozzle/diffuser elements that take care of a rectifying action. The principle of operation relies on the change in pressure when the fluid passing different channel geometries, which results in preferential flow in one direction.[27, 28] Since no mechanical movement is involved to realize the check valve function, the nozzle/diffuser elements are often referred as valveless valves.[27, 28]

There is a variety of micropumps that realize unidirectional fluid delivery without the use of check valves. Bubble-powered pumps rely on the repeated growth and collapse of a single bubble to push small amounts of liquid through narrow channels.[29] Electrohydrodynamic pumping (EHD) is performed by the large electric fields developed between two electrodes that are positioned orthogonal to the flow direction, or by

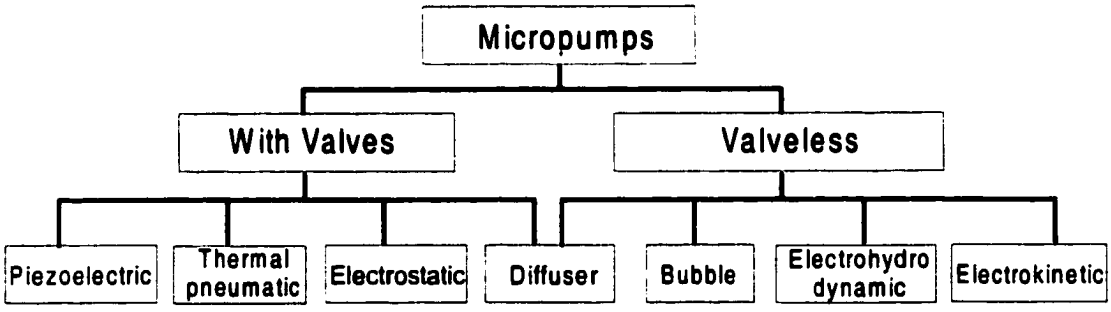

Figure 2. Micropump classification.

induction.[30] Electrokinetic pumping has been, to date, the most successful mechanism for achieving controlled fluidic delivery in miniaturized channels. It relies on the presence of a surface charge on glass capillaries, which causes counter ions in the fluid to align along the inside of the capillary. Therefore, when a high voltage is applied along the longitudinal direction of the flow channel, the mobile counter ions move and take the rest of the fluid column with them.[31]

Microvalves. Microvalves can be classified into two categories: active microvalves (with an actuator) and passive microvalves (without an actuator).[16, 32] They may be part of a micropump as check valves, or work independently to switch flow direction or to control flow rate.

Active microvalves are usually used for control of flow rate and for sample injection. Although most all microactuators have been adapted to build gas control microvalves, only a few active microvalves have been developed for controlling liquid flow based on piezoelectric[24, 33] or thermopneumatic[34] actuation. Recently, the unique material properties of shape-memory alloys[35, 36] and pH- or charge-sensitive hydrogels[37, 38] have been exploited to fabricate new types of microactuators for microvalves as well as for micropump devices.

In contrast, passive microvalves are used mainly as check valves and are attached to each side of a micropump. Several types of operating schemes have been developed, which rely on microstructures such as a simple bulk silicon cantilever,[39] a suspended polysilicon round disk,[40] or a molded silicone rubber float.[41]

Microchannels. Another passive element in a microfluidic device is the microchannel network. Microfluidic channels have been fabricated in different kinds of materials, ranging from silicon,[42, 43] glass,[44] to a variety of polymers.[45] Silicon and glass machining techniques are adopted mainly from the IC industry. Indeed, the first commercial microfluidic-based lab-on-a-chip device (HP 2100 Bioanalyzer) was built on a glass substrate based on the techniques developed by Caliper Technologies, Inc., to perform DNA analysis. Figure 3 shows a photograph of one of the microfluidic chips made by Caliper.

Recently, more attention has been given to polymeric substrates. Polymers differ from one another in their mechanical properties, optical characteristics, temperature stability,

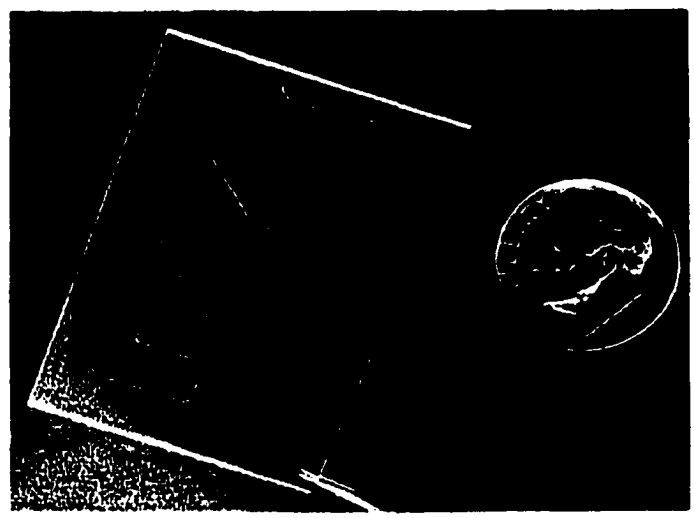

Figure 3. Microfluidic chip for DNA analysis. Reproduced with permission from www.calipertech.com

and chemical resistivity. As a consequence, it is believed that there is a suitable polymer material for nearly every application. Traditional photolithography techniques have been exploited to directly build microstructures into different photoresist polymers, including SU-8, photosensitive polyimide, and photosensitive polymethylmethacrylate (PMMA). Replication technologies, such as hot embossing, injection molding, and casting further expand the applicable substrates to low cost materials like polycarbonate (PC), polypropylene (PP), and polystyrene (PS).[46-49] These fabrication technologies, together with the substrate materials, offer the opportunity for low-cost manufacturing, which is the secret of commercial success. In fact, a start-up biotech company, Aclara BioScience, Inc. is building its major market in plastic microfluidic chips fabricated from the replication process that is shown in Figure 4. Laser-based direct writing[50, 51] and stereolithography techniques are also being applied to fabricate polymer-based structure and devices.[45]

Microfilters. Microfilters are sometimes fabricated within a microfluidic channel to select particulate materials of a certain size within a sample. The deep reactive ion etching

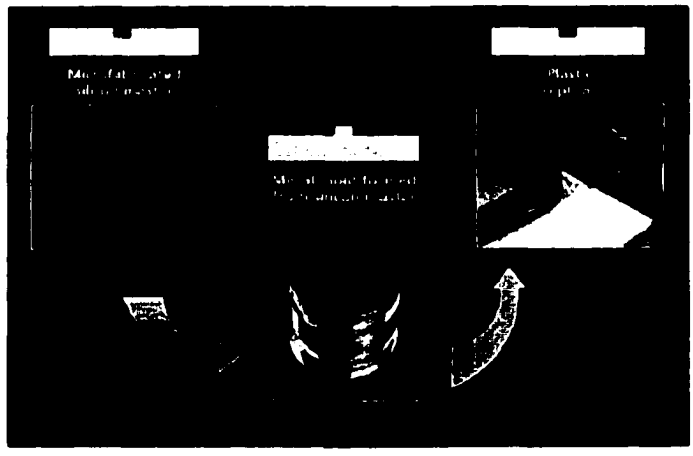

Figure 4. The replication process used by Aclara BioScience, Inc to fabricated plastic microfluidic chips. Reproduced with permission from www.aclara.com

(DRIE) technique was used to create a network of intersecting 1.5 x 10 μm channels in quartz.[52] When placed at the bottom of reservoirs with a side exit, this channel network behaved as a lateral percolation filter and was used to filter cells in a flow stream. Microsieves with sub-micron (260 nm) pore sizes were also made using multiple laser interference lithography in a 100 nm thick silicon nitride layer.[53]

Micromixers. Solution mixing within small channels is usually a big problem caused by the absence of turbulence in the flow with low Re (<100). The laminar flow characteristic of microfluidics suggests that diffusion dominates the mixing process, which is much slower than turbulence caused mixing. To specifically account for this flow characteristic in microfluidic devices, micromixers have been designed and fabricated. Bessoth and co-workers presented a micromixer for the laminar flow regime based on the principle of flow lamination.[54] The structure is made from a glass/silicon/glass sandwich and the layout of the micromixer is based on the principle of distributive mixing. A similar principle was used by Schwesinger and co-workers for building static micromixers, consisting of two structured silicon wafers bonded together.[55]

Detectors. Conventional fluorescence microscopes, equipped with CCD cameras, have been used widely to observe and detect analytical results obtained from most microfabricated devices.[56] However, miniaturized detectors that can be integrated within miniaturized systems are usually in the form of microelectrodes,[57-61] where detection is based on the electrochemical properties of the analytes in a sample. Optical fibers have also been integrated within the detection region of flow channels to perform absorbance or fluorescence-based detection.[62, 63] Other types of chemical sensors, such as surface acoustic wave devices (SAW),[64] were microfabricated, but their applicability in μTAS has not been demonstrated.

Analytical Devices. In the past two decades, scientists have been trying to miniaturize the analytical systems that are the workhorses in the analytical laboratories. In 1979, researchers at Stanford University fabricated a gas chromatographic air analyzer, the first chip scale analytical device fabricated on a silicon wafer.[65] A miniaturized flow injection analysis (FIA) system was also integrated on a plastic platform the size of a credit card.[66] Some efforts were given towards building chip-scale liquid chromatographs (LC), but more success has been achieved when using electrokinetic pumping for fluidic delivery[67-69] rather than with pressure driven LC systems.[70, 71] A micromachined Coulter counter[72] was demonstrated in 1999, and miniaturized cell sorting devices were also integrated on chip.[73-75] Moreover, the key component of a mass spectrometer, the mass analyzer, has been miniaturized by the Jet Propulsion Laboratory.[76] Both quadrupole and magnetic sector types of mass analyzers were reduced to a size less than ten centimeters.

Among miniaturized analytical devices, capillary electrophoresis (CE) chips[77-80] have been applied most widely in practical applications such as DNA sequencing[81, 82] and immunoassays.[83-85] The simple hardware requirements for fluidic control and delivery facilitate the miniaturization of a CE system. Almost every form of CE, including capillary zone electrophoresis (CZE),[86] capillary gel electrophoresis (CGE),[87-90] and micellar electrokinetic chromatography (MEKC),[91] has been transferred successfully to planar chips. The major advantage of chip CE over capillary CE is the ability to make zero dead volume interconnects, which reduce tremendously band broadening during the sample injection step in a CE experiment. Another advantage is the simplicity of fabricating channel arrays on the chip versus making capillary arrays, which facilitates the extension from a single device to parallel processing devices. However, the size of a CE chip limits the maximum length of the separation channel, which limits ultimately the separation power of these devices. In

applications such as sequencing DNA fragments with more than 1000 base pairs, capillary-based CE systems are still more beneficial than chip-based electrophoresis devices. Ongoing research efforts are devoted to overcoming this size limitation with chip CE devices.

Other Applications. Microfabricated fluidic devices have not only been used to perform chemical and biological analysis, but also as microreactors to carry out chemical syntheses.[92] For example, the temperature-dependent polymerase chain reaction (PCR) was carried out by flowing reactants continuously in a microfluidic channel that crossed different temperature zones on a microchip. Rather than changing the temperature of the reactants in a stationary vial, this microfluidic-based reactor has been considered as a breakthrough towards an integrated DNA total analysis device.[93]

Elastomeric microfluidic networks have been used for surface patterning by localizing chemical reactions between biomolecules and the surface. For example, different antibodies were delivered precisely onto different locations of a surface using an array of microfluidic channels. Immunoassays were then successfully performed on such surfaces.[94, 95] Similar microfluidic networks have been used for the patterned deposition of cells as well.[96]

Microarrays

High-density microarray devices are based on a microtitre plate-type format and achieve high information throughput by massively parallel processing.[9, 97] Such devices have numerous spatially separated addresses, where each is labeled with a different type of probes. For example, DNA arrays are comprised of short strands of immobilized DNA ("probe") sequences prepared on a planar support. Samples of unknown DNA, usually

labeled with fluorescent dye, can be analyzed by monitoring the sequence-specific binding ("hybridization") to the arrays. Detailed information about the sample sequence is related to the location (i.e., address) of the probe on the planar support.[98] DNA microarray devices have been used in gene expression, sequencing, and mutation detection,[98-103] and are commercially available through companies, such as Affymetrix, Inc. and Nanogen Inc. The development of microarrays capable of performing proteomic analysis has also appeared as an extension of DNA chips. In this case, different proteins, such as antibodies or enzymes, are used as probes and are immobilized to different addresses on the chip.[104]

One of the essential steps in building these devices is to fabricate arrays of sufficient size and complexity with the highest possible density of encoded sequence information. The technology involved in the definition of these high-density spatially-separated addresses is usually used to differentiate the fundamental operational platform.

Light-Directed Synthesis. DNA arrays are fabricated at Affymetrix through the light-directed synthesis process, termed as "very large-scale immobilized polymer synthesis".[105-107] In this technique, 5'-terminal protecting groups of the growing oligonucleotide chains are selectively removed from the sequence in predefined regions of a glass support by controlled exposure to light through photolithographic masks. Figure 5 illustrates the overall fabrication process. It begins with a planar glass or silica substrate, which has been covalently modified with linker molecules bearing a terminal photolabile protecting group. Specific regions of the surface, defined by a mask, are exposed to light, causing the selective removal of protecting groups from the linkers in the illuminated regions. The activated linkers react locally with one of four similarly protected nucleotide building blocks (dA, dG, dC, or dT) supplied in the reaction mixture. Cycles of photo-deprotection and nucleotide addition are repeated to build the desired array of sequences.

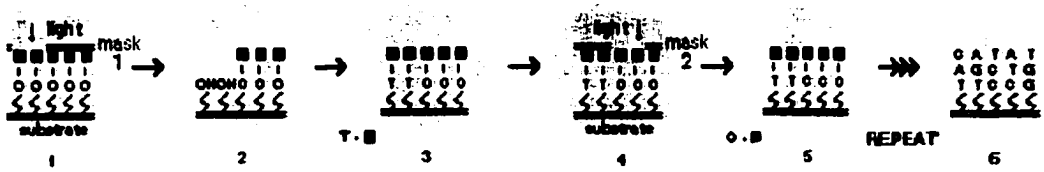

Figure 5. Schematic representation of light-directed synthesis. Reproduced with permission from www.affymetrix.com

This strategy is considered to be the most efficient combinatorial scheme for building high-density arrays.

Electronic Addressing. Nanogen exploits the polarity of DNA for localization on charged microelectrode arrays, a technique named "electronic addressing".[108] In this technique, the pre-synthesized, negatively-charged DNA probes under the effect of an electric field move close to a set of positively-biased electrodes and are chemically bound to these sites. The microchip is then washed and another solution of distinct DNA probes can be added. Repetition of the cycle with appropriate electrode-biasing, therefore, builds sequentially a large array containing distinct sites of sequence-specific DNA probes. Figure 6 shows five sets of different capture probes that have been electronically addressed to the microchip. In contrast to the light-directed synthesis approach of Affymetrix, this technique is more versatile and cost-effective when building custom arrays with less addresses.

Some companies also use automatic array spotters to directly deliver different pre-synthesized DNA probes to specific locations on the substrates. The array spotter uses state-of-the-art XYZ positioning instrument to provide precise and high-speed manufacturing. Figure 7 shows the central part of the array spotter used at Molecular Dynamics, Inc. It relies on 12 capillary pens to deposit nanoliter volumes of samples at a

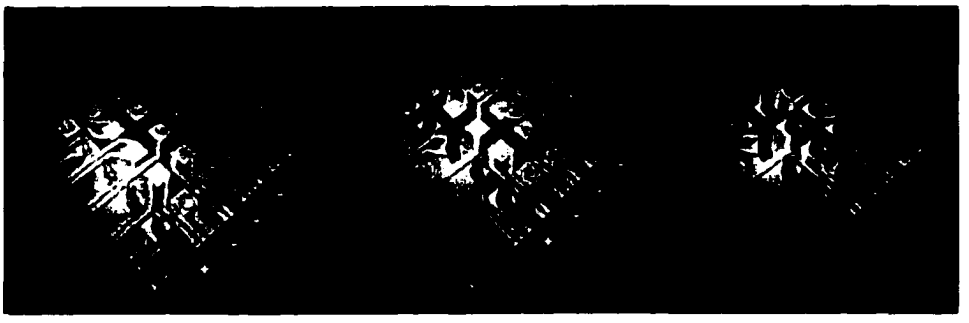

Figure 6. Schematic representation of electronic-addressing. Reproduced with permission from www.nanogen.com

high density onto coated glass slides. Clearly, the accuracy and precision of the spotter movement and the surface modification of the substrate are critical factors in determining the array density.

Massively Parallel Readout Methods

Instead of reducing the size of the analytical instrument, i.e., the "hardware" used in the analysis, massively parallel readout methods increase the information throughput obtained from conventional instruments by devising new methodologies of the analyses, i.e., the "software". This is done by using multiple labels for the simultaneous detection of multiple species in an unknown sample mixture.[10] This approach is particularly beneficial for clinical applications, since many immunoassays (e.g., the diagnosis of myocardial infarction, screening of cancer markers, and allergen tests) require the rapid, concomitant determination of several analytes to formulate a diagnosis. The multianalyte detection technique provide advantages including work simplification, increased test throughput and reduced overall cost per test.[109].

To perform the analysis, the labeled analyte is first separated from the sample and then analyzed by a variety of different approaches,[110] including scintillation counting,[11]

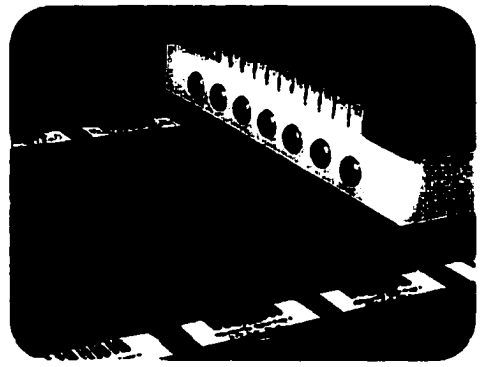

Figure 7. The array spotter used by Molecular Dynamics, Inc. for DNA array fabrication. Reproduced with permission from www.mdyn.com

fluorescence,[111, 112] absorption,[113] electrochemistry,[12] chemiluminescence,[114] Rayleigh scattering,[115] and Raman scattering.[116-118] The identification of the unknown sample is established based on the observed signatures of different labels. Figure 8 conceptualizes the procedure of a multianalyte enzyme-linked immunosorbant assay (ELISA). Obviously, the more labels that can be distinguished simultaneously, the more information can be obtained from a single readout. Indeed, ongoing research efforts in this field have been devoted to the development of different detection schemes and to the search for different groups of labels.

Several requirements need to be considered when choosing labels for simultaneous multianalyte detection. First, the analytical signal from a label should be of sufficient strength so that the assay can provide adequate sensitivity. Second, the signals from different labels should have minimal overlap to ensure accurate detection. Ideally, the signals should be insensitive to the environmental conditions, such as humidity and oxygen concentration, in which the analysis is performed. This characteristic broadens the applicability of the technique and ensures the reproducibility of the measurement. Finally, the hardware required for inducing and detecting signals from different labels should be as

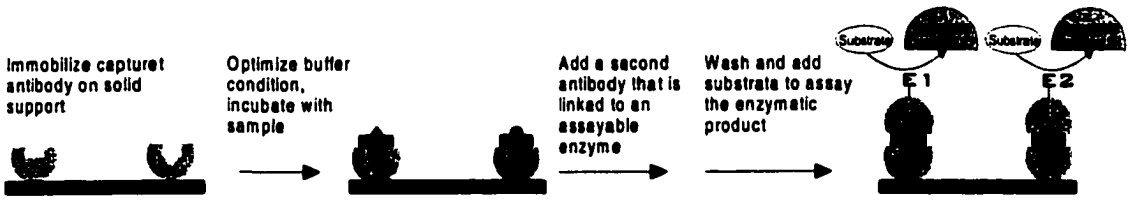

Figure 8. Schematic illustration of a dual-analyte ELISA

simple as possible. Of the vast selection of readout schemes and labels, fluorescent-based multianalyte detection using different fluorescence dye molecules as labels have been by far the most widely used to address this need. This situation is primarily because of the availability of distinguishable labels and the detection sensitivity of this technique.[10]

To summarize, the demand for high-throughput and cost effective analysis of complex mixtures has focused a great deal of interest on the development and application of compact, miniaturized fluidic devices, high-density microarrays, and parallel readout schemes. Collectively, the combined efforts in these fields will lead rapidly to the elucidation of the underlying mechanisms of disease, resulting in the discovery of novel drugs, vaccines and diagnostic methods.

References

(1) Ryu, D. D. Y.; Nam, D.-H. *Biotechnol. Prog.* **2000**, *16*, 2.

(2) Hancock, W.; Apffel, A.; Chakel, J.; Hahnenberger, K.; Choudhary, G.; Traina, J. A.; Pungor, E. *Anal. Chem.* **1999**, *71*, 742A.

(3) Figeys, D. *Curr. Opin. Mol. Ther.* **1999**, *1*, 685.

(4) Kniss, R. *Am. Lab.* **1998**, *30*, 40.

(5) Knapp, M. R.; Sundberg, S.; Kopf-Sill, A.; Nagle, R.; Gallagher, S.; Chow, C.; Wada, G.; Nikiforov, T.; Cohen, C.; Parce, J. W. *Am. Lab.* **1998**, *30*, 22.

(6) Manz, A.; Graber, N.; Widmer, H. M. *Sens. Actuators* **1990,** *B1*, 244.

(7) Manz, A. In *J. Pharm. Pharmacol.*, 1998; Vol. 50, pp 42.

(8) Mastrangelo, C. H. *Adv. Sci. Technol.* **1999,** *26*, 465.

(9) Schena, M. *Microarray Biochip Technology*, 2000.

(10) Kricka, L. J. In *Immunoassay*; Diamandis, E. P., Christopoulos, T. K., Eds.; Academic Press: New York, 1996, pp 389.

(11) Gutcho, S.; Mansbach, L. *Clin. Chem.* **1977,** *23*, 1609.

(12) Hayes, F. J.; Halsall, H. B.; Heineman, W. R. *Anal. Chem.* **1994,** *66*, 1860.

(13) Chau, C.; Banerjee, S.; Seul, M. *Proc. SPIE-Int. Soc. Opt. Eng.* **1999,** *3877*, 36.

(14) Ho, C.-M.; Tai, Y.-C. *J. Fluids Eng.* **1996,** *118*, 437.

(15) Gravesen, P.; Branebjerg, J.; Jensen, O. S. *J. Micromech. Microeng.* **1993,** *3*, 168.

(16) Shoji, S.; Esashi, M. *J. Micromech. Microeng.* **1994,** *4*, 157.

(17) Zemel, J. N.; Furlan, R. In *Handb. Chem. Biol. Sens.*, 1996, pp 317.

(18) Zengerle, R.; Richter, M. *J. Micromech. Microeng.* **1994,** *4*, 192.

(19) Guckel, H. In *Philos. Trans. R. Soc. London, Ser. A*, 1995; Vol. 353, pp 355-66.

(20) Van Den Berg, A.; Lammerink, T. S. J. *Top. Curr. Chem.* **1998,** *194*, 21.

(21) Harrison, D. J.; Berg, A. v. d. *Proceedings of the Micro Total Analysis Systems '98*; Kluwer Academic: Banff, Canada, 1998.

(22) Howitz, S. *BioMethods* **1999,** *10*, 31-73.

(23) Van Lintel, H. T. G.; Van De Pol, F. C. M.; Bouwstra, S. *Sens. Actuators* **1988,** *15*, 153.

(24) Shoji, S.; Nakagawa, S.; Esashi, M. *Sens. Actuators* **1990,** *A21*, 189.

(25) Van De Pol, F. C. M.; Van Lintel, H. T. G.; Elwenspoek, M.; Fluitman, J. H. J. *Sens. Actuators* **1990,** *21*, 198.

(26) Zengerle, R.; Geiger, W.; Richter, M.; Ulrich, J.; Kluge, S.; Richter, A. *Sens. Actuators* **1995,** *A47*, 557-61.

(27) Olsson, A.; Enoksson, P.; Stemme, G.; Stemme, E. *J. Microelectromech. Sys.* **1997,** *6*, 161.

(28) Stemme, E.; Stemme, G. *Sens. Actuators* **1993,** *A39*, 159-67.

(29) Jun, T. K.; Kim, C.-J.; Ho, C.-M. In *Tech. Dig.*, 1996, pp 144.

(30) Bart, S. F.; Tavrow, L. S.; Mehregany, M.; Lang, J. H. *Sens. Actuators* **1990,** *A21*, 193.

(31) Manz, A.; Effenhauser, C. S.; Burggraf, N.; Harrison, D. J.; Seiler, K.; Fluri, K. *J. Micromech. Microeng.* **1994,** *4*, 257.

(32) Shoji, S. *Top. Curr. Chem.* **1998,** *194*, 163-188.

(33) Shoji, S.; Esashi, M.; Matsuo, T. *Sens. Actuators* **1988,** *14*, 101.

(34) Zdeblick, M. J.; Anderson, R.; Jankowski, J.; Kline-Schoder, B.; Christel, L.; Miles, R.; Weber, W. *Solid-State Sensor and Actuator Workshop* **1994**, 251.

(35) Benard, W.; Kahn, H.; Huff, M. *A TiNi shape-memory alloy actuated micropump with fluid isolation*, 1997.

(36) Kohl, M.; Skrobanek, K. D.; Miyazaki, S. *Sens. Actuators* **1999,** *A72*, 243-250.

(37) Baughman, R. H.; Shacklette, L. W.; Elsenbaumer, R. L.; Plichta, E. J.; Becht, C. *Top. Mol. Organ. Eng.* **1991,** *7*, 267.

(38) Beebe, D. J.; Moore, J. S.; Bauer, J. M.; Yu, Q.; Liu, R. H.; Devadoss, C.; Jo, B.-H. *Nature* **2000,** *404*, 588.

(39) Tiren, J.; Tenerz, L.; Hok, B. *Sens. Actuators* **1989,** *18*, 389.

(40) Esashi, M.; Shoji, S.; Nakano, A. *Sens. Actuators* **1989,** *20*, 163.

(41) Shoji, S.; van der Schoot, B. H.; de Rooij, N. F.; Esashi, M. *Sens. Actuators* **1992,** *A32*, 335.

(42) Kovacs, G. T. A.; Petersen, K.; Albin, M. *Anal. Chem.* **1996,** *38*, 407A.

(43) Mastrangelo, C. H.; Tang, W. C. In *Semiconductor Sensors*; Sze, S. M., Ed.; John Wiley and Sons: New York, 1994, pp 17.

(44) Stjernstrom, M.; Roeraade, J. *J. Micromech. Microeng.* **1998,** *8*, 33-38.

(45) Becker, H.; Gartner, C. *Electrophoresis* **2000,** *21*, 12-26.

(46) Chiang, Y.-M.; Bachman, M.; Chu, C. Y.; Li, G. *Proc. SPIE-Int. Soc. Opt. Eng.* **1999,** *3877*, 303-311.

(47) Martynova, L.; Locascio, L. E.; Gaitan, M.; Kramer, G. W.; Christensen, R. G.; MacCrehan, W. A. *Anal. Chem.* **1997,** *69*, 4783-4789.

(48) Martin, P. M.; Matson, D. W.; Bennett, W. D.; Lin, Y.; Hammerstrom, D. J. *J. Vac. Sci. Technol.* **1999,** *A17*, 2264-2269.

(49) Becker, H.; Heim, U.; Roetting, O. In *Proc. SPIE-Int. Soc. Opt. Eng.*, 1999; Vol. 3877, pp 74-79.

(50) Martin, P. M.; Matson, D. W.; Bennett, W. D.; Stewart, D. C.; Lin, Y. *Proc. SPIE-Int. Soc. Opt. Eng.* **1999,** *3680*, 826-833.

(51) Martin, P. M.; Bennett, W. D.; Hammerstrom, D. J.; Johnston, J. W.; Matson, D. W. *Proc. SPIE-Int. Soc. Opt. Eng.* **1997,** *3224*, 258-265.

(52) He, B.; Tan, L.; Regnier, F. *Anal. Chem.* **1999,** *71*, 1464-1468.

(53) Van Rijn, C. J. M.; Nijdam, W.; Kuiper, S.; Veldhuis, G. J.; Van Wolferen, H.; Elwenspoek, M. *J. Micromech. Microeng.* **1999,** *9*, 170.

(54) Bessoth, F. G.; deMello, A. J.; Manz, A. *Anal. Commun.* **1999,** *36*, 213.

(55) Schwesinger, N.; Frank, T.; Wurmus, H. *J. Micromech. Microeng.* **1996,** *6*, 99-102.

(56) Jiang, G.; Attiya, S.; Ocvirk, G.; Lee, W. E.; Harrison, D. J. *Biosens. Bioelectron.* **2000,** *14*, 861-869.

(57) Cohen, A. E.; Kunz, R. R. *Sens. Actuators* **2000,** *B62*, 23.

(58) Sullivan, M. G.; Utomo, H.; Fagan, P. J.; Ward, M. D. *Anal. Chem.* **1999,** *71*, 4369.

(59) Liu, Z.; Niwa, O.; Kurita, R.; Horiuchi, T. *Anal. Chem.* **2000,** *72*, 1315.

(60) Rossier, J. S.; Roberts, M. A.; Ferrigno, R.; Girault, H. H. *Anal. Chem.* **1999,** *71*, 4294.

(61) Zhelyaskov, V. R.; Milne, E. T.; Hetke, J. F.; Morris, M. D. *Appl. Spectrosc.* **1995,** *49*, 1793.

(62) Liang, Z.; Chiem, N.; Ocvirk, G.; Tang, T.; Fluri, K.; Harrison, D. J. *Anal. Chem.* **1996,** *68*, 1040.

(63) Brahmasandra, S. N.; Johnsona, B. N.; Websterc, J. R.; Burke, D. T.; Mastrangeloc, C. H.; Burns, M. A. *Proc. SPIE-Int. Soc. Opt. Eng.* **1998,** *3515*, 242.

(64) Shiokawa, S.; Matsui, Y. *Mater. Res. Soc. Symp. Proc.* **1995,** *360*, 53-64.

(65) Terry, S. C.; Jerman, J. H.; Angell, J. B. *IEEE Trans. Elec. Dev.* **1979,** *26*, 1880.

(66) Schoot, B. H.; Jeanneret, S.; Van Den Berg, A.; de Rooij, N. F. *Sens. Actuators* **1993,** *B13*, 333.

(67) Oleschuk, R. D.; Shultz-Lockyear, L. L.; Ning, Y.; Harrison, D. J. *Anal. Chem.* **2000,** *72*, 585-590.

(68) Jacobson, S. C.; Hergenroder, R.; Koutny, L. B.; Ramsey, J. M. *Anal. Chem.* **1994,** *66*, 2369.

(69) Kutter, J. P.; Jacobson, S. C.; Matsubara, N.; Ramsey, J. M. *Anal. Chem.* **1998,** *70*, 3291-3297.

(70) He, B.; Tait, N.; Regnier, F. *Anal. Chem.* **1998,** *70*, 3790.

(71) Manz, A.; Miyahara, Y.; Miura, J.; Watanabe, Y.; Miyagi, H.; Sato, K. *Sens. Actuators* **1990,** *B1*, 249.

(72) Koch, M.; Evans, A. G. R.; Brunnschweiler, A. *J. Micromech. Microeng.* **1999,** *9*, 159-161.

(73) Yang, J.; Huang, Y.; Wang, X.-B.; Becker, F. F.; Gascoyne, P. R. C. *Anal. Chem.* **1999,** *71*, 911-918.

(74) Cheng, J.; Sheldon, E. L.; Wu, L.; Heller, M. J.; O'Connell, J. P. *Anal. Chem.* **1998,** *70*, 2321.

(75) Fiedler, S.; Shirley, S. G.; Schnelle, T.; Fuhr, G. *Anal. Chem.* **1998,** *70*, 1909.

(76) Stalder, R. E.; Boumsellek, S.; Van Zandt, T. T.; Kenny, T. W.; Hecht, M. H.; Grunthaner, F. E. *J. Vac. Sci. Technol.* **1993,** *12*, 2554.

(77) Deyl, Z.; Miksik, I.; Tagliaro, F. *Forensic Sci. Int.* **1998,** *92*, 89-124.

(78) Effenhauser, C. S.; Bruin, G. J. M.; Paulus, A. *Electrophoresis* **1997,** *18*, 2203-2213.

(79) Manz, A.; Verpoorte, E.; Effenhauser, C. S.; Burggraf, N.; Raymond, D. E.; Widmer, H. M. *Fresenius' J. Anal. Chem.* **1994,** *348*, 567-71.

(80) Regnier, F. E.; He, B.; Lin, S.; Busse, J. *Trends Biotechnol.* **1999,** *17*, 101-106.

(81) Kambara, H. *Curr. Top. Anal. Chem.* **1998,** *1*, 21-36.

(82) Paulus, A. *Am. Lab.* **1998,** *30*, 59-62.

(83) Chiem, N. H.; Harrison, D. J. *Clin. Chem.* **1998,** *44*, 591-598.

(84) Hadd, A. G.; Raymond, D. E.; Halliwell, J. W.; Jacobson, S. C.; Ramsey, J. M. *Anal. Chem.* **1997,** *69*, 3407-3412.

(85) Hadd, A. G.; Jacobson, S. C.; Ramsey, J. M. *Anal. Chem.* **1999,** *71*, 5206-5212.

(86) Jacobson, S. C.; Hergenroder, R.; Koutny, L. B.; Ramsey, J. M. *Anal. Chem.* **1994,** *66*, 1114-18.

(87) Woolley, A. T.; Sensabaugh, G. F.; Mathies, R. A. *Anal. Chem.* **1997,** *69*, 2181.

(88) Simpson, P. C.; Roach, D.; Woolley, A. T.; Thorsen, T.; Johnston, R.; Sensabaugh, G. F.; Mathies, R. A. *Proc. Natl. Acad. Sci. U. S. A.* **1998,** *95*, 2256-2261.

(89) Shi, Y.; Simpson, P. C.; Scherer, J. R.; Wexler, D.; Skibola, C.; Smith, M. T.; Mathies, R. A. *Anal. Chem.* **1999,** *71*, 5354-5361.

(90) Scherer, J. R.; Kheterpal, I.; Radhakrishnan, A.; Ja, W. W.; Mathies, R. A. *Electrophoresis* **1999,** *20*, 1508-1517.

(91) Moore, A. W., Jr.; Jacobson, S. C.; Ramsey, J. M. *Anal. Chem.* **1995,** *67*, 4184-9.

(92) Koch, M.; Schabmueller, C. G. J.; Evans, A. G. R.; Brunnschweiler, A. *Sens. Actuators* **1999,** *A74*, 207-210.

(93) Belgrader, P.; Okuzumi, M.; Pourahmadi, F.; Borkholder, D. A.; Northrup, M. A. *Biosens. Bioelectron.* **2000,** *14*, 849-852.

(94) Delamarche, E.; Bernard, A.; Schmid, H.; Bietsch, A.; Michel, B.; Biebuyck, H. *J. Am. Chem. Soc.* **1998,** *120*, 500-508.

(95) Delamarche, E.; Bernard, A.; Schmid, H.; Michael, B.; Biebuyck, H. *Science* **1997,** *276*, 779-781.

(96) Kane, R. S.; Takayama, S.; Ostuni, E.; Ingber, D. E.; Whitesides, G. M. *Biomaterials* **1999,** *20*, 2363-2376.

(97) Schena, M.; Heller, R. A.; Theriault, T. P.; Konrad, K.; Lachenmeier, E.; Davis, R. W. *Trends Biotechnol.* **1998,** *16*, 301-306.

(98) Thompson, M.; Michelle Furtado, L. *Analyst* **1999,** *124*, 1133-1136.

(99) Ravine, D. *J. Inherited Metab. Dis.* **1999,** *22*, 503-518.

(100) Colantuoni, C.; Purcell, A. E.; Bouton, C. M. L.; Pevsner, J. *J. Neurosci. Res.* **2000,** *59*, 1-10.

(101) Graves, D. J. *Trends Biotechnol.* **1999,** *17*, 127-134.

(102) Hicks, J. In *R&D*, 1999; Vol. 41, pp 28-29, 31-33.

(103) Hacia, J. G. *Nat. Genet.* **1999,** *21*, 42-47.

(104) Humphery-Smith, I.; Cordwell, S. J.; Blackstock, W. P. *Electrophoresis* **1997,** *18*, 1217-1242.

(105) McGall, G. H.; Barone, A. D.; Diggelmann, M.; Fodor, S. P. A.; Gentalen, E.; Ngo, N. *J. Am. Chem. Soc.* **5082,** *119*, 1997.

(106) Anderson, R. C.; McGall, G.; Lipshutz, R. J. *Top. Curr. Chem.* **1998,** *194*, 117.

(107) Lipshutz, R. J.; Fodor, S. P. A.; Gingeras, T. R.; Lockhart, D. J. *Nat. Genet.* **1999,** *21*, 20-24.

(108) Cheng, J.; Kricka, L. J.; Sheldon, E. L.; Wilding, P. *Top. Curr. Chem.* **1998,** *194*, 215-231.

(109) Gosling, J. P. *Clin. Chem.* **1990,** *36*, 1408.

(110) Christopoulos, T. K.; Diamandis, E. P. In *Immunoassay*; Diamandis, E. P., Christopoulos, T. K., Eds.; Academic Press: New York, 1996, pp 227.

(111) Vuori, J.; Rasi, S.; Takala, T.; Vaananen, K. *Clin. Chem.* **1991,** *37*, 2087.

(112) Xu, Y.-Y.; Pettersson, K.; Blomberg, K.; Hemmila, I.; Mikola, K.; Lovgren, T. *Clin. Chem.* **1992,** *38*, 2038.

(113) Varenne, A.; Vessieres, A.; Salmain, M.; Durand, S.; Brossier, P.; Jaouen, G. *Anal. Biochem.* **1996,** *242*, 172.

(114) Brown, C. R.; Higgins, K. W.; Frazer, K.; Schoelz, L. K.; Dyminski, J. W.; Marinkovich, V. A.; Miller, S. P.; Burd, J. F. *Clin. Chem.* **1985,** *31*, 1500.

(115) Fotiou, F. K. *Anal. Chem.* **1992,** *64*, 1698.

(116) Dou, X.; Takama, T.; Yamaguchi, Y.; Yamamoto, H.; Ozaki, Y. *Anal. Chem.* **1997,** *69*, 1492.

(117) Sijtsema, N. M.; Duindam, J. J.; Puppels, G. J.; Otto, C.; Greve, J. *Appl. Spectrosc.* **1996,** *50*, 545.

(118) Rohr, T. E.; Cotton, T.; Fan, N.; Tarcha, P. J. *Anal. Biochem.* **1989,** *182*, 388.

CHAPTER 1. ELECTROCHEMICALLY-ACTUATED MERCURY PUMP FOR FLUID FLOW AND DELIVERY

A manuscript in preparation for submission to *Analytical Chemistry*

Jing Ni,[1] Shelley J. Coldiron,[1] Chuan-Jian Zhong,[1,2] and Marc D. Porter[1,3]

Abstract

This paper describes the development of a prototype pumping system for the potential incorporation into miniaturized, fluid-based analytical instruments. The approach extends the well-established electrocapillarity phenomena at a mercury/electrolyte interface as the mechanism for pump actuation. That is, electrochemically-induced changes in surface tension of mercury result in the piston-like movement of a mercury column confined within a capillary. We present herein theoretical and experimental assessments of pump performance. The design and construction of the pump are detailed, and the potential attributes of this design, including the generated pumping pressure, flow rate, and power consumption are discussed. The possible miniaturization of the pump for use as a field-deployable, fluid-delivery device is briefly examined.

Introduction

The growing need for small-sized, field/site-deployable instrumentation to function as environmental monitors in both earth- and space-based applications has stimulated a great deal of interest in the design of miniaturized analytical instrumentation.[1, 2] Operationally, a

[1] Microanalytical Instrumentation Center, Ames Laboratory-USDOE, and Department of Chemistry, Iowa State University, Ames, IA 50011
[2] Current address: Department of Chemistry, State University of New York at Binghamton, Binghamton, NY 13902
[3] Corresponding author

reduction in size may also reduce the consumption of reagents, shorten analysis times, and enhance the capability to analyze small amounts of samples.[3] Indeed, efforts to reduce significantly the size of analytical systems that are the workhorses in the analytical laboratory, such as flow injection analyzers (FIA)[4] and capillary electrophoresis devices,[5, 6] gas[7] and liquid chromatographs (LC),[8, 9] and mass spectrometers,[10] have been ongoing since the 1980's. These developments, some of which were triggered by breakthroughs in micromachining and microfabrication capabilities,[11, 12] have led to far-reaching concepts such as the chemical analysis laboratory on a chip, electronic noses, and biochips.[13]

Of the many challenges in merging micromachining and chemical analysis technologies, the development of micropumps continues to be a key issue. Development issues include not only the construction and integration of micropumps, but also the formulization of descriptions for fluid flow (i.e., microfluidics[14]) within exceedingly small-sized (e.g., tens of microns) channels. Several types of micropumps and requisite microvalves have been devised and extensively tested along with various forms of micromixers and microdosers.[15-17] In many of the existing examples, micromachined silicon or polymer diaphragms have served as flexible physical elements that induce fluid flow via piezoelectric, pneumatic, or magnetic actuation. The limited lifetime of these diaphragms, however, remains somewhat problematic.

Recently, surface tension changes along a flow channel have been employed for fluid pumping, a concept known as Marangoni flow.[18, 19] In these approaches, a surface tension gradient was generated between two electrodes positioned on the walls of the flow channel, using electrochemical reactions of surfactants,[18] immiscible electrolyte solutions,[20] or polymer gels.[19] This paper describes a completely different approach for exploiting change in surface tension for the construction of a miniaturized pump. It is based on the

ability to induce changes in the surface tension of liquid metals, such as mercury.[21, 22] Compared to gravitational and frictional forces, the effects of surface tension in fluidic systems become increasingly significant upon miniaturization, and are generally dominant in the microgravity conditions encountered in outerspace. Our pumping principle relies on the electrochemically-induced changes in the surface charge, and hence, the surface tension, of mercury in contact with an electrolytic solution.

Descriptions of the change in surface tension of mercury as a function of applied potential and electrolyte composition (i.e., electrocapillary curves) have been a long standing research area in electroanalytical chemistry.[23] This type of plot for mercury electrodes often has a parabolic shape, where the surface tension maximum is defined as the potential of zero charge (pzc). Thus, the excess charge that accumulates at a mercury surface at applied potentials more positive or more negative than the pzc causes a decrease in surface tension, which in turn, results in a relaxation in the curvature of a mercury drop. This shape change is the basis of the mercury beating heart laboratory demonstration,[24] and has been used in optical and electrical switching applications.[25, 26] The electrocapillarity of mercury has also been harnessed as a mechanical actuation process, which was first theorized by Matsumoto et al. in a micropump format,[27] and recently used by Lee et al. to build a micromachined mercury motor.[28] We present herein the first demonstration of this phenomenon,[21, 22] which may have applicability in various microelectromechanical systems (e.g., chemical dispensers, reactors, and analyzers), to drive fluids continuously through a capillary. The potential application of this type of pump in miniaturized fluidic-based analytical instruments is briefly discussed.

Experimental

Chemicals. Mercury (ACS certified) was purchased from Fisher (Caution: hazardous vapor), and subsequently cleaned by three passes through freshly pierced filter paper (hole i.d. of ~0.5 mm). Platinum wires (0.2 mm diameter), used to make connect with the mercury pool or as a counter electrode, were obtained from Aldrich and used as received. Potassium chloride (ACS certified) was also acquired from Fisher.

Mercury pump construction. The proof-of-concept design of the mercury pump (not to scale) is shown in Figure 1. The pump is composed of two components: the main body and the insert. Figure 1A shows the two parts before assembly and Figure 1B provides two and three-dimensional illustrations of the pump after assembly. The single-piece insert, shown in the upper left, consists of a 2.5 cm x 2.5 cm x 0.5 cm top platform and a cylindrically shaped, open-bottomed capillary, which is defined as the inner capillary. The inner capillary is 1.2 cm long. A horizontal flow channel (0.8 mm i.d.) was drilled through the platform, and opened into the inner capillary of the pump. Four small vent holes (i.d. of 0.2 mm) were drilled through the insert for pressure equilibration with the outer reservoir during actuation.

The outer mercury reservoir, shown in the lower left, was formed by drilling a hole into a 2.5 cm x 2.5 cm x 2.0 cm Plexiglas block. The depth of this reservoir is 1.5 cm. A coiled platinum wire was introduced from the side of the pump body into the outer reservoir, and used as the counter electrode. Another platinum wire was inserted through the bottom of pump to make electrical contact with the mercury. The two wires are then connected to an external electrical source (i.e., a waveform generator or a potentiostat) to manipulate the voltage applied across the mercury/electrolyte interface. The inner and the outer radii of the inner capillary, and the radius of the outer reservoir were varied as part of our assessments of factors that affect pump performance.

In assembling the pump, 50 to 150 μL of freshly cleaned mercury were pipetted into the outer reservoir depending on the size of the pump. The insert and the main body were then assembled, as illustrated in Figure 1B. The assembled pump therefore consists of two concentrically aligned mercury columns, partially filling the inner capillary and the outer reservoir as a result of capillary action. An aqueous electrolytic solution (0.5 M KCl) was introduced into the outer reservoir through the vent holes, forming the outer mercury/electrolyte interface.

Relative height determinations. To determine precisely the relative height (*h*) of the internal and external mercury columns, the pump insert was modified by removing the flow channel section of the upper platform along the dashed line a-a' in Figure 1. The same electrolyte was added on top of the inner mercury column to prevent the evolution of hazardous mercury vapor. A Ag/AgCl (sat'd KCl) reference electrode was then inserted into the electrolyte solution in the outer reservoir, and a potentiostat (Bioanalytical Systems CV-27) was used to supply the voltage to the mercury column in a common three-electrode configuration. Note that both the counter and reference electrodes are located in the outer reservoir and that there is no electrical connection between the inner and outer pools of electrolyte; the voltage is therefore applied only across the interface formed between the electrolyte and outer mercury column.

Two additional platinum wires were mounted on separate micromanipulators (1 μm resolution), and connected to a multimeter (Wavetek 28XT) that was set in its audible continuity test mode. To determine *h*, one of the wires was carefully moved toward the top of the inner mercury column, and the other toward the top of the outer mercury through a vent hole. When both wires made contact with the mercury, the resulting electrical continuity triggered the audio signal from the multimeter. The difference in the readings from the two micromanipulators then represented the relative height, *h*. In all tests, *h* was

determined under two conditions: when the applied voltage was near the pzc of mercury (pzc for mercury in contact with 0.1 M KCl is -0.423 V vs. Ag/AgCl (sat'd KCl)[29]), and when the applied voltage was 1-2 volts negative of the pzc. The difference between the two values of h was defined as the change in relative height, Δh.

Flow rate measurements. In evaluations of flow rate viability, a set of ball-style check valves were attached to each end of the flow channel with heat-shrinkable tubing. These check valves, which were manufactured by Ace Glass Inc, used 2 mm diameter spheres made from silicon carbide. The inlet side of the pump was then immersed in a solution reservoir, while the check valve on the outlet side of the pump was connected to a glass (0.8 mm i.d.) capillary. The relative height of the solution inlet and outlet was adjusted in order to avoid gravity-induced fluid flow.

Before each measurement, the fluid conduit, which included the mercury pump, check valves, and the glass capillary, was primed by applying carefully a vacuum to the outlet of the flow channel with a syringe. Square voltage waveforms were applied to the outer mercury/electrolyte interface using a TENMA 72-3060 function generator, which induced the movement of the two mercury columns. Flow rates were determined by measuring the displacement of the fluid per unit time within the horizontal flow channel located at the outlet side of the pump. The volume flow rate (F) was calculated by multiplying the flow velocity with the cross section area of the flow channel. The volume per actuation cycle data (VPC) at low pumping frequencies ($\leq$1 Hz) were obtained by measuring directly the displacement length of the fluid during each cycle, while those at high frequencies were back calculated from the volume flow rates. All experiments were performed at room temperature.

Power consumption determinations. To determine the power consumption of the mercury pumps, a voltage step was applied across the mercury/electrolyte interface

potentiostatically. Pumps, similar to those used in relative height determinations, were used in this set of experiments. The change in the double layer charging current was immediately recorded upon application of the voltage step. Theoretically, the power consumption for the pump can be determined via the applied voltage, actuation frequency, and integrated charge passed during an actuation cycle. However, only the maximum power consumption, which was estimated from the product of the change in the applied voltage and the maximum charging current, will be reported in order to obtain a general perspective on the instantaneous power consumption of the pump.

Results and Discussion

Theoretical assessment. Earlier theoretical models of the pressures generated by changes in the surface tension of mercury were used in a preliminary assessment of concept feasibility.[27, 30] These models consider the situation where an open capillary is inserted into a large mercury pool, which is subsequently filled with mercury by capillary action. In this situation, the mercury confined within the capillary exhibits capillary depression. The fundamental relationships that correlate changes in surface tension ($\Delta\gamma$), changes in relative height of mercury column (Δh), and changes in pressure across the mercury/electrolyte interface (ΔP) are given by the formulations of Young and Laplace in equations 1 and 2.[30]

$$\Delta h = 2\frac{\Delta\gamma}{R\rho g}\cos\theta \qquad (1)$$

$$\Delta P = \rho g \Delta h \qquad (2)$$

where R is the inner radius of the capillary, ρ is the density of mercury, g is the gravitational acceleration, and θ is the contact angle at the mercury-capillary wall interface. These

equations describe the equilibrium relationship between interfacial and gravitational forces within the capillary.

If the surface tension change-induced pressure change can be utilized to drive liquid flow, the predicted ΔP can then be used to determine the flow rate (F) based on equation 3. This equation relates F and ΔP in terms of the radius of the flow channel (r), the viscosity of the pumped fluid (η_m), and the length of the flow channel (L).[31]

$$F = \frac{\pi r^4}{8\eta_m}\frac{\Delta P}{L} \qquad (3)$$

Collectively, these equations show that the fluid flow rate can be manipulated by controlling the change in the surface tension of mercury. That is, the greater $\Delta\gamma$, the larger Δh and ΔP, and the higher the value of F. Moreover, equation 2 points to an important attribute of miniaturization - by reducing the radius R of the capillary, a higher ΔP can be achieved for the same $\Delta\gamma$.

Flow rates were calculated based on these equations for conditions typically employed in miniaturized FIA and LC applications. With FIA, flow channels usually have a r of ~250 μm and F of a few hundreds of μL/min.[32] In miniaturized open tubular LC systems, however, the flow channels are much smaller (r of 5 to 10 μm) as are the flow rates (F of a few nL/min.[2, 3]). Table 1 summarizes the theoretical Δh, ΔP, and F results that were calculated with channel dimensions mimicking those in FIA or LC applications. In these calculations, we assumed a θ of 0°, a L of 10 cm, a η_m of 1 x 10^{-3} N-s-m^{-2} (i.e., the viscosity of water), and set r equal to R. The calculation also used a $\Delta\gamma$ value of 100 dynes/cm, a change easily accessible when mercury is in contact with aqueous electrolytes (e.g., 0.1 M KCl).[29]

The results in Table 1 demonstrate that the pump can theoretically function in both types of analytical formats. For example, with both r and R equal to 250 μm, a $\Delta\gamma$ of 100 dynes/cm results in a ΔP of 0.12 psi, and F as high as 736 μL/min. In contrast, setting r and R equal to 5 μm results in a ΔP of 5.80 psi, and F of near 6 nL/min. These results, which demonstrate the intricate interplay between R, ΔP, and F, support the possible applicability of our pump concept in both miniaturized FIA and LC.

Experimental performance evaluations. Building on the results of the feasibility assessments, the pump shown in Figure 1 was constructed and tested. This design confines the outer mercury pool within a reservoir, whose radius is slightly larger than the external radius of the inner capillary. Under open circuit conditions, the relative height between the inner and outer mercury columns reflects the balance of forces from gravity and surface tension. By controlling the radius of each capillary, the inner mercury column can be forced to rise to a height greater than that of the outer mercury column. The actuation of the pump relies on how the surface tension of the outer mercury column is altered through changes in the voltage applied across the outer mercury/electrolyte interface. This change in surface tension causes both mercury columns to reposition until a new balance between gravity and surface tension is established, with the height change of the inner mercury column exploited to displace the fluid within the flow channel. The following examines how the displacement of the inner mercury column as a function of the applied voltage can be harnessed to pump fluids. The power consumption of the pump is then estimated, and a brief discussion of the possible use of this pump in a microfluidics system is presented.

(i) *ΔP and Δh.* The first set of experiments examined the influence of applied voltage on ΔP and Δh. As mentioned in the Experimental section, the voltage is applied only across

the outer mercury/electrolyte interface, indicating that only the outer mercury surface tension is affected by a change in the applied voltage (ΔE). This change in surface tension ($\Delta\gamma$) leads to a pressure change in the outer reservoir, which causes the two mercury columns to move until a new pressure balance is established by the change in relative height (Δh) of the inner and outer mercury columns. Therefore, Δh is a reflection of the electrochemically-induced ΔP, and it is a consequence of the displacements of both the inner (Δh_{in}) and the outer (Δh_{out}) mercury columns.

The actuation process of the mercury pump is demonstrated by the two photographs in Figure 2. These photographs were taken when applying either –1.8 V (Figure 2A) or -0.4 V (Figure 2B) to the mercury pool with respect to a Ag/AgCl (sat'd KCl) reference electrode; 0.5 M KCl was used as the supporting electrolyte. Considering the pzc for mercury is around -0.4 V vs. Ag/AgCl (sat'd KCl),[29] Figure 2A therefore, shows the relative height between the inner and outer mercury columns at an applied voltage that is ~1.4 V negative of the pzc. Figure 2B, on the other hand, represents the relative heights at an applied voltage that is close to the pzc. Based on the electrocapillary curve for mercury in 0.1 M NaCl,[33] this difference in applied voltage induces a $\Delta\gamma$ of ~200 dynes/cm, which, as shown in Figure 2, results in a Δh of ~2.6 mm. This height change corresponds to an elevation of the inner mercury column (Δh_{in}) by nearly 1.5 mm, and to a lowering of the outer mercury column (Δh_{out}) by ~1.1 mm. Hence, it is Δh_{in} that causes the piston-like displacement of the liquid in contact with the inner mercury column, and forms the basis of our pumping mechanism.

The general shape of an electrocapillary curve, when combined with the predictions of equation 1, suggests that Δh can be manipulated by controlling ΔE. Our tests have shown that changing the negative limit of the applied voltage to –1.0 V, instead of the –1.8

V used for the experiment in Figure 2A, reduces Δh to ~1.1 mm. However, the maximum Δh that can be obtained is limited by the most negative voltage that can be applied across the mercury/electrolyte interface before hydrogen evolution, which occurs near –2.0 V vs. Ag/AgCl (sat'd KCl) according to a voltammetric current-potential curve. We also found, as expected, that the identity and concentration of the supporting electrolyte influenced the displacement of the two columns, but that the displacements were not significantly different when using simple electrolytes (e.g., sodium vs. potassium, chlorides vs. nitrates), over concentration ranges between 0.1 M and 1 M. Therefore, 0.5 KCl was used as the supporting electrolyte for the remainder of these experiments for comparison purposes.

Besides electrochemically controlling $\Delta\gamma$, equations 1 and 2 suggest that the radius of the capillaries (R) should also affect Δh and therefore ΔP. To assess this effect, pumps were constructed having different values of R. The experimental Δh of each pump was then determined from the relative height data at -0.4 and -1.8 V vs. Ag/AgCl (sat'd KCl).

To calculate theoretical values for Δh, equation 1 serves as a starting point to derive the correlation between Δh and the size of the two confined mercury columns in our concentrically-aligned geometry. Recognizing that the voltage is applied to the outer mercury/electrolyte interface, only the surface tension of the outer mercury column changes when the applied voltage is altered. Equation 4, which reflects a balance of the effect of gravity at the inner mercury column with the surface tension-induced change in pressures at the two contact surfaces of the outer mercury column, can therefore be written:

$$\Delta h = \frac{2\Delta\gamma\cos\theta}{\rho g}\left(\frac{1}{R_1 - R_2}\right) \qquad (4)$$

where R_1 is the radius of the outer reservoir, and R_2 is the external radius of the inner capillary.

As mentioned earlier, Δh is an important parameter that relates to the pressure that can be generated by the pump. The displacement of the inner mercury column (Δh_{in}), is another important characteristic of the pump, and defines the displacement that can be utilized to induce fluid flow. The relationship between Δh_{in}, Δh, and the dimensions of the pump is presented in Equation 5:

$$\Delta h_{in} = \frac{R_1^2 - R_2^2}{R_1^2 - R_2^2 + R_3^2} \Delta h \qquad (5)$$

where R_3 is the internal radius of the inner capillary. The development of Equations 4 and 5 are detailed in the Appendix.

Four different-sized pumps were constructed; their sizes and performance figures of merit are given in Table 2. First, the theoretical and experimental results for Δh were compared. The experimental Δh data were then used to determine ΔP *and* Δh_{in} based on Equations 2 and 5. The calculations used a $\Delta\gamma$ of 200 dynes/cm, which is representative for the voltage biases used in these experiments, and a θ of 135°, which was measured from the photographs in Figure 2.

In general, the experimental results are in very good agreement with the theoretical expectations. For example, Δh increased with the decrease of R_1-R_2, as expected according to Equation 4. We attribute the small quantitative differences between experimental and theoretical results to several factors, including the approximate values of the contact angle and the surface tension used in the calculation, the disregard of the curvature of the mercury meniscus in the height measurement, and small misalignments of the inner capillary when placed in the outer reservoir.

Most importantly, Table 2 shows that two key aspects of pump performance, ΔP and Δh_{in}, are also affected by the physical size of the two containment columns, reflecting the

contribution of capillarity. That is, both ΔP and Δh_{in} increased with a decrease in R_1-R_2, suggesting an improved pump performance with the reduction of the separation distance between the capillaries. These results point to an important benefit of miniaturization - a decrease in size potentially enhances the ability of the pump to move fluids in microchannels.

(ii) *F.* Flow rate (F) is another important delimiter in defining pump performance. This set of experiments was aimed at delineating the flow rates accessible with our mercury-based pumps. Figure 3 conceptualizes the piston-like actuation process for inducing fluid flow. That is, at applied voltages removed from the pzc, which is termed the fill mode, the inner mercury column is distended and the inner capillary fills with the pumped fluid. The pump mode, in contrast, results when the inner mercury column extends in response to an applied voltage closer to the pzc, driving fluid out of the inner capillary. Thus, the application of a waveform that oscillates between the two extremes in applied voltage induces a piston-like reciprocation of the inner mercury column. This reciprocation can then be used for fluid delivery after incorporating check valves to realize one-directional flow.

In the flow rate characterization, square waveforms were applied across the outer mercury/electrolyte interface in a two-electrode configuration, i.e., the mercury electrode and the platinum coil electrode inserted in the electrolyte contacting the outer mercury column. Thus, a change in the magnitude and/or frequency of the applied voltage causes a difference in the magnitude of mercury displacement, and therefore a difference in F. Figure 4 shows the dependence of flow rate on the difference in the two limits in the applied waveform for pump #2. The amplitude of the waveform, E_+ - E_- or ΔE, was changed by resetting the negative limit (E_-) of the 1-Hz waveform after each measurement, while maintaining the same positive limit (E_+ = -1.0 V). These voltages were chosen so E_+ was

close to the pzc, while E_- moved increasingly negative of the pzc. Note that, here the values of E_+ and E_- are usually shift by ~1 V negatively when compared with the values referenced against Ag/AgCl, sat'd KCl.

As evident in Figure 4, applying a square waveform with lower negative limits results in a higher F. For instance, when E_- is -3.0 V (i.e., ΔE = +2 V), F is about three times larger than that observed when E_- is -2.0 V (i.e., ΔE = +1 V). Usually, the observed flow rate varies by 15% between replicated measurements using the same experimental setup. We note that a E_- lower than –3.5 V results in strong hydrogen evolution, which degrades the reliability of flow characterizations.

Flow rate can also be manipulated by changing the frequency of the voltage waveform. A set of these results obtained from pump #2 is shown in Figure 5 with the flow characteristics presented as both the volume per actuation cycle (VPC) and the volume flow rate (F). In these measurements, a square waveform with E_+ at -1.0 V and E_- at -3.0 V was used to induce mercury actuation. These voltage differences correspond approximately to 0.0 V and -1.8 V vs. Ag/AgCl (sat'd KCl), respectively. The results are plotted as a function of the frequency of the waveform. As evident, F initially increases as the frequency of the waveform increases, reaches a maximum (~175 μL/min) at about 1 Hz, and then decreases to nearly 10% of its maximum value at 20 Hz. There is no measurable flow above 20 Hz. The value of VPC, on the other hand, exhibits a maximum (~12 μL) at lower frequencies, starts to decrease above 0.1 Hz, and is immeasurable above 10 Hz.

We attribute the decay of VPC and the fall off of F at higher frequencies to the time constant of the pump. When modeling the mercury pump as a simple RC circuit, a nonlinear-least-square fit of the VPC dependence yields a overall time constant of ~2 s. Two factors, the electrochemical time constant of the pump (i.e., the combined effect of electrolyte resistance and interfacial capacitance) and the inertial time constants of the

mercury column and the check valves, were considered as the main contributors to the overall time constant. A voltage step experiment showed that the electrochemical time constant of a mercury electrode of similar size was less than 0.2 s, leaving the inertial drag of mercury column and/or check valves as the most likely contributors to the above observations. Since the overall weight as well as the density of mercury (ρ = 13.6 g/cm^3) are much higher than those of the check valves (ρ = 2.7 g/cm^3), we believe the decrease in performance at higher frequencies arises mainly from the inertia in inducing physical movement of mercury. In support of this conclusion, plots of *F* and VPC vs. the frequency of the voltage waveform for experiments using pump #4, which has smaller-sized mercury columns, have a maximum for *F* at 5 Hz, an increase in the actuation frequency yielding detectable fluid flow up to 50 Hz, and a reduction in the overall time constant to 0.4 s. Since this experiment used the same set of check valves, these findings demonstrate that the inertial drag of mercury is a key factor in controlling the time response of the mercury columns upon electrical stimulation. Importantly, a reduction in size may again improve the pump performance.

(iii) Power consumption. An experiment was also performed to develop a perspective on the power consumption of the pump. The initial peak current density after stepping the applied voltage from –0.4 V to -1.8 V vs. Ag/AgCl (sat'd KCl) was almost 5 mA/cm^2. Therefore, the highest current flow for pumps in described Table 2 was a few milliamperes, a level that reflects the current required to charge the electrical double layer formed by the contact between the mercury meniscus and the supporting electrolyte as the applied potential is changed. This current level, coupled with the magnitude of the change in applied voltage (2 V), translates to a peak power consumption of a few milliwatts. These levels of voltage and power are in contrast to electrostatic pump actuation, which consumes little power but typically requires high voltage,[5] and to electromagnetic[7] or thermal

actuation,[34] which use low voltage but operate at high power. Intriguingly, the low voltage and power consumption of our pump suggest that the small-sized power cells used in devices like wrist watches and cameras can be adopted to operate this type of pumps. The existence of a readily-available, small-sized power supplies will clearly facilitate the ongoing efforts to reduce the size of the pump to a chip-scale format.

Conclusions

In this report, we have described the capabilities of an electrochemically-driven mercury pump for fluid flow and delivery. Changes in relative mercury height for pumps having several different design parameters were studied, and the experimental results showed good agreement with theoretical predictions. Flow rates up to a few hundred microliters/min and fluid dispensing volumes as high as several tens of microliters per actuation cycle were achieved in a capillary column using mercury pumps assisted by ball-style check valves for controlling the fluid flow direction. Both the change in relative mercury height and flow rate increased proportionally to the amplitude of the voltage waveform. The low voltage requirement and power consumption of this pump may also facilitate the eventual miniaturization of the fluidic system.

Encouraged by these preliminary results, experiments to enhance performance through further optimization of the different functional elements of the pump and flow system to meet the needs of chemical analysis systems are underway. Furthermore, we believe that the potential environmental hazard of mercury can be minimized by the further reduction of the pump size and therefore the amount of mercury required for effective actuation.

Acknowledgments

J. N. gratefully acknowledges the support of the ACS Analytical Division Fellowship that is sponsored by the Eastman Chemical Company. We express our appreciation to Mike Granger, Jeremy Kenseth, and Robert Lipert, for their assistance in manuscript preparation. This work was supported by NASA (Grant #NAGW4951) and the Microanalytical Instrumentation Center of Iowa State University.

Appendix

This section presents the mathematical derivation for the dependence of the change in relative height, Δh (i.e., Equation 4), and the inner mercury column displacement, Δh_{in} (i.e., Equation 5) on the radii of the concentrically-aligned inner capillary and outer reservoir. The fundamental principle underlying the Young and Laplace equations serve as the starting point of the derivation, which is based on the pressure balance inside the two mercury columns as affected by surface tension and gravity. Specifically, the relative height of the two mercury columns at equilibrium reflects the balance of the pressure at the inner capillary (P_{in}) and the outer reservoir (P_{out}):

$$P_{out} = P_{in} \qquad \text{(A)}$$

Both pressures can be calculated using the forces that act on the mercury columns divided by their meniscus areas (A). The force at the outside column (f_{out}) can be written as the sum of the surface tensions (γ_{out}) at the inner wall of the outer reservoir and the outer wall of the inner capillary:

$$f_{out} = 2\pi(R_1 + R_2)\gamma_{out}\cos\theta \qquad \text{(B)}$$

This force acts on the meniscus of the outer mercury column, the area of which can be approximated as:

$$A_{out} = \pi(R_1^2 - R_2^2) \quad \text{(C)}$$

The expression for P_{out} is then:

$$P_{out} = \frac{2\gamma_{out}\cos\theta}{R_1 - R_2} \quad \text{(D)}$$

The total force acting within the inner column (f_{in}) at the outer meniscus height can be given as:

$$f_{in} = 2\pi R_3\gamma_{in}\cos\theta + \pi R_3^2 h\rho g \quad \text{(E)}$$

where the first term in the equation defines the force related to the surface tension of the inner mercury column (γ_{in}), and the second term in the equation reflects the force due to the relative height (h) of the two columns. This force is applied across the surface area of the inner column (A_{in}):

$$A_{in} = \pi R_3^2 \quad \text{(F)}$$

The expression of P_{in} is then written as:

$$P_{in} = \frac{2\gamma_{in}\cos\theta}{R_3} + \rho g h \quad \text{(G)}$$

Collectively, the value of h can then be developed by equating Equations D and G and rearranging to yield:

$$h = \frac{2\cos\theta}{\rho g}\left(\frac{\gamma_{out}}{R_1 - R_2} - \frac{\gamma_{in}}{R_3}\right) \quad \text{(H)}$$

Since the voltage is applied only across the outer mercury/electrolyte interface, the γ_{out} changes by a value of $\Delta\gamma$. This change results in a new height difference ($h+\Delta h$) between the inner and outer mercury columns, with Δh defined as the change in relative height.

A similar set of equations (I-L) can also be written based on the pressure balance under the new equilibrium established by $\Delta\gamma$, with parameters of importance given as "primed" terms.

$$P'_{out} = P'_{in} \tag{I}$$

$$P'_{out} = \frac{2(\gamma_{out} + \Delta\gamma)\cos\theta}{R_1 - R_2} \tag{J}$$

$$P'_{in} = \frac{2\gamma_{in}\cos\theta}{R_3} + \rho g(h + \Delta h) \tag{K}$$

$$h + \Delta h = \frac{2\cos\theta}{\rho g}\left(\frac{\gamma_{out} + \Delta\gamma}{R_1 - R_2} - \frac{\gamma_{in}}{R_3}\right) \tag{L}$$

Combining Equations H and L, and solving for Δh, gives Equation 4.

The volume of fluid displaced by the pump in a single actuation step is directly related to the displacement of the inner mercury column, Δh_{in}, which can be derived from Δh through the physical dimensions of the pump. Since the total volume of the mercury inside of the pump is fixed, an increase in the volume of mercury in the inner capillary (ΔV_{in}) must equal the decrease in the volume of mercury in the outer reservoir (ΔV_{out}).

$$\Delta V_{out} = \Delta V_{in} \tag{M}$$

Each of these volume changes can be expressed as the product of the height displacement of the mercury column, and the surface area of the corresponding meniscus:

$$\Delta V_{out} = \pi(R_1^2 - R_2^2)\Delta h_{out} \tag{N}$$

$$\Delta V_{in} = \pi R_3^2 \Delta h_{in} \tag{O}$$

The above two equations can then be combined through Equation M and rearranged to show the relationship between Δh_{in} and Δh_{out}:

$$\Delta h_{in} = \frac{R_1^2 - R_2^2}{R_3^2} \Delta h_{out} \qquad \text{(P)}$$

Recognizing next that Δh is the direct result of Δh_{in} and Δh_{out}, we can write:

$$\Delta h = \Delta h_{in} + \Delta h_{out} \qquad \text{(Q)}$$

Finally, combining Equations P and Q, and solving for Δh_{in} in terms of Δh gives Equation 5.

References

(1) Shoji, S.; Esashi, M.; Schoot, B. H. v. d.; Rooij, N. d. *Sensors and Actuators A* **1992,** *32*, 335.

(2) Manz, A.; Graber, N.; Widmer, H. M. *Sensors and Actuators B* **1990,** *1990*, 244.

(3) Manz, A.; Harrison, D. J.; Verpoorte, E.; Widmer, H. M. *Adv. Chrom.* **1993,** *33*, 1.

(4) Schoot, B. H. v. d.; Jeanneret, S.; Berg, A. v. d.; Rooij, N. F. d. *Sensors and Actuators B* **1993,** *13*, 333.

(5) Jacobson, S. C.; Hergenroder, R.; Koutny, L. B.; Ramsey, J. M. *Anal. Chem.* **1994,** *66*, 1114.

(6) Woolley, A. T.; Sensabaugh, G. F.; Mathies, R. A. *Anal. Chem.* **1997,** *69*, 2181.

(7) Terry, S. C.; Jerman, J. H.; Angell, J. B. *IEEE Transactions on Electron Devices* **1979,** *26*, 1880.

(8) Manz, A.; Miyahara, Y.; Miura, J.; Watanabe, Y.; Miyagi, H.; Sato, K. *Sensors and Actuators B* **1990,** *1*, 249.

(9) He, B.; Tait, N.; Regnier, F. *Anal. Chem.* **1998,** *70*, 3790.

(10) Barber, S. J.; Morse, A. D.; Wright, I. P.; Kent, B. J.; Waltham, N. R.; Todd, J. F. J.; Pillinger, C. T. *Adv. Mass Spectrom.* **1998,** *14*.

(11) Mastrangelo, C. H.; Tang, W. C. In *Semiconductor Sensors*; Sze, S. M., Ed.; John Wiley and Sons: New York, 1994, pp 17.

(12) Kovacs, G. T. A.; Petersen, K.; Albin, M. *Anal. Chem.* **1996,** *38*, 407A.

(13) Harrison, D. J.; Berg, A. v. d. , Banff, Canada 1998; Kluwer Academic.

(14) Gravesen, P.; Branebjerg, J.; Jensen, O. s. *J. Micromech. Microeng.* **1993,** *3*, 168.

(15) Shoji, S.; Nakagawa, S.; Esashi, M. *Sensors and Actuators A* **1990,** *21*, 189.

(16) Lintel, H. T. G. v.; Pol, F. C. M. v. d.; Bouwstra, S. *Sens. Actuators* **1988,** *15*, 153.

(17) Olsson, A.; Enoksson, P.; Stemme, G.; Stemme, E. *Journal of Microelectromechanical Systems* **1997,** *6*, 161.

(18) Gallardo, B. S.; Gupta, V. K.; Eagerton, F. D.; Jong, L. I.; Craig, V. S.; Shah, R. R.; Abbott, N. L. *Science* **1999,** *283*, 57.

(19) Lee, H. J.; Fermin, D. J.; Corn, R. M.; Girault, H. H. *Electrochem. Comm.* **1999,** *1*, 190.

(20) Girault, H. H. J.; Schiffrin, D. J. *J. Electroanal. Chem.* **1984,** *179*, 277.

(21) Porter, M. D.; Hoffman, D. K.; Zhong, C. J. ; Iowa State University Research Fundation, Ames, Iowa: US, 1995.

(22) Porter, M. D.; Zhong, C.-J.; Ni, J.; Coldiron, S. J.; Tang, W. C. *SAE Technical Paper Series*, Lake Tahoe, Nevada, July 14-17, 1997 1997; 972420.

(23) Bard, A. J.; Faulkner, L. R. *Electrochemical Methods: Fundamentals and Applications*; John Wiley and Sons: New York, 1980.

(24) Lin, S.-W.; keizer, J.; Rock, P. A.; Stenschke, H. *Proc. Nat. Acad. Sci USA* **1974,** *71*, 4477.

(25) Jackel, J. L.; Hackwood, S.; Beni, G. *Appl. Phys. Lett.* **1982,** *40*, 4.

(26) Beni, G.; Tenan, M. A. *J. Appl. Phys.* **1981,** *52*, 6011.

(27) Matsumoto, H.; Colgate, J. E. *IEEE Micro Electro Mechan. Sys.* **1990**, 105.

(28) Lee, J.; Kim, C.-J. *IEEE Micro Electro Mechanical Systems Workshop* **1998**, 538.

(29) Wrona, P. K.; Galus, Z. In *Encyclopedia of Electrochemistry of the Elements*; Bard, A. J., Ed.; Marcel Dekker: New York, 1982; Vol. 9.

(30) Adamson, A. W. *Physical Chemistry of Surfaces*; John Wiley and Sons: New York, 1990.

(31) Giancoli, D. C. In *Physics: Principles with Applications*; Prentice-Hall, Inc: Englewood Cliffs, NY, 1980, pp 147.

(32) Ruzicka, J. *Flow Injection Analysis*; John Wiley and Sons: New York, 1988.

(33) Grahame, D. C. *Chem. Rev.* **1947**, *41*, 441.

(34) Zdeblick, M. J.; Anderson, R.; Jankowski, J.; Kline-Schoder, B.; Christel, L.; Miles, R.; Weber, W. *Solid-State Sensor and Actuator Workshop* **1994**, 251.

Table 1. Theoretical assessment for performance figures of merit using a mercury pump based on electrochemically-induced changes in surface tension.[a]

R, r (μm)	*Δh* (cm)	*ΔP* (psi)	*F* (μL/min)
500	0.3	0.06	5890
250	0.6	0.12	736
50	3	0.58	5.89
25	6	1.16	0.736
5	30	5.80	5.89×10^{-3}

[a] Values of Δh, ΔP, and F are based on a $\Delta\gamma$ of 100 dynes/cm, θ of 0°, η_m of 1×10^{-3} N-s-m^{-2}, ρ of 13.6×10^3 kg/m^3, g of 9.8 N/kg, and L of 10 cm.

Table 2. The theoretical (theo.) and experimental (exp.) assessment of the pump performance as a result of variation of inner capillary and outer reservoir dimensions, in terms of Δh, ΔP, and Δh_{in}.

Pump #	R_1 (mm)	R_2 (mm)	R_3 (mm)	R_1-R_2 (mm)	Δh (mm) theo.[a]	exp.[b]	Δh_{in} (mm) exp.	ΔP (psi) exp.
1	4.00	2.48	2.02	**1.52**	1.39	1.05	**0.74**	**0.02**
2	4.00	3.23	1.98	**0.77**	2.76	2.56	**1.47**	**0.05**
3	4.00	3.50	2.02	**0.50**	4.24	4.18	**2.00**	**0.08**
4	1.64	1.49	0.51	**0.25**	8.49	8.87	**5.71**	**0.17**

[a] Values of the theoretical Δh are based on a $\Delta\gamma$ of 200 dyne/cm, θ of 135°, ρ of 13.6×10^3 kg/m^3, and g of 9.8 N/kg.

[b] The Δh data obtained from repetitive measurements usually fell within ±0.1 mm of the presented values.

Figure Captions

Figure 1. Proof-of-concept design for the mercury pump (not to scale). (A) Before assembly. top: 2-D representation of the pump insert; bottom: 2-D representation of the pump body. (B) After assembly. top: 3-D representation of the assembled pump; bottom: 2-D representation of the assembled pump. See Experimental section for details.

Figure 2. Photographs of the electrochemically-induced actuation of the two mercury columns in pump #2. Captured at two different applied potentials: (A) –1.4 V negative of the pzc, (B) near the pzc. The supporting electrolyte was 0.5 M KCl.

Figure 3. A schematic representation of the fill and pump modes of the mercury-based pump as a result of application of a voltage step across the mercury/electrolyte interface. The arrows below the pump conceptualize the relative displacement of the mercury in the inner and outer capillaries. By applying a voltage waveform, the movement of the mercury column within the inner capillary mimics the actuation process of a piston pump. Two check valves are incorporated in the representation to realize uni-directional fluid flow.

Figure 4. The dependence of flow rate on the amplitude of the applied voltage waveform for pump #2. The positive limit (E_+) of the waveform was maintained at -1.0 V, while the negative limit (E_-) was changed in each measurement. The amplitude of the square waveform (ΔE) is defined by the difference between the two voltage limits (i.e., $\Delta E = E_+ - E_-$). The frequency of the square waveform was 1 Hz, and the supporting electrolyte was 0.5 M KCl.

Figure 5. The dependence of volume flow rate (F, •) and volume per actuation cycle (VPC, o) on the frequency of the applied voltage waveform measured using pump #2. The

positive and negative limits of the waveform were held at −1.0 and −3.0 V, respectively. The supporting electrolyte was 0.5 M KCl.

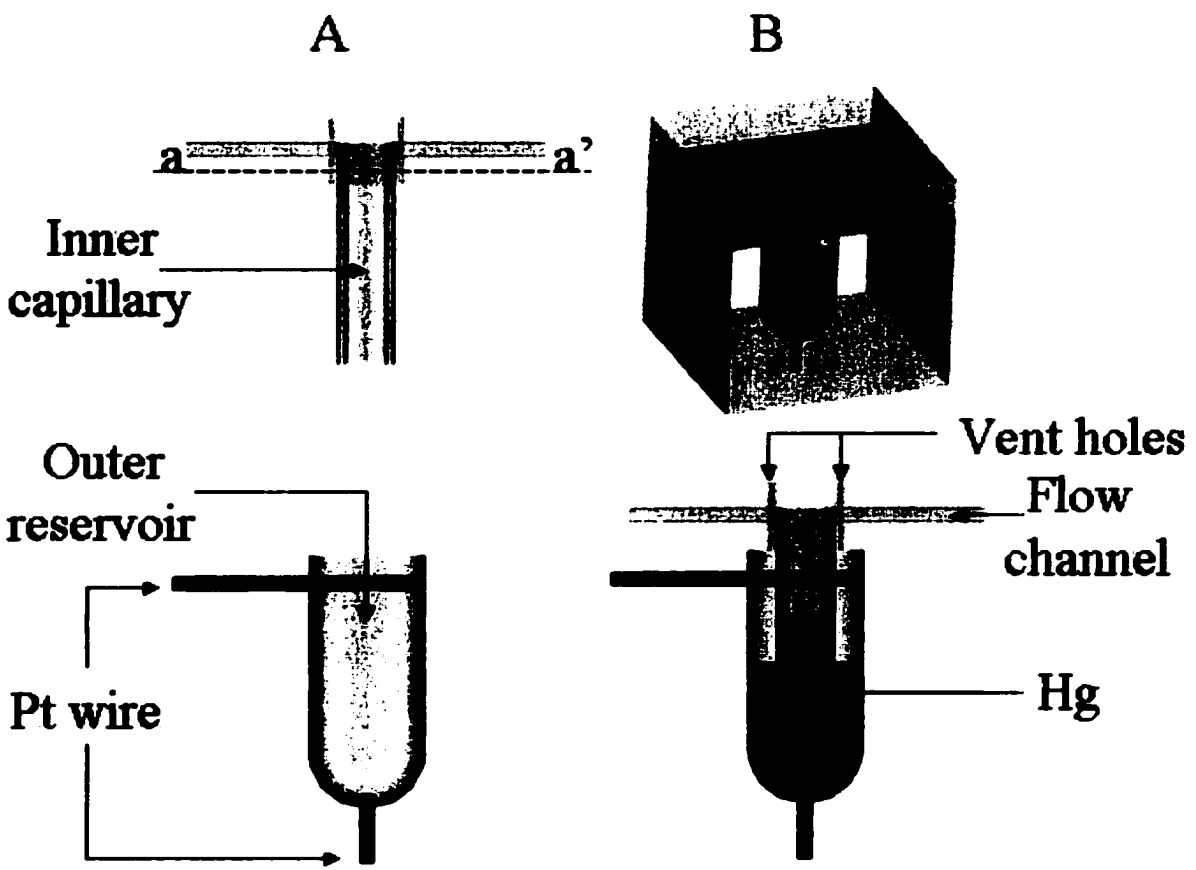
A
B
a
a'
Inner
capillary
Outer
reservoir
Pt wire
Vent holes
Flow
channel
Hg

Figure 1.

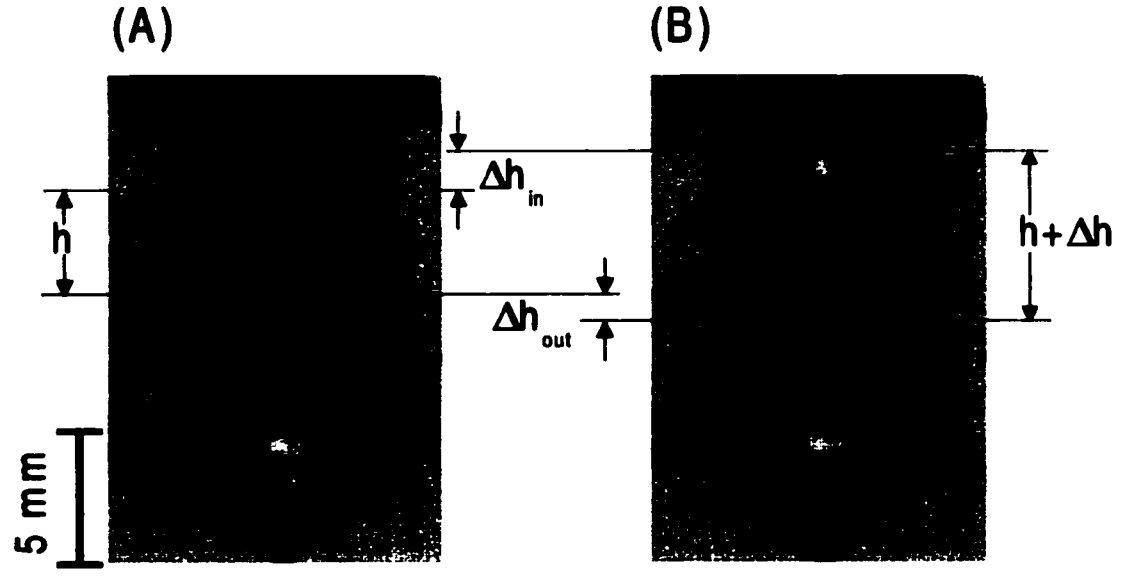
(A)
(B)
Δh in
h
Δh out
h+Δh
5 mm
E = -1.8 V vs. Ag/AgCl,sat'd KCl
~1.4V negative of pzc
E = -0.4 V vs. Ag/AgCl,sat'd KCl
near pzc

Figure 2.

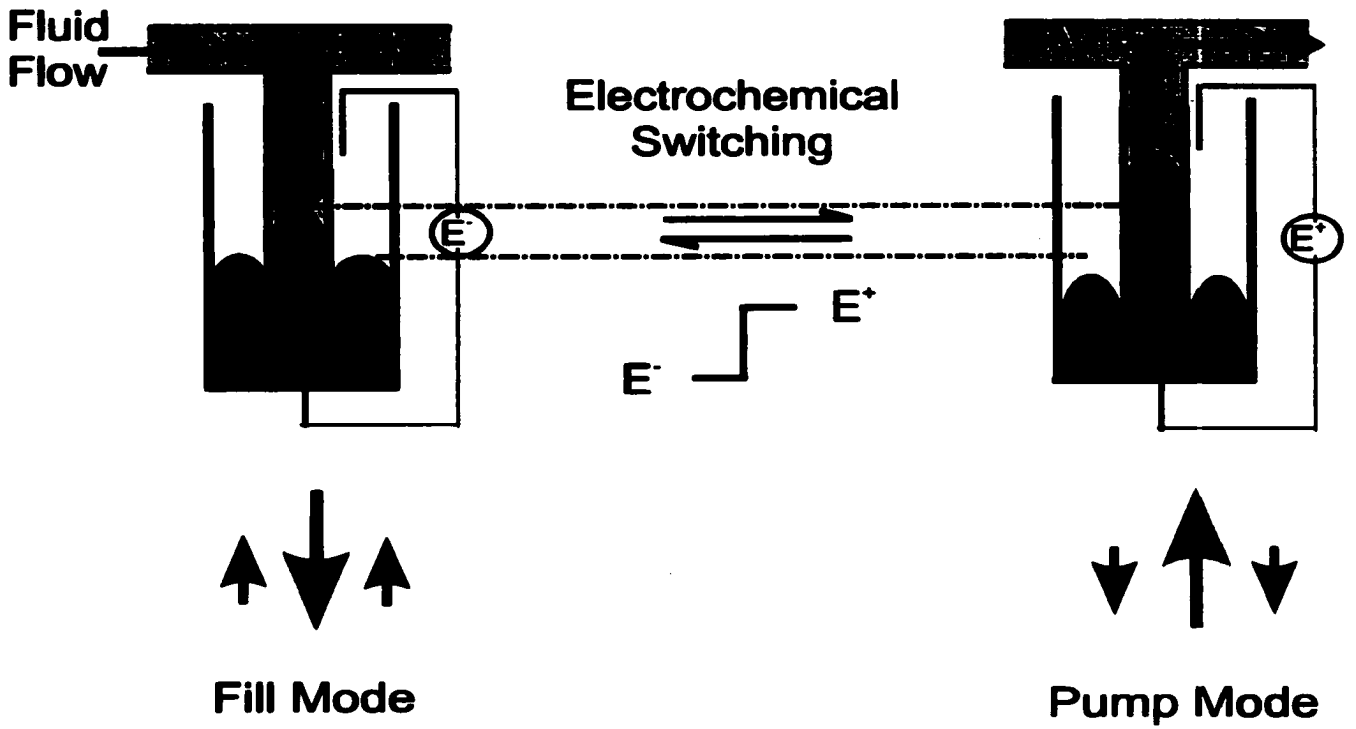
Fluid
Flow
Electrochemical
Switching
E-
E+
E+
E-
Fill Mode
Pump Mode

Figure 3.

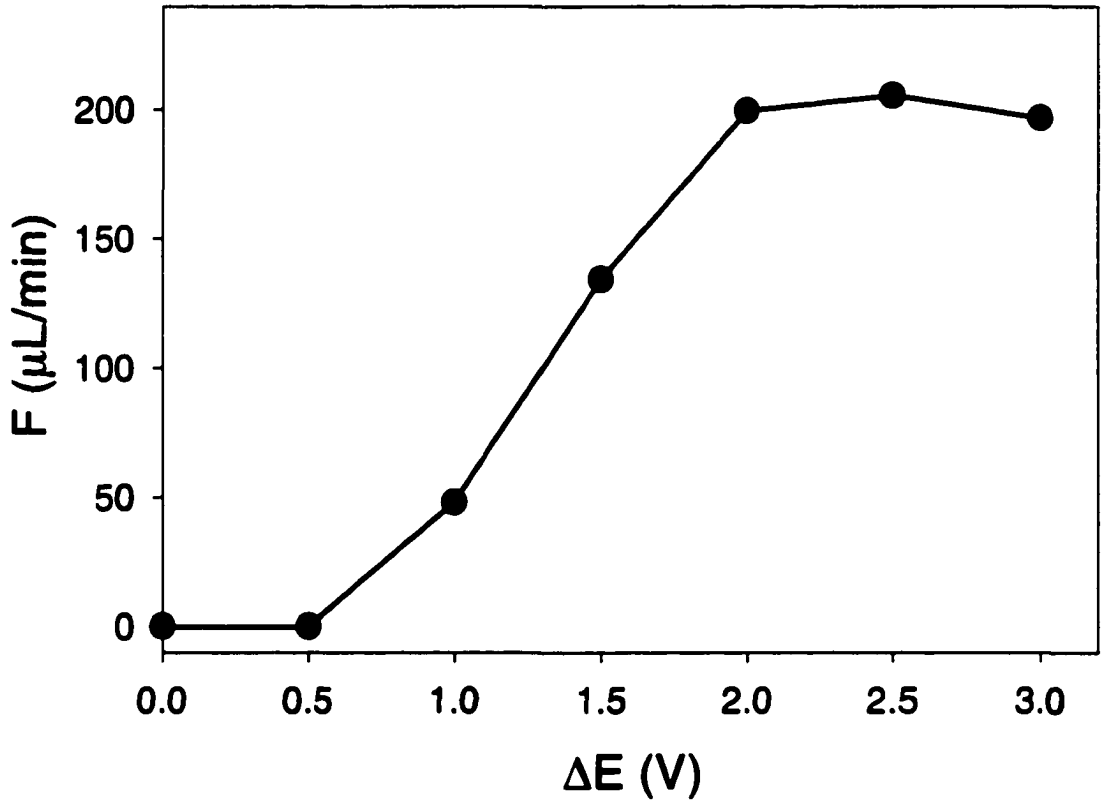

Figure 4.

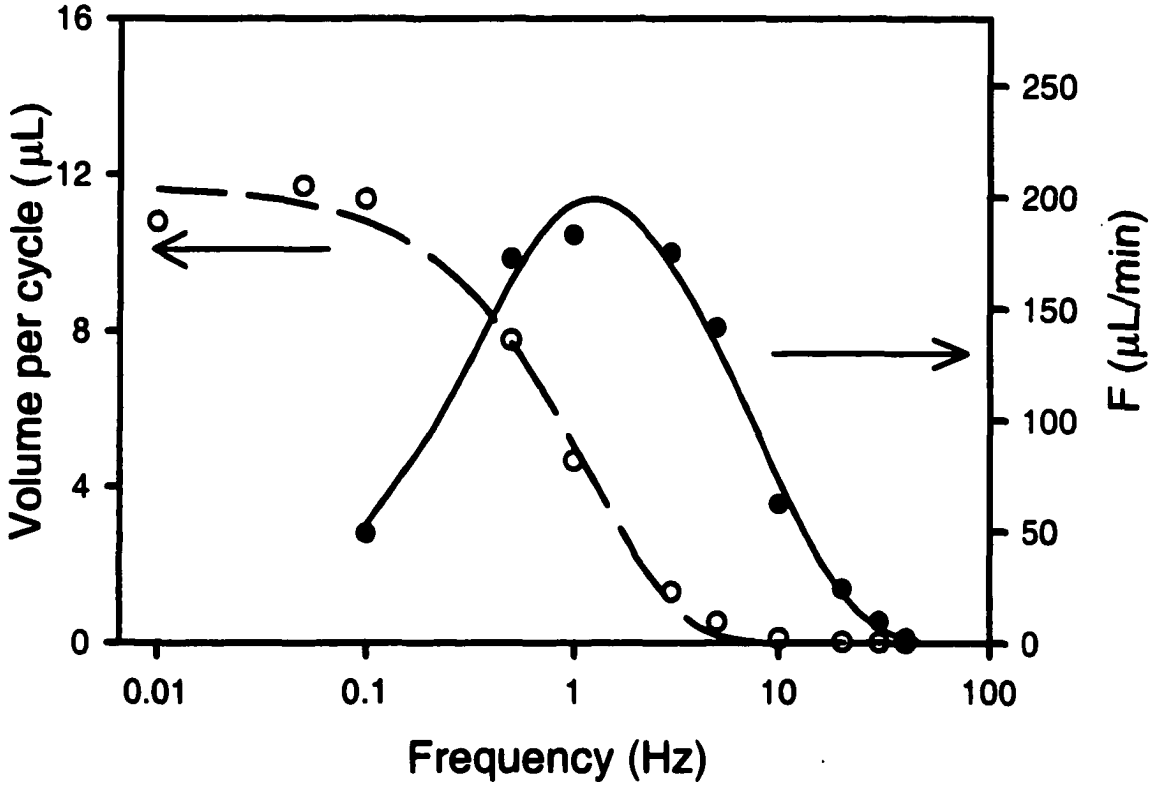
16
12
8
4
0
Volume per cycle (µL)
250
200
150
100
50
0
F (µL/min)
0.01
0.1
1
10
100
Frequency (Hz)

Figure 5.

CHAPTER 2. AN ELECTROCHEMICALLY-ACTUATED MERCURY VALVE FOR FLOW RATE AND DIRECTION CONTROL: FROM DESIGN AND CHARACTERIZATION TO APPLICATIONS IN FLOW INJECTION ANALYSES

A manuscript in preparation for submission to *Analytical Chemistry*

Jing Ni,[1] Shelley J. Coldiron,[1] Chuan-Jian Zhong,[1,2] Marc D. Porter[1,3]

Abstract

An electrochemically-actuated mercury pump was reconfigured to function as a valve for controlling both flow rate and flow direction. The valving mechanism relies on a glass piston, placed on top of a mercury column, to open or block the flow passage. The glass piston is actuated by the movement of the mercury column, based on electrochemically-induced change in the surface tension to the mercury/electrolyte interface. The position of the piston can therefore be controlled by applying different voltages to the mercury electrode, which changes the surface tension of mercury, and therefore the relative height of the mercury columns in the two arms of a U-shaped tube. The extent of the piston displacement opens, closes, or partially opens the flow channel, altering fluid flow rate. We present herein the usage of this concept for both flow rate and direction control, and demonstrate its application in flow injection analyses.

---

[1] Microanalytical Instrumentation Center, Ames Laboratory-USDOE, and Department of Chemistry, Iowa State University, Ames, IA 50011
[2] Current address: Department of Chemistry, State University of New York at Binghamton, Binghamton, NY 13902
[3] Corresponding author

Introduction

The earliest work on a miniature chemical analysis instrument was reported by Terry et al. in 1979 as a chip-scale gas chromatograph.[1] Since then, the development of miniaturized total analysis systems (μTAS) has drawn a great deal of attention from researchers in a wide range of disciplines. Since the behavior of fluids in microfabricated channels (i.e., microfluidics) can be much different from that in more conventional-sized devices, microtechnology offers some unique advantages for chemical analysis extending beyond miniaturization of already existing systems. One of the most important advantages is the possibility for a high degree of integration of miniaturized device components, which allows the development of high-throughput applications. Other advantages include the reduction in sample and expensive reagent consumption, in waste generation, and in analysis time. These attributes are particularly beneficial in the chemical and medical analysis fields.[2]

In order to realize automated miniaturized chemical analyses, the development and integration of all functional hardware components for sample handling, treatment, and detection are necessary. The microvalve is one type of important component in a fluid flow-based analytical system that helps to realize controlled fluid delivery. They can be classified in two categories: active microvlaves (with an actuator) and passive microvalves (without an actuator). Microvalves may be part of a micropump and function as check valves, or work independently to control or change flow direction and flow rate.

Active microvalves are generally used for controlling flow rate and for sample injection. They rely on actuators to open or close the opening to or in a flow channel. The characteristics of this type of device depends strongly on the actuation mechanism. Although almost all the microactuator types have been used to fabricate microvalves for gas flow control,[3] only a few active microvalves have been developed for successfully controlling

liquid flow. Piezoelectric stacks and bimoph-based microactuators are among the few types of actuators that have been successfully exploited to build liquid flow control valves and used for sample injection purposes.[4, 5] Microvlaves based on shape-memory alloys have been developed and used for blood flow rate control,[6] and microvalves driven by thermopheumatic actuators or pH sensitive hydrogels have also been fabricated.[7, 8]

Passive microvalves are mainly used as check valves and attached to each side of a micropump. Several types of operational schemes have appeared, relying, for example, on a silicon cantilever,[9] a suspended polysilicon disk,[10] and a molded silicone rubber float.[11] Key performance parameters for this type of valves include the response time (i.e., the transition time during open-to-close or close-to-open operations), the on-to-off (for injection valve) and forward-to-reverse (for check valve) flow rate ratio, and the pressure tolerance. Electrical requirements, including power, voltage and current, fabrication process complexity, cost, and lifetime are also important application issues.

This paper describes the design and testing of a novel type of active valve which is based on electrochemically-induced surface tension changes. Actuation of the valve relies on the electrocapillarity of mercury, which is usually illustrated by a group of electrocapillary curves (i.e., plots of the change in the surface tension as a function of applied potential and electrolyte composition).[12] These curves generally have parabolic shapes with the maxima in surface tension defined as the potential of zero charge (pzc). Applying potentials more positive or more negative than the pzc causes a decrease in surface tension. Depending on how the mercury is confined in a system, the surface tension change can induce either a shape change of a mercury drop or a mechanical actuation of a mercury column. The shape changes of the mercury are the basis of the well-known mercury beating heart laboratory demonstrations,[13] and optical and electrical switches.[14, 15] The mechanical actuation of a mercury column, on the other hand, was only theorized by Matsumoto et al. in

a micropump format[16], and recently harnessed by Lee et al. as a micromachined mercury motor.[17] In our previous report, we presented the first utility of this actuation principle to drive fluids continuously through glass capillaries by confining mercury within two concentrically-aligned tubes.[18] The fluidic pumping was realized from the repetitive piston-like actuation of a mercury column that resulted from the application of a square waveform across the mercury/electrolyte interface.

In this report, the mercury pump concept is extended for use in a valving format. The same type of electrochemically-induced surface tension change was exploited as the basis for the valve actuation. The function of the valve is demonstrated either as flow rate control valves or as check valves. Several of the parameters for evaluating the performance of a microvalve, including response time, the on-to-off flow rate ratio and pressure tolerance for operation are examined. The mercury-based pump and valves were also integrated into a flow injection analysis (FIA) system to demonstrate applicability to fluidic control and delivery.

Experimental

Chemicals. Mercury (ACS certified) was purchased from Fisher (Caution: hazardous vapor), and subsequently cleaned by three passes through freshly pierced filter paper . Potassium chloride (99+%) and hydrofluoric acid (49%) were also acquired from Fisher. Platinum wires (0.2 mm diameter), Iron(III) chloride (97%) and sodium thiocyanate (98%) were obtained from Aldrich.

Mercury valve. The design of the mercury activated valve is depicted in Figure 1. The design uses an U-shaped glass tube that is filled with mercury. The glass tube, open on both sides, has an inner radius of 0.92 mm and a total length about 10 cm. It was constructed such that one arm is slightly higher than the other. A platinum wire was sealed

through the bottom of the "U" to make electrical contact with the mercury pool. A second platinum wire was used as counter electrode in the higher arm of the U-shaped tube.

The lower arm was connected to the flow channel through a Plexiglas adaptor. The adaptor has a vertical hole with an inner diameter that equals the inner diameter of the U-shaped glass tube. Near the bottom of the adaptor, this vertical hole was enlarged to the size of the outer diameter of the U-tube to facilitate its coupling with the tube. A horizontal (inner radius of 0.42 mm) channel was also drilled near the top of the adaptor, which connected to the vertical hole in a T-shaped geometry. The horizontal channel therefore serves to connect the valving element to the flow channel, whereas the vertical hole provides access for insertion of the glass piston on top of the mercury column. The adapter was sealed to the top of the lower arm of the U-tube, and glass capillaries (inner radius of 0.42 mm) were then connected to both sides of the adaptor.

The glass pistons were fabricated by etching a glass rod in 25% HF to a radius of 0.88 mm, which were then cut to a length of 2 mm. The radius of the piston is only slightly smaller than the internal radius of the vertical hole of the adaptor, insuring both smooth vertical movement of the piston in the adaptor, and providing the necessary seal against the two orifices that connect the vertical hole to the flow channel. The weight of the piston is 0.12 g.

In assembling the valve, freshly cleaned mercury was first pipetted into the U-shaped tube. The glass piston was then placed on top of the mercury column in the lower arm through the top of the vertical hole in the adaptor. In the higher arm, aqueous electrolytic solution (0.1 M KCl) was introduced on top of the mercury column, forming a mercury/electrolyte interface. Next, the platinum counter electrode was immersed in the electrolyte, which completed the electrical circuit for controlling the surface tension through changes in applied voltage. After sealing the top of the vertical hole with a small piece of

adhesive Teflon tape, the fluidic channels were primed by applying a pressure carefully to the solution inlet with a syringe. Once the flow channel and the space above the glass piston were filled with solution, the position of the piston was adjusted by adding or removing mercury from the higher arm of the U-tube until the piston fully blocked the flow channel at the open circuit potential.

Flow rate determinations. To test the performance of the valve for fluidic control, one end of the flow channel was connected to a solution reservoir filled with deionized Water. The other end of the channel was then positioned over a collection reservoir that was placed on an analytical balance (Ohaus E400). The flow rate was determined by weighing the water added to the collection reservoir per unit time, and then converting the weight to volume based on the density of water.

To test the valve as an element for controlling flow rate, the water level on the inlet side of the channel was positioned higher than the level at the outlet. The resulting height difference induces fluid flow hydrodynamically. A Ag/AgCl (sat'd KCl) reference electrode was added to the system and also immersed in the electrolyte solution. It was incorporated to control precisely the applied voltage across the mercury/electrolyte interface using a potentiostat (Bioanalytical Systems CV-27) in a three-electrode configuration. Flow rates were determined at several different applied voltages under the same gravity feed condition.

The check valve function was demonstrated by connecting three of our U-shaped mercury columns in series. Square waveforms at same frequency and with same positive (-1 V) and negative (-3 V) limits were applied to each of the mercury columns in a two-electrode configuration. The three applied waveforms were offset with respect to each other by a preselected phase, and supplied from the outputs of an in-house built function generator.[19] Flow rates were measured in the same way as described above, except that the height of the solution inlet and outlet were kept the same in order to avoid gravity-

induced flow. Flow rates under different conditions, including different frequencies and phase shifts, were compared.

Flow injection analysis. The mercury-based pump, injection valve, and the flow cell for optical detection were assembled through flow channels (inner radii of 0.42 mm) connected together with heat-shrinkable tubing. The schematic representation of the integrated FIA assembly is shown in Figure 2. The pump/check valve unit was supplied with three square waveforms, each at a 90° phase shift with respect to the other. All the waveforms have a frequency of 1 Hz, with one voltage limit at –1 V and the other at –3 V. These conditions resulted a flow rate of 215 mL/min in a 30-cm long flow channel. Gravity-induced flow was not used for fluid delivery in the FIA setup.

The flow rate control valve was also employed for sample injection. A voltage pulse of –2 V vs. Ag/AgCl (sat'd KCl) opens the injection valve, and different amounts of the $FeCl_3$ (1.0 mM) sample was pumped into the flow channel by altering duration of the voltage pulse. A solution of NaSCN (0.10 M) was used as running buffer, and it forms a $FeSCN^{2+}$ complex that has an absorbance maximum at 474 nm.[20] Detection was accomplished using a 1-cm path length flow cell (1-mm diameter), housed in a UV-Vis spectrometer (HP 8453), with the absorbance recorded every 5 s using the kinetic mode of the HP Chem Station software.

Results and Discussion

Concept. The following sections describe the design and testing of a novel type of active valve. The valving element is a glass piston actuated by an underlying mercury column, i.e., the mercury actuator. Actuation is based on the same fundamental mechanism that we exploited recently in the design of a mercury-based pump: the electrochemically-induced surface tension change at mercury/electrolyte interface.[18]

However, the geometry of the mercury actuator for valving is changed from two concentrically aligned mercury columns, which was used in the pump, to a single U-shaped column. The remainder of this section briefly describes the actuation concept.

At the open circuit potential, the heights of the mercury columns in the two arms of the U-shaped tube are the same, as shown on the left-hand side of Figure 1. Upon applying a voltage that decreases the surface tension of mercury in the right arm of the tube, the U-shaped mercury column shifts from left arm to right arm until a new equilibrium is reached. As shown on the right-hand side of Figure 1, this shift lowers the piston in the left arm of the tube, while the mercury in the right arm is elevated. This change in relative height (Δh), and hence pressure (ΔP) are given by the formulations of Young and Laplace in Equations 1 and 2:[21]

$$\Delta h = 2\frac{\Delta\gamma}{R\rho g}\cos\theta \qquad (1)$$

$$\Delta P = \rho g \Delta h \qquad (2)$$

where $\Delta\gamma$ is the electrochemically-induced change in the surface tension of mercury in the right arm, R is the internal radius of the U-shaped tube, ρ is the density of mercury, g is the gravitational acceleration, and θ is the contact angle of the mercury at the mercury-tube wall interface. These equations describe the equilibrium relationship between interfacial and gravitational forces, which establish the relative heights of the two mercury meniscuses in each arm of the tube.

The U-shaped design offers several advantages over our earlier construction using concentrically-aligned mercury columns, especially when adapted for building a mercury-based valving system. As depicted in Figure 1, the initial piston position in the lower arm of the U-tube is very critical and has to be high enough to block fully the flow channel when the

applied voltage is near the pzc. The U-shaped tube design facilitates adjustment of the piston position by adding or removing mercury from the other arm of the tube; since the arm on the right side of the tube is not directly connected to the flow channel, no disassembling or re-priming is required. We also found that filling a small cavity with mercury in our earlier design could be complicated because of the high surface tension of mercury. The new design solves the filling difficulty by allowing mercury to be drawn into the U-shaped tube by applying carefully a vacuum to one end. Since only one tube is used, no alignment of the cylinders is required, an attribute which also makes the new design more readily adaptable for miniaturization. The following sections present the results of using our electrochemically actuated valves for controlling flow rate, achieving one-directional flow, and injecting samples in a FIA demonstration.

Flow rate control valve. According to Equation 1, a change in surface tension ($\Delta\gamma$) leads to a difference in the height (Δh) of the mercury column, which in turn alters the position of the piston. Therefore, the extent of piston displacement, which can be adjusted by varying the mercury surface tension through changes in applied voltage, can be used to open, close, or partially open a flow channel, and therefore alter the fluid flow rate.

Figure 3 demonstrates this concept. The data connected by the solid lines represent the results of two separate sets of measurements using the same valve unit. In both cases, the valve shuts off the flow when the applied voltage is positive of –0.8 V (i.e., the threshold voltage, V_{th}). At and above the V_{th}, the piston completely blocks the flow channel. In contrast, when the applied voltage is negative of –1.8 V (i.e., the saturation voltage, V_{sat}), the piston descends to a height where the flow channel is fully open, resulting in the maximum observed flow rate. Between V_{th} and V_{sat}, the piston partially blocks the channel, with the flow rate controlled by adjusting electrochemically the height of the mercury column and hence the extent in which the piston protrudes into the channel.

The dashed line in Figure 3 shows the same experiment using a second U-tube and piston assembly. This valve opens and closes at different applied voltages. Indeed, both the V_{th} and the V_{sat} for this valve are shifted negatively by ~0.3 V from those for the first valve. We attribute this offset to a subtle difference in the initial position of the piston relative to the openings in the top and bottom of the flow channel. In other words, the piston in this valve probably protruded further into the opening at the top of the flow channel, and therefore a more negative voltage needed to be applied in order to allow the piston to drop to a height low enough to open fully the flow channel. Between V_{th} and V_{sat}, which also covers a range of ~1 V, the flow rate increases with the magnitude of the applied voltage in the same manner as observed previously.

An interesting result is obtained when calculating the theoretical height change of the piston for this 1 V window. Based on the electrocapillary curve of mercury in 0.1 M KCl,[22] this voltage window causes a surface tension change of ~150 dynes/cm. Using a R of 0.92 mm, ρ of 13.6 g/cm^3, g of 9.8 N/Kg, θ of 135°, and $\Delta\gamma$ of 150 dynes/cm gives via Equation 1 a Δh of 1.72 mm. This Δh translates to an increase of 0.86 mm in height of the mercury column on the side of the U-shaped tube where the voltage is applied, and a decrease of 0.86 mm for the column and piston in the arm connected to the flow channel. We note that the i. d. of the flow channel is 0.84 mm, which is the minimum distance required for the piston to move from a position where the channel is fully open to one in which the channel is completely blocked. Thus, the calculated piston displacement that results from the 1-V change in applied voltage is very close to the minimum travel needed to fully open or fully close the valve.

Switching the applied voltage between a value equal to or slightly positive of the threshold voltage ($V_{off} \geq V_{th}$), and a value equal to or slightly negative than the saturation voltage ($V_{on} \leq V_{sat}$), the flow rate control valve can also function as a sample injector. At V_{off},

the flow channel connected to the sample reservoir is blocked by the piston, and no sample can move into the flow stream. The sample solution can be delivered into the flow system by changing the applied voltage to V_{on}, which causes the piston to descend and in effect open the injection valve. Once the desired amount of sample is delivered, the applied voltage is switched back to V_{off}, and the injection is complete.

Two important characteristics for a sample injection valve were studied: the on-to-off flow rate ratio and the pressure tolerance level. The on-to-off flow rate ratio is diagnostic of the leakage of the valve, noting that the higher this ratio, the better the performance. The pressure tolerance level defines the pressure range under which the valve opens and closes correctly; the wider this range, the greater the applicability of the valve. Figure 4 shows the flow rates measured at -0.5 V (V_{off}) and –2.0 (V_{on}) under different pressures. The pressure was increased by increasing the height of the solution inlet while maintaining a constant height for the outlet. The on flow rate (open circles) increases linearly with the inlet pressure, and is consistent with the expectation based on the Poiseuille's equation.[23] The off flow rate (closed circles) shows that no fluid flow is observed until the pressure becomes greater than ~250 Pa.

The non-detectable leakage of the valve at low pressures suggests an effective fitting of the piston and the vertical hole in the adapter. Thus, the piston function reliably as a valve in this pressure range. The increased fluid flow above 250 Pa defines the upper limit for the pressure tolerance of this valve, which is fundamentally determined by the nature of the mercury actuator. Based on the voltage change (i.e., from –0.5 V to –2.0 V vs. Ag/AgCl, sat'd KCl) and the established electrocapillary curve for measuring in 0.1 M KCl,[22] Equations 1 and 2 predict a ΔP of ~300 Pa. This ΔP suggests the pressure that can be utilized for moving the piston, and it matches reasonably well with the experimentally determined upper limit of the pressure tolerance for this valve. Equations 1 and 2 also

suggest that using a U-shape tube with a smaller *R* can generate a higher pressure from the actuator, and therefore increase the pressure tolerance of the valve and enhance the valve performance.

Check valve. Flow direction control can be achieved by positioning a mercury-actuated valve on each side of a mercury-actuated pump. The relative movements of the mercury columns in the two valves and in the pump are determined by the phase of the waveform applied to each mercury column. Figure 5, which shows three mercury columns connected to the flow channel in series, presents the concept. The middle column, which is shown as having a larger radius than the surrounding columns, functions as the pump. The columns on each side of the pump then serve as active check valves. Thus, by judicious selection of the phase for a voltage waveform applied to each column, one-directional fluid flow can be realized. The square waveforms applied to each mercury column are shown at the top of this figure. At one limit in the waveform, V_{off}, the applied voltage causes the mercury to ascend and block the flow channel (e.g., V_{off} = pzc). At the other limit, V_{on}, the applied voltage causes the mercury to descend and open the flow channel (e.g., V_{on} < pzc). All three of these waveforms are set at same frequency and having the same voltage limits, but with different phases. The illustration in Figure 5 shows that the phase of the waveform applied to the middle column is 90° behind that applied to mercury column on the right, but 90° ahead of that applied to the mercury column on the left.

Figures 5A-D illustrate the position of each piston and the track of the fluid flow at every quarter of the full period of the waveform. Initially, all of the pistons are fully extended into the flow channel. As the cycle begins (Figure 5A), the valve on the right is supplied with a voltage that causes it to open. Due to the phase shift of the three waveforms, the pump and the valve on the left side remain closed. During the second quarter of the period (Figure 5B), the voltage applied to the pump is switched to a value that causes the mercury

column and hence the piston to descend. At this point in the cycle, the pump draws liquid only from the right-hand side of the flow channel, as determined by the status of the two valves. In the third quarter (Figure 5C), the valve on the left-hand side opens at the same time as valve on the right-hand side valve closes. This step sets the flow direction for the final quarter of the period. In the last quarter of the period (Figure 5D), the voltages applied to the two valves are held the same as those in the third quarter, while that applied to the mercury pump is switched to V_{on}. This process causes the mercury pump to extend, pushing the liquid to the left through the flow channel. The second full period then starts again, and the ensuing peristaltic motion of the three mercury columns results a continuous unidirectional flow of fluid from right to left. The valve on the left therefore functions as an outlet check valve, while the valve on the right functions as an inlet check valve.

Table 1 summarizes the flow rate data measured at different actuation frequencies. As is evident, flow rate increases with frequency until ~4 Hz, where the flow rate then starts to decrease. This observation is consistent with our previous findings using a single mercury pump.[18] That is, the decrease in flow rate is a result of the inertial time constant of the system in which the movement of the mercury and piston can not fully track the electrical stimulation at high frequencies. We have demonstrated with the single pump that this time constant can be reduced by decreasing the radius of the mercury column, which expanded the actuation frequency to a higher upper limit, yielding a higher flow rate.

Table 2 lists the flow rates measured when the three mercury columns were actuated at different phase shifts. A higher flow rate is indicative of a more efficient peristaltic motion and/or a higher check valve efficiency (i.e., higher forward-to-reverse flow rate ratio). At a 180° phase shift, no net flow rate was detected as the solution being moved only between the mercury pump and the valves on each side. More importantly, when increasing the phase shift from 180° to 360°, the net fluid flow moves in the opposite

direction of that for phase difference of 0-180°, demonstrating the flow direction can be reversed simply by changing the phase shift of the waveforms. For example, applying waveforms with 270° phase shift in stead of 90° phase shift, alters the net flow from the right-to-left to the left-to-right at almost the same flow rate. Thus, the valve on the right becomes an outlet check valve, while the valve on the left becomes an inlet check valve. Compared to conventional approaches for flow direction control, which usually require the reconstruction or rearrangement of the two check valves, this approach makes directional control much easier.

Integrated flow injection analysis. The mercury pump, check valves, and sample injector were integrated together to demonstrate their utility in a miniaturized FIA system. Figure 2 is a schematic diagram of our single-line FIA manifold. The pump/check valve unit induces and regulates fluid flow in the direction shown by the arrows. When the injection valve is closed, only the carrier solution flows through the channel. The sample solution is then injected by application of a negative voltage pulse to the mercury column in the injection valve; this lowers the piston, opens the valve, and the sample solution is then pumped into the flow stream together with the carrier. Mixing is accomplished by the diffusion of the sample zone in the carrier stream, and the reaction product is detected optically at the end of the flow channel.

Figure 6 shows a set of experimental results collected from this single-line setup. An aqueous solution of 0.10 M NaSCN was used as carrier, and different amounts of a 1.0 mM $FeCl_3$ solution were injected into the carrier stream by opening the injection valve for different periods of time. As expected, the absorbance of the formed $FeSCN^{2+}$ complex increases with the injection time, and therefore with the amount of the injected Fe^{3+}.[20] The insert further demonstrates the linear relationship between the absorbance and the injection time, with a regression coefficient (r^2) of 0.99. The linear regression curve, shown as the

solid line in the insert, however, does not pass the origin, intercepting the absorbance-axis at 0.09 A. U. We attribute this non-ideality to the approximation of injection volume by using the injection time. In addition to the amount of sample that flows into channel during an injection, sample is also injected during the closing of the valve because of the volume displacement of the elevated piston. This situation makes the total analyzed sample greater than what is represented by the injection time, resulting in the non-zero response at zero injection time. The dead volume of the injection valve, which can cause the tailing of the observed absorbance peaks, is determined by the distance between the piston and the T-junction where the sample and the carrier meet. Therefore, shortening this distance should reduce the dead volume of the injection valve. Finally, the similar absorbances (0.1129 and 0.1273, respectively) of the first two peaks in Figure 6, which are the results from two repetitive 5-s injections, indicate the reproducibility of the overall process.

Other types of FIA experiments have been examined using this setup. For example, we have conducted an acid-base titration by using the absorbance signal collected upon injecting different volumes of a NaOH solution into a HCl/methyl red carrier stream. A FIA of cerium(IV) sample was also demonstrated based on a redox reaction between cerium(IV) and ferrocyanide, which was present in the carrier solution. Taken together, these results provide a strong foundation for the continued development of this novel mercury-based system for fluid delivery.

Conclusions

In this report, we have constructed and examined the performance of electrochemically-actuated mercury valves for controlling flow rate and flow direction. The applicability of these valves was demonstrated as sample injection valves and check valves in a single-line flow injection analysis setup. Valving is realized by using an

electrochemically-actuated mercury column to lift a glass piston (~0.12 g) by a distance of 1-2 mm into a flow channel and block fluid flow. The performance of the valve, in terms of pressure tolerance, response time, and electrical requirements therefore are mainly determined by the mercury actuator. The voltage required for operating such a valve is about 2 V, the current is a few milliamps, and the power consumption is therefore in the milliwatt range. These electrical requirements will facilitate the planned miniaturization. In addition, the U-shape mercury column design requires no alignment and is easy to assemble, which simplifies the fabrication process. To meet the needs of the chemical analysis, experiments to enhance the valve performance and further integrate the fluidic delivery system with improved reliability are underway.

Acknowledgments

J. N. gratefully acknowledges the support of the ACS Analytical Division Fellowship that is sponsored by the Eastman Chemical Company. We express our appreciation to Mike Granger for the valuable discussion. This work was supported by NASA (Grant #NAGW4951) and by the Microanalytical Instrumentation Center of Iowa State University.

References

(1) Terry, S. C.; Jerman, J. H.; Angell, J. B. *IEEE Transactions on Electron Devices* **1979**, *26*, 1880.

(2) Harrison, D. J.; Berg, A. v. d. , Banff, Canada 1998; Kluwer Academic.

(3) Shoji, S.; Esashi, M. *Micromech. Microeng.* **1994**, *4*, 157.

(4) Shoji, S.; Esashi, M. *Chem. Sens. Tech.* **1988**, *1*, 179.

(5) Esashi, M. *Sens. Actuators* **1990**, *A21*, 161.

(6) Shoji, S.; Esashi, M.; Matsuo, T. *Sens. Actuators* **1988,** *14*, 101.

(7) Zdeblick, M. J.; Anderson, R.; Jankowski, J.; Kline-Schoder, B.; Christel, L.; Miles, R.; Weber, W. *Solid-State Sensor and Actuator Workshop* **1994**, 251.

(8) Beebe, D. J.; Moore, J. S.; Bauer, J. M.; Yu, Q.; Liu, R. H.; Devadoss, C.; Jo, B.-H. *Nature* **2000,** *404*, 588.

(9) Tiren, J.; Tenerz, L.; Hok, B. *Sens. Actuators* **1989,** *18*, 389.

(10) Esashi, M.; Shoji, S.; Nakano, A. *Sens. Actuators* **1989,** *20*, 163.

(11) Shoji, S.; Schoot, B. H. v. d.; Rooij, N. F. d.; Esashi, M. *Sens. Actuators* **1992,** *A32*, 335.

(12) Bard, A. J.; Faulkner, L. R. *Electrochemical Methods: Fundamentals and Applications*; John Wiley and Sons: New York, 1980.

(13) Lin, S.-W.; keizer, J.; Rock, P. A.; Stenschke, H. *Proc. Nat. Acad. Sci USA* **1974,** *71*, 4477.

(14) Jackel, J. L.; Hackwood, S.; Beni, G. *Appl. Phys. Lett.* **1982,** *40*, 4.

(15) Beni, G.; Tenan, M. A. *J. Appl. Phys.* **1981,** *52*, 6011.

(16) Matsumoto, H.; Colgate, J. E. *IEEE Micro Electro Mechan. Sys.* **1990**, 105.

(17) Lee, J.; Kim, C.-J. *IEEE Micro Electro Mechanical Systems Workshop* **1998**, 538.

(18) Porter, M. D.; Zhong, C.-J.; Ni, J.; Coldiron, S. J.; Tang, W. C. *SAE Technical Paper Series*, Lake Tahoe, Nevada, July 14-17, 1997 1997; 972420.

(19) Coldiron, S. J.; Kodis, J.; Englieg, A.; Smith, C. *manuscript in preparation* .

(20) Harris, D. C. *Quantitative Chemical Analysis*, 5th ed.; W. H. Freeman and Company, 1998.

(21) Adamson, A. W. *Physical Chemistry of Surfaces*; John Wiley and Sons: New York, 1990.

(22) Grahame, D. C. *Chem. Rev.* **1947,** *41,* 441.

(23) Giancoli, D. C. In *Physics: Principles with Applications*; Prentice-Hall, Inc: Englewood Cliffs, NY, 1980, pp 147.

Table 1. Net flow rate obtained from the pump/check valve assembly, measured at different frequencies. The voltage waveforms are at a 90° phase shift, with the V_{off} and V_{on} at −1 and −3 V, respectively.

f (Hz)	F (μL/min)[a]
0.5	125
1	225
2	314
3	384
4	443
5	303
7	164
10	Not measurable

[a] The uncertainty of the flow rate measurements is about ±5%.

Table 2. Net flow rate obtained from the pump/check valve assembly, measured at different phase shifts. The square voltage waveforms are at 1 Hz, with the V_{off} and V_{on} at −1 and −3 V, respectively.

Phase shift (°)	F (μL/min)[a]
30	274
60	274
90	213
120	169
150	137
180	Not measurable

[a] The uncertainty of the flow rate measurements is about ±5%.

Figure Captions

Figure 1. A schematic representation of the close and open modes of the mercury-based valve as a result of application of a voltage step across the mercury/electrolyte interface. Mercury (shown in black) fills both arms of the U-shaped tube. The electrolyte solution (shown in blue) is introduced to top of the mercury in the higher arm while a glass piston (shown in green) is placed on top of the mercury in the lower arm. A flow channel connects with the lower arm in a "T" arrangement. Two platinum wires (shown in purple), one making contacted with mercury and the other as counter electrode and immersed in the electrolyte, are also incorporated.

Figure 2. A schematic diagram that depicts the single-line flow injection analysis setup. The key components of this setup includes a mercury pump/check valve assembly, an injection valve, a flow channel, and a detector. See text for details.

Figure 3. Control of flow rate of water by electrochemically-changing the piston position in the flow channel. Solution flow is induced by raising the water level at the inlet channel 2.5 cm higher than that of the outlet. This height difference corresponds to a pressure difference 247 Pa. Two of the three sets of results (▲,▼) were obtained using the same valve assembly, whereas the third set of the results (●) represents data from a different U-tube and piston assembly.

Figure 4. On and Off flow rates as a function of the fluid pressure. The open circles are the flow rates measured when the valve is open, which results from applying –2.0 V (vs. Ag/AgCl, sat'd KCl) to the mercury column. The closed circles represent the flow rates measured when the valve is closed by changing the applied voltage to -0.5 V. The pressure was increased by increasing the height of the solution inlet while keeping the outlet height the same. The error bar shows the standard deviation from three different flow rate measurements.

Figure 5. A schematic illustration of using two active mercury-based check valves to realize unidirectional flow. The three waveforms applied to the mercury columns are shown at the top, and the vertical dashed lines divide the full period of a waveform into four quarters. V_{on} represents the limit of the waveform that causes the valve to open, and V_{off} is the limit of the waveform that causes the valve to close. The three waveforms are offset by 90° from right to left. The position of each piston and the track of the flow at each quarter of the period are given from A-D. Only the lower arms and the "T" sections of three U-shape mercury columns are represented (in gray). The glass pistons are shown in green, and the solution is shown in red. A net flow from right to left is achieved with this actuation scheme.

Figure 6. The flow injection results obtained using the single-line setup. The plot shows the absorbance response after injecting different amounts of 1.0 mM $FeCl_3$ sample into a 0.10 M NaSCN flow stream (flow rate = 215 mL/min). The absorbance at 474 nm was recorded at 5-s intervals. The insert shows the linear relationship between the absorbance and the sample injection time.

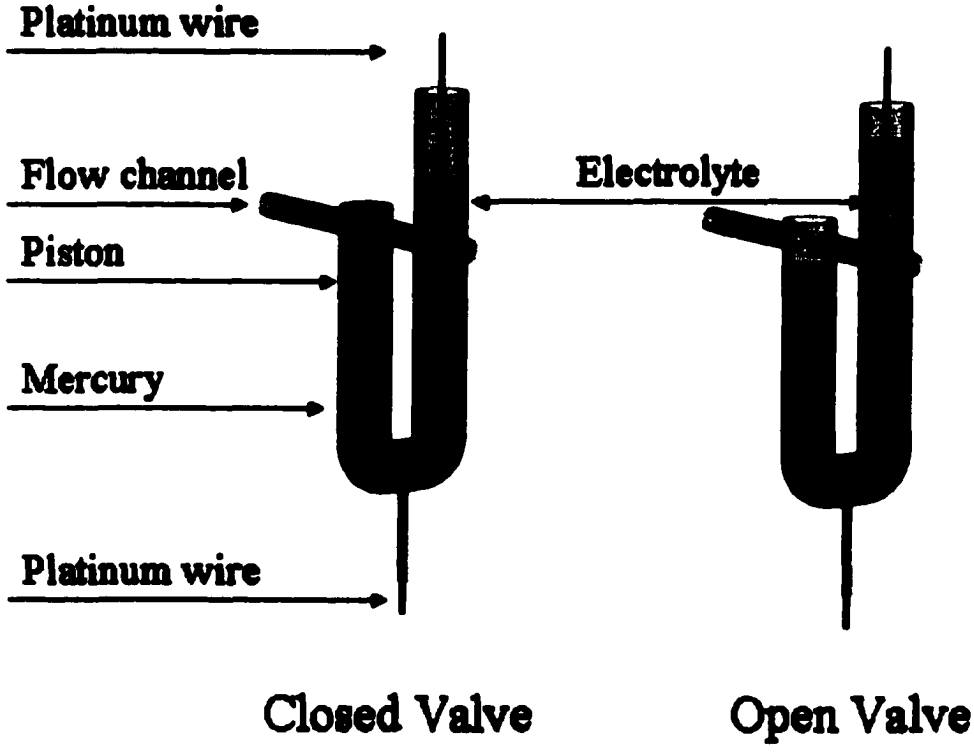
Platinum wire
Flow channel
Piston
Mercury
Platinum wire
Electrolyte
Closed Valve
Open Valve

Figure 1.

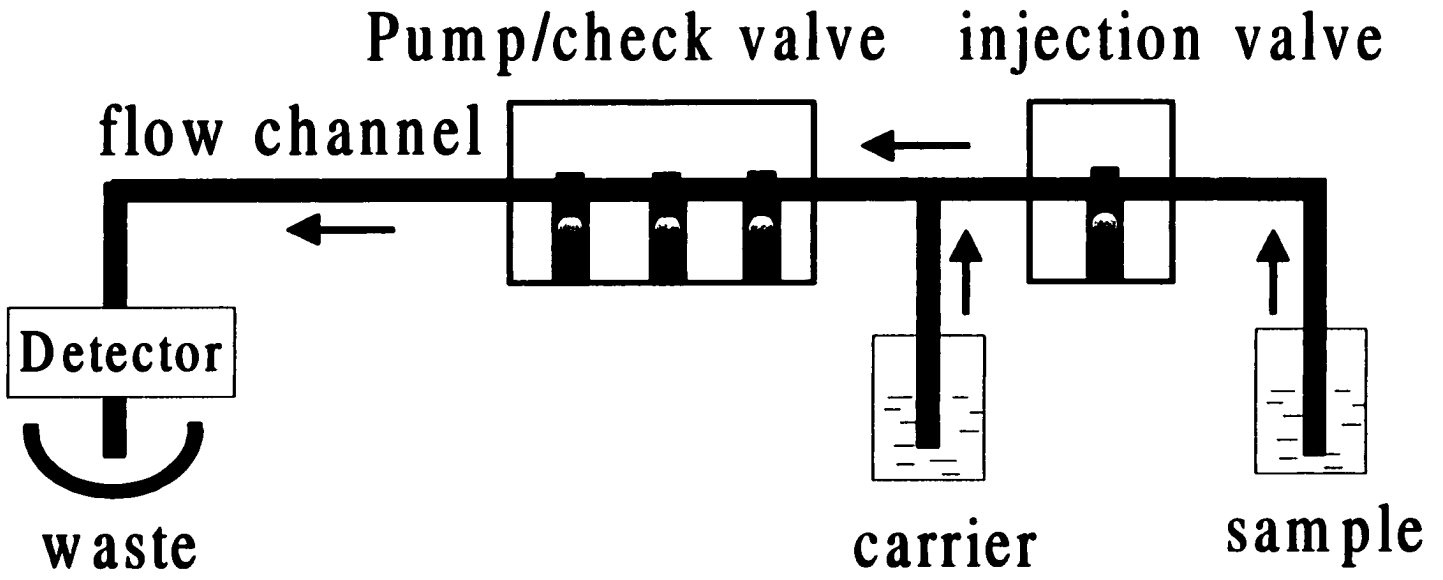
Pump/check valve
injection valve
flow channel
Detector
waste
carrier
sample

Figure 2.

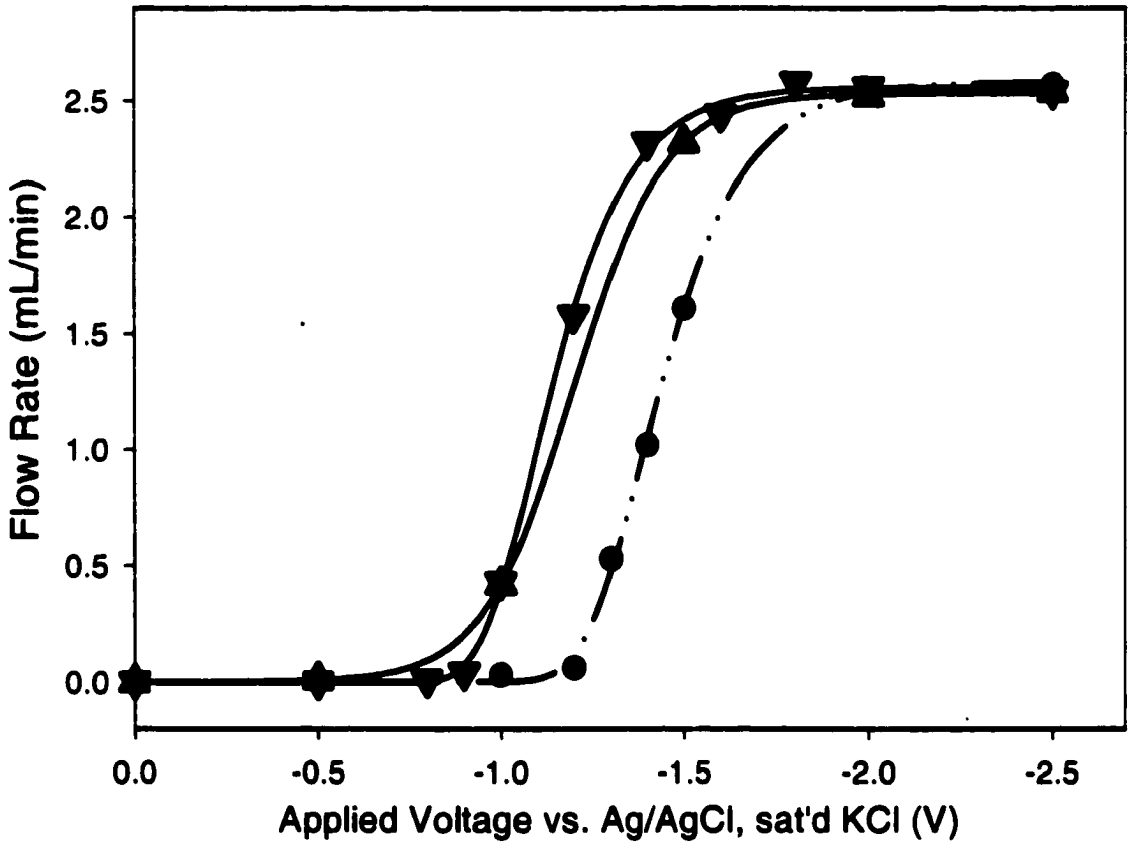
Flow Rate (mL/min)
2.5
2.0
1.5
1.0
0.5
0.0
0.0
-0.5
-1.0
-1.5
-2.0
-2.5
Applied Voltage vs. Ag/AgCl, sat'd KCl (V)

Figure 3.

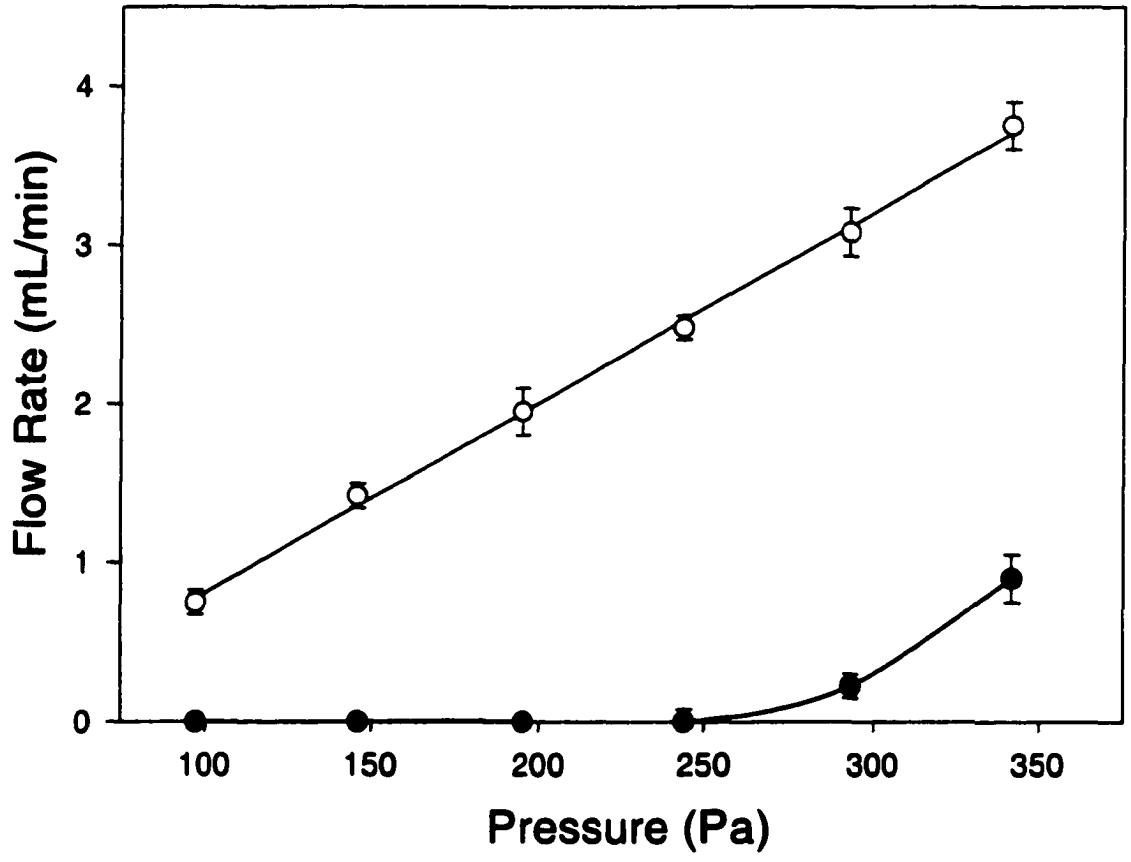

Figure 4.

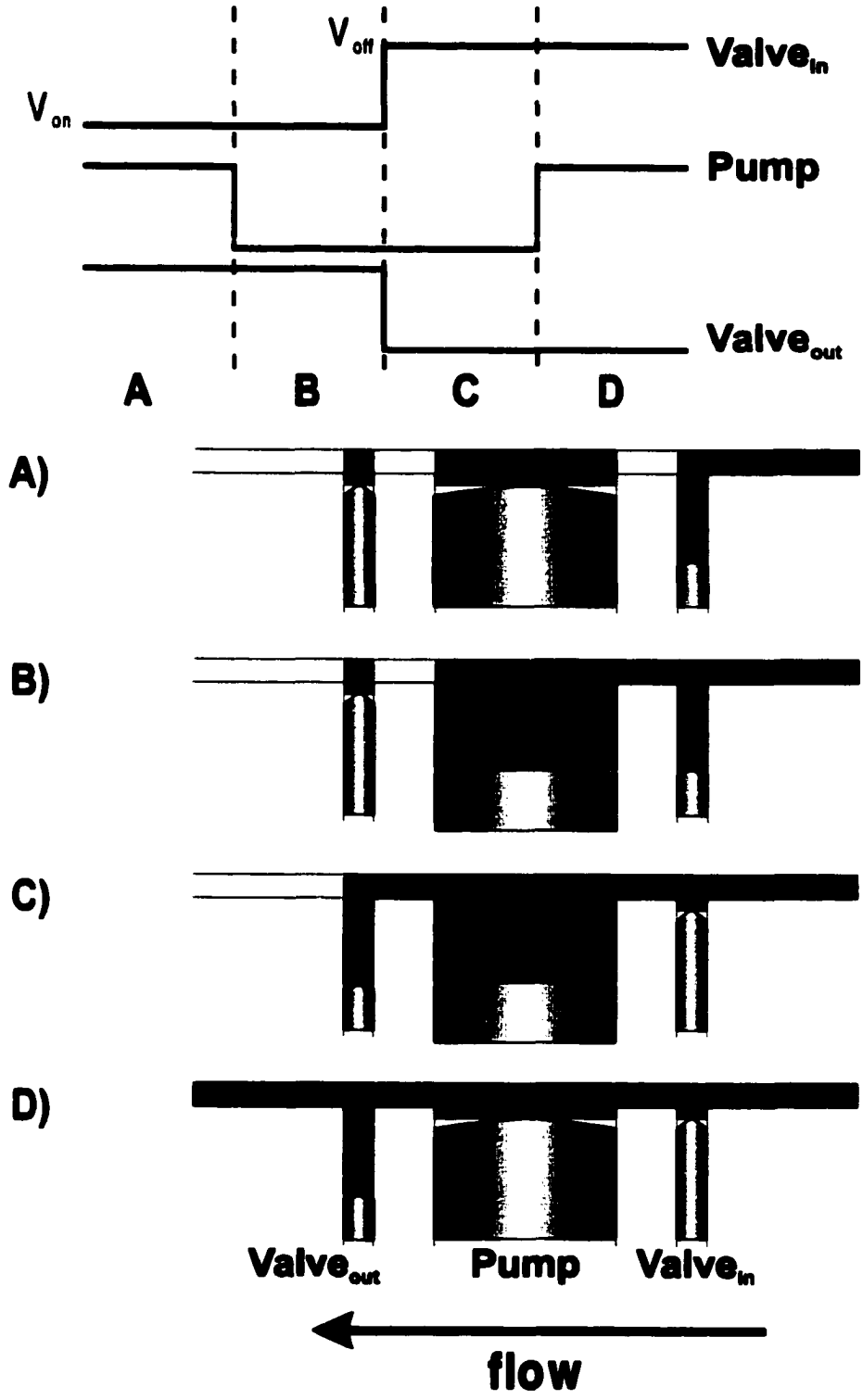
V off
Valve in
V on
Pump
Valve out
A
B
C
D
A)
B)
C)
D)
Valve out
Pump
Valve in
flow

Figure 5.

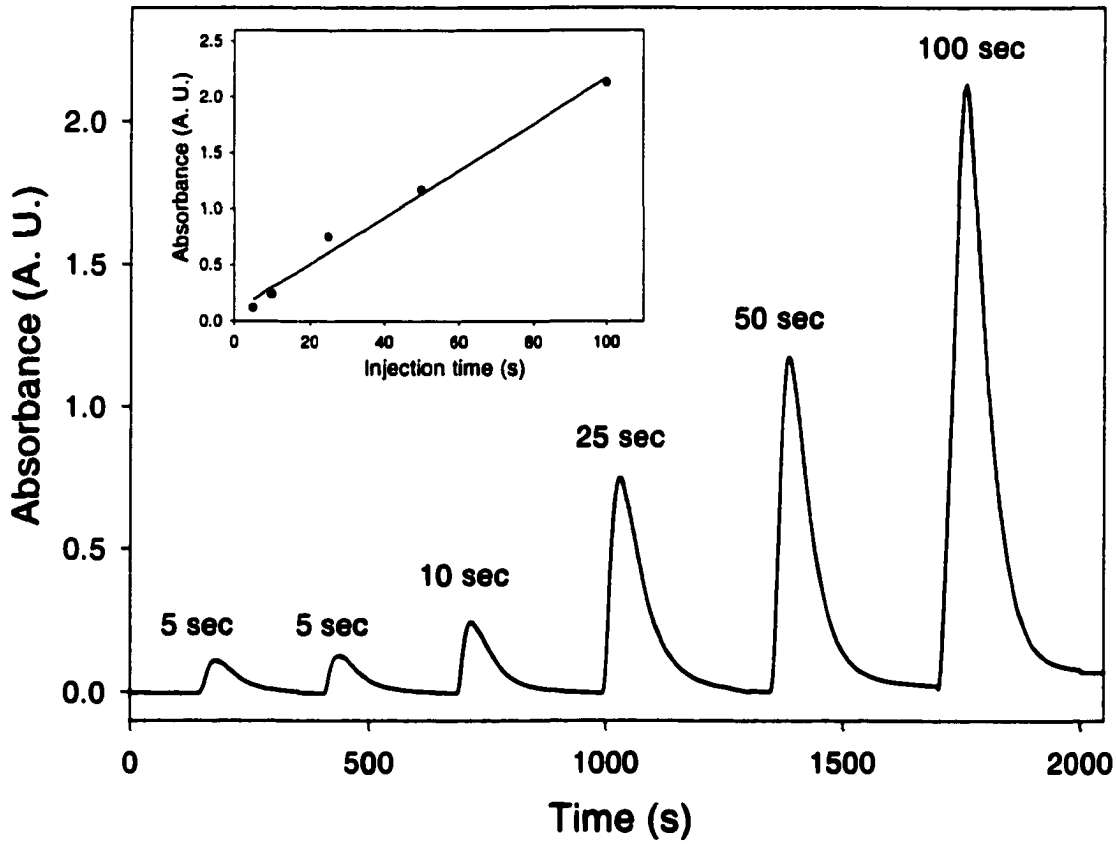
Absorbance (A. U.)
Time (s)
0.0
0.5
1.0
1.5
2.0
0
500
1000
1500
2000
5 sec
5 sec
10 sec
25 sec
50 sec
100 sec
Absorbance (A. U.)
Injection time (s)
0.0
0.5
1.0
1.5
2.0
2.5
0
20
40
60
80
100

Figure 6.

CHAPTER 3. DESIGN, FABRICATION AND TESTING OF MICROCOLUMNS FOR MINIATURIZED LIQUID CHROMATOGRAPHY

Abstract

This paper describes the design, fabrication, and testing of chip-scale columns for incorporation in miniaturized liquid chromatographic instruments. This approach exploited standard microfabrication techniques to build microchannels and electrodes on planar glass substrates. Separations of two fluorescent dyes were demonstrated using these microfabricated channels based on either an open-tubular liquid chromatography (OTLC) format or an electrochemically-modulated liquid chromatography (EMLC) format. Both surface modification and applied potential were demonstrated that can affect the separation. The potential application of such columns in a microfluidic array is also briefly discussed.

Introduction

Research in many areas of chemical and biological analyses has been moving rapidly towards the development and use of miniaturized instrumentations.[1-4] Microfluidic devices represent one type of these so-called "lab-on-a-chip" systems in which sample handling and processing are conducted via microchannel networks. The ultimate goal of these efforts is to use such systems in realizing a reduction in sample and reagent consumption, in analysis time, and an enhancement in the collection of data when characterizing a large number of samples.[3, 5, 6]

In order to realize automatic chemical analysis, the development and integration of the individual components for a microfluidic device are necessary.[7] Figure 1 shows a basic flow-based analytical system consisting of microfabricated flow channels or columns,

miniaturized detectors, and flow delivery and control units such as micropumps and microvalves.

Microfluidic channels are generally utilized for sample separation and sample processing on a chip. They have been fabricated in many types of materials, ranging from silicon[8, 9] and glass[10] to a variety of polymers.[11] Silicon and glass machining techniques have been adopted mainly from the integrated circuits (IC) industry. Indeed, the first commercial microfluidic-based lab-on-a-chip device, i.e., the HP 2100 Bioanalyzer, was built on a glass substrate to perform DNA analysis. Recently, more attention has been given to polymeric substrates.[12-15] Since polymers differ from one another in their mechanical properties, optical characteristics, temperature stability, and chemical resistivity, it is generally believed that there is a suitable polymer material for nearly every application.

In the past two decades, scientists have focused on miniaturizing the analytical systems that are the workhorses in modern analytical laboratories. In 1979, researchers at Stanford University fabricated a gas chromatographic air analyzer, the first chip-scale analytical device fabricated on a silicon wafer.[16] Several miniaturized flow injection analysis (FIA) systems have also been integrated onto a planar plastic substrate.[17, 18]

Among the miniaturized analytical devices, capillary electrophoresis (CE) chips[19-22] have been most explored, with examples including DNA sequencing[23, 24] and immunoassays.[25-27] The focus on CE stems on the ease in which the hardware for fluidic control and delivery can be miniaturized. However, relying on electrokinetic pumping in fluidics limits the range of sample types that can be addressed by CE-based devices. For example, electrokinteic pumping is very sensitive to fluidic properties such ionic strength, pH, and the amount of organic materials in the sample and running buffer. It is therefore difficult to rely on this mechanism to deliver biological fluids such as blood and urine, whose high ionic strength leads to excessive Joule heating in the flow channel. Joule heating also

limits the flow rate and dimensions of the channel. Another challenge is the difficulty in matching the voltage at every channel junction, which is required to control flow direction and to avoid band broadening. Finally, since high voltages are applied to the running buffer, bubbles are sometimes generated due to hydrolysis, causing discontinued electric field and interrupting fluid flow.

Considering the limitations of a CE-based device, several reports exploring the design and construction of pressure-driven chip-scale liquid chromatographs (LC) have appeared.[28, 29] Although individual components, such as micron-sized pumps, valves, flow channels, and detectors have been developed in many implementations,[30-34] integration of these components to meet the requirements for performing chemical analysis remains a major obstacle. These requirements include the ability to delivery liquid precisely at very low flow rates, to inject and detect sample components in extremely small volumes, and to obtain high separation efficiencies.

Recently, we have reported on our efforts towards constructing fluidic delivery systems based on electrochemically-induced change in surface tension.[35] In this paper, we present the results of our efforts to fabricate microfluidic channels and to use them in test separations. The potential application of these devices in an array format to perform miniaturized combinatorial liquid chromatography analyses will also be discussed.

Experimental

Chemical reagents. Two fluorescent dyes, fluorescein, sodium salt (Aldrich) and rhodamine B (Aldrich) were used as analytes to demonstrate separations in microfluidic channels. Mixtures of the two dyes were prepared in deionized water, each at a concentration of 5 ppm. The mobile phase was made of 0.01 M sodium tetraborate decahydrate (Fisher) in 2-propanol/water mixture (V/V:15/2). In the chip-scale EMLC

experiments, sodium perchlorate (Fisher) was added as an electrolyte to the mobile phase at a concentration of 0.10 M. Ethanolic solutions of 10 mM 1-octanethiol (Aldrich) or 11-mercapto-1-undecanol (Aldrich) were used to create hydrophobic or hydrophilic stationary phases by coating as a monolayer on the inner wall of the flow channel. Potassium ferrocyanide ($K_4Fe(CN)_6$, Fisher) and ferricyanide ($K_3Fe(CN)_6$, Fisher) were used as the redox couple to test the electrochemical characteristics of the EMLC chip, both were dissolved at a concentration of 50 μM in 0.10 M H_2SO_4 (Fisher) as a mixture.

Positive photoresist AZ5214 and its developer AZ 312 MIF were gifts from Clariant Corporation. The adhesion promoter 1,1,1,3,3,3-hexamethyl-disililazane (HMDS, 99.9%) was obtained from Aldrich. Buffered oxide etchant was prepared by mixing 28 mL hydrofluoric acid (50%, Fisher), with 113 g of ammonium fluoride (Fisher) in 170 mL of deionized water. Chromium etchant was made with 10 mL of hydrochloric acid (37%, Fisher) and 10 mL of glycerine (Aldrich). Gold etchant was a mixture of 4 g of potassium iodide (Fisher) with 1 g of iodine (Aldrich) in 40 mL of deionized water.

Lithographic mask generation. The lithographic mask used for optically transferring patterns onto photoresist was made on a photonegative. The mask generation process starts with designing the pattern on computer and then printing it onto bright-white paper using a conventional laser jet printer at 1200 dpi. The size of this pattern is usually four-times that of the desired size and with reserved black-and-white contrast. The drawing is then photographically reduced to the desired size, and reproduced on high contrast black-and-white film. Finally, the film is developed, and the photonegative is used as the mask in the lithography step of the chip fabrication process.

Chip design and fabrication. Wet chemical etching, fusion bonding, and physical vapor deposition techniques were used to fabricate microfluidic channels on the glass chip. Different chip configurations was designed to accomplish different types of separations.

(i) OTLC columns-on-chip. The OTLC columns using the native glass surface as stationary phase were fabricated via the micromachining processes shown in Figure 2. The 1x3 in glass slide (Fisher) was first cleaned in Pirahna solution (Caution: strong acid and oxidant) and then baked at 120°C for 2 h to dehydrate the surface. The slide was coated with adhesion promoter and photoresist via spin-coating at 4000 rpm. It was further baked at 90°C for 30 min. Next, the photonegative mask was placed on top of the photoresist, and the pattern was transferred from the mask to the photoresist with a UV exposure (275 W Hg lamp) of 365 nm for 90 sec. The photoresist was then developed in a solution of AZ 312 MIF.

Once the pattern was transferred, the photoresist was baked again at 120°C for 30 min. After that, thin layers of chromium (15 nm) and then gold (300 nm) were evaporated on the patterned-photoresist by resistive evaporation at a pressure $<1.3 \times 10^{-4}$ Pa. After a short sonication in acetone, the photoresist layer and the adherent metal layer were lifted off the glass slide, which transferred a reversed pattern of the photoresist onto the metal layer. The patterned metal layer now serves as the etching mask, which protects the underneath glass substrate from reacting with the buffered oxide etchant. The unprotected regions, therefore, were etched, forming a trench on the substrate. The etching rate was ~0.3 μm/min with the duration of the etch time determining the channel depth. After reaching the desired depth of the trench, the gold and chromium layers were stripped off using their corresponding etchant, and the slide was cleaned in Pirahna solution. The profile of the trenched flow channel was then characterized using a DEKTEK profilometer. Finally, a flat piece of a glass slide was bonded to the top of the patterned slide at 650°C. This fabrication process provides the flexibility to design flow channels of varied width, depth, and length.

The OTLC column with chemically modified stationary phase was constructed from flow channels defined by double-sided Scotch™ tape. First, thin layers of chromium and gold were deposited on a bare glass slide using the same resistive evaporation method. The gold slides were then modified by the self-assembly of either 1-octanethiol or 11-mercapto-1-undecanol by immersion in the 10 mM ethanolic solutions. The modified slides were next rinsed with ethanol and dried under a stream of nitrogen. Three separated sections of Scotch tape were then fixed on the slide, defining two flow channels on the gold surface along the 3 inch length of the slides. The top of the channels were sealed with a bare glass slide by adherence to the double-sided tape.

(ii) EMLC column-on-chip. The chips for the EMLC columns were fabricated by duplicating largely the second approach for making OTLC columns. Figure 3 shows a schematic representation of the EMLC chip. Here, the gold film on the bottom slide was electrically isolated into two separate electrodes by the gap in the middle of the film. Moreover, both counter and reference electrodes were formed on the bottom of the top slide in a comb-shaped geometry. The counter electrode comb was made by evaporating sequentially 15 nm of chromium and 150 nm of gold on the slides through a patterned metal mask. The comb for the pseudo reference electrode was evaporated on the same slide and consisted of a chromium layer (15 nm) and followed by a silver layer (150 nm). After assembly, the gold strips on the top of the bottom slide function as the working electrodes, the gold comb on the bottom of the top slide as the counter electrode, and the silver comb on the bottom of the top slide as the reference electrode. As shown in Figure 3, the two flow channels on the chip share the same counter and reference electrodes, but each has different working electrode with individual surface area of ~1 cm^2.

Cyclic voltammetry. The electrochemical viability of the EMLC chip was examined by cyclic voltammetry (CV), using an aqueous solution of 50 μM $K_3Fe(CN)_6/K_4Fe(CN)_6$

dissolved in 0.1 M H_2SO_4. The applied voltage was scanned from 0.0 to +0.5 V at a rate of 0.1 V/sec. A total of 25 scans were collected.

Separation test. In our preliminary separation assessments, a small drop of the sample solution was first placed at the entrance of the empty flow channel. The sample was then injected rapidly into the channel as a result of capillary action. After a small portion of the flow channel was filled with sample, the same entrance was immediately dipped in a reservoir filled with mobile phase. As such, the mobile phase continuously flows into the channel, stopping once the channel is completely filled. In the EMLC experiments, a potentiostat (Bioanalytical Systems CV-27) was used to apply voltages to the working electrode in one of the two columns on the same chip, while the working electrode in the other column was left at open circuit.

Detector setup. To monitor the separation inside the flow channel, the chip was placed under the Olympus BX50WI fluorescence microscope, equipped with 2x objective and a band pass filter cube for fluorescein and rhodamine excitation and emission. A Dage 330 color cameral was used to record the results at 30 frames/sec.

Results and Discussion

Fabrication result. The lithographic mask made on the high contrast black/white film showed improved feature definition. Figure 4 compares the pattern printed directly on an overhead transparency (Figure 4a) with the same pattern produced on a photonegative (Figure 4b). Clearly, the pattern on the transparency is poorly defined; the white region of the pattern has a lot of black dot while the black region has a lot of pin holes. Using this transparency as photo mask in the continuing fabrication step will result a blur pattern transferred onto the photoresist, and reduce the image resolution. On the other hand, the

image on the photonegative appeared with much improved resolution, and this technique was able to produce features 100 μm or even less.

The column layout on the OTLC chip and a cross-sectional profile at two adjacent sections of the microfabricated channel are shown in Figure 5. The column was designed in a serpentine pattern to increase the length of the channel and hence, the plate number. The profile shows that the channel is roughly 225-μm wide and 18-μm deep. The image also indicates that the depth of the channel is fairly uniform across the slide, but the glass surface at the bottom of the channel is much rougher after etching.

A photograph of the EMLC chip is shown in Figure 6. To facilitate visualization, both flow channels on the chip were filled with a concentrated rhodamine solution, which gives the channels a red-pink color. These channels are about 1-mm wide, as determined by the separation of the two stripes of double-sided tape, 50-μm deep, as determined by the thickness of the tape, and 70-mm long, which is the longest dimension of the glass slide. These dimensions are similar to those of the OTLC columns constructed using double-sided tape.

Capillarity induced liquid flow. We relied only on capillary action inside of the flow channel to induce liquid flow. No external pumps were used for fluidic delivery in the experiments. Because the Reynolds numbers (Re) of these microfluidic channels are very small (< 10), the fluidic movement inside the channels follows a Laminar flow pattern and can be described by Poiseuille's Equation.[36] Equation 1 is a modified form of Poiseuille's equation,[37] which describes the flow rate (v) fluid flow in channels with a rectangularly-shaped cross section.

$$v = \frac{1}{8\eta}\left(\frac{wh}{w+h}\right)^2 \frac{\Delta P}{L} \qquad (1)$$

where w and h are the width and the depth of the flow channel respectively, L is the length of the channel, η_m is the viscosity of the fluid, and ΔP is the pressure used for driving the flow of the liquid.

Capillarity, which results from the pressure difference between two sides of a liquid meniscus, can be described by Laplace's equation.[38] It is the fundamental reason that causes fluidic flow in these channels. Equation 2 is a modified version of Laplace's equation,[37] which relates ΔP for channels with a rectangularly-shaped cross section to the surface tension the liquid (γ).

$$\Delta P = \gamma \{ \frac{\cos\theta_{top} + \cos\theta_{bottom}}{h} + \frac{\cos\theta_{left} + \cos\theta_{right}}{w} \} \quad (2)$$

where θ is the contact angle where the liquid meets each side of the channel boundaries and the subscripts, *top, bottom, left,* and *right* denote the different sides of the channel.

Collectively, these equations show that the capillary flow rate is determined by the combined effect of the surface tension and viscosity of the flowing liquid (γ and η), the size and shape of the flow channel (w, h, and L), and the interaction between the liquid and channel walls (θ). In addition to these factors, we found that the roughness of the channel surface can have a dramatic effect on flow rate. For example, intermittent flow was sometimes observed inside the chemically-etched flow channel, which is likely due to the difference in surface smoothness at different locations within the channel. The average flow rate in these channels is about 5 mm/min or 20 nL/min.

OTLC separation. The choice to explore separations in an open tubular column comes from the pressure accessible for most of the existing micropumps. In packed columns, very high pressures (>100 bar) are usually required for fluid delivery. The

relatively low pressure that can be generated by micropumps, therefore, dictates the use of open tubular columns to induce fluid flow.

In open tubular columns, the efficiency of a separation depends on the partitioning of analytes between the walls of the column (i.e., the stationary phase) and the mobile phase. The plate height (*H*) of an open-tubular column was given by the form of Golay's equation as shown in Equation 3,[39, 40] and the plate number (*N*), which indicates the separation efficiency, can then be determined using Equation 4:

$$H = \frac{2D}{v} + \frac{(1+6k'+11k'^2)}{24(1+k')^2}\frac{r^2 v}{D} \qquad (3)$$

$$N = \frac{L}{H} \qquad (4)$$

where *D* is the analyte diffusion coefficient in the mobile phase, *r* is the radius of the flow channel, *k'* is the capacity factor of the analyte, *v* is the mobile phase flow rate, and *L* is the column length.

Clearly, in order to obtain higher separation efficiencies (i.e., larger values of *N*), long capillaries with smaller inner diameters are preferred. Indeed, long (1-10 m) narrow bore (i.d.<20 μm) capillaries are generally used as columns in conventional OTLC. However, glass capillaries of this size are often difficult to construct and very easy to clog. We relied on the micromachining techniques build shallow trenches directly on glass slides to address these problems. Instead of making channels with a circular cross section, we fabricated them with rectangular cross section shape. The intent was that having the short dimension of the rectangular cross section would facilitate separations, while the long dimension would render the channel less susceptible to particulate clogging.

(i) Using silanol groups on the glass surface as the stationary phase. Our first set of separation tests took advantage of the surface chemistry of glass. That is, the silanol

groups on the glass surface functioned as a normal phase stationary phase. Moreover, the chemical etching process roughens the inner capillary wall, which increases the surface area of the stationary phase and hence, the column capacity.

Figure 7 shows the separation of the fluorescent dye mixture upon injection into our chemically etched glass channel. The progression of the fluorescence images show that the green FL molecules move through the column near the speed of the solvent front with almost no retention, while the red RD molecules are more strongly retained by the silica stationary phase and move through the column at a much slower speed. The two dyes are completely separated from each other after traveling for 45 s in the column. The elution order of the two dyes is consistent with that observed using normal phase thin layer chromatography with silica gel as the stationary phase.[41] It is suspected that the separation is achieved due to the charge difference between the two types of dye molecules. That is, the FL carries two negative charge, while the RD carries a positive charge and a negative charge. Since most silanol groups on the glass surface are negatively charged under these conditions, the negatively charged stationary phase therefore repels the negatively charged FL, but strongly interact with the positive center of the RD, resulting stronger retention of the red RD band.

(ii) Using monolayer-coated gold thin films as a stationary phase. This set of experiment evaluates the separation efficiency of different types of stationary phases. To facilitate the creation of the stationary phase, we took advantage of self-assembled monolayer technology to modify the surface of gold thin films using different thiols.[42] Two thiol modifiers were used: 1-octanethiol to form a hydrophilic stationary phase and 11-mercapto-1-undecanol to form a hydrophilic stationary phase in the channel. The different end groups, which form the interface between the adlayer and the solution, determine the functionality of the stationary phase.

Both of the images in Figure 8 show the same separation performed using the two flow channels fabricated on a single glass slide. Figure 8a presents the results using the 11-mercapto-1-undecanol modified channels and Figure 8b presents the results using the1-octanethiol modified channels. There are two important observations when comparing the two results. First, the average capillary flow rate is approximately five times faster in the hydrophilic flow channels prepared by coating the underlying gold film with 11-mercapto-1-undecanol when compared with that in the hydrophobic channels prepared by coating with 1-octanethiol. Qualitatively, this difference agrees with theory. That is, according to Equations 1 and 2, a smaller contact angle between an aqueous solution and a hydrophilic surface leads to a larger ΔP and hence a larger v. Second, a more efficient separation is obtained in the hydrophobic channels (Figure 8b). We attribute the improved efficiency to the difference in both the flow rate and in the stationary phase. Note that these channels only have one of the two major surfaces modified by thiol, the other major surface of the channel is bare glass. Therefore, we suspect that it is the difference in flow rate that causes the difference in the separation. In addition, since the sample volume is also affected by the flow rate, the unresolved separation in Figure 8a may also reflect an injection of an excessive amount of sample causing the column to saturate. Nevertheless, Figure 8 suggests the end result is that a separation can be manipulated by using columns modified with different monolayers.

EMLC separation. The key behind EMLC is the manipulation of chemical separations by controlling the surface charge on the stationary phase. It therefore differs from the approaches commonly used in conventional LC, which rely on changes in the chemical composition of the mobile phase and/or stationary phase. By using a conductive stationary phase, such as porous graphitic carbon, the surface charge on the stationary phase can be controlled electrochemically after modifying a conventional LC column to

function as an electrochemical cell.[43] In such a cell, the conductive stationary phase also functions as the working electrode. When the potential applied to the working electrode equals the potential-of-zero-charge (pzc) of the stationary phase material, there is no excess charge present on the stationary phase. But when the potential is biased to a value positive or negative than the pzc, an excess of positive or negative charges can accumulate on the surface of the stationary phase, which then affects analyte retention.

The conventional-sized EMLC columns developed so far have demonstrated the effectiveness of the concept. However, the high solution resistance of the column limits the ability to switch the applied potential efficiently between different values. The work herein explores the opportunity to decrease the equilibration time by miniaturizing the system.

The electrochemical performance of the EMLC chip was examined prior to any separation tests. Figure 9 is a group of CVs obtained from 25 continuous scans. The reproducible position of the redox peaks demonstrates the effective stability of the quasi reference electrode. The reproducibility of the peak current, on the other hand, confirms the stability of the working electrode. More importantly, the peak separation in this experiment is only 123 mV, suggesting a rapid electrochemical response of this miniaturized cell, and therefore quick equilibration.

Figure 10 shows two sets of preliminary separations obtained with the EMLC chip. Two separations were carried out simultaneously on the same chip, with one at the open circuit potential and the other at a pre-selected applied potential. This dual-separation approach allows us to compensate, at least partially, for variations in injection time and flow rate by using the separation at open circuit as a reference. Both sets of results in Figure 10 were collected when the average flow rate within the two channels on the same chip was approximately the same; therefore, the difference in the separations can be attributed mainly to the effect of applying different potentials. Figure 10a, left, shows that, the red RD

is more strongly retained under negative applied potentials. On the other hand, it is less retained under more positive applied potentials, which causes the two dyes to be unresolved (Figure 10b, right).

There are two issues will be addressed in our ongoing effort. First, how the applied potential affects the separation is unclear. Besides the EMLC mechanism, we are also investigating the contribution of electrical field flow fractionation,[44] which may also affect the elution rate of charged analytes under applied potentials. Second, so far we are not able to reproduce, and therefore accurately assess, the effect of applied potential between experiments, a situation due to the complications in maintaining constant flow rates and injection volumes. Therefore, in order to quantitatively compare the separation results at different applied potentials, more reliable pumping and injection methods are needed. Nevertheless, these preliminary results demonstrate the possibility of manipulating separations in microfluidic channels by applying different potentials.

Conclusions

This paper has described the design and fabrication of chip-scale LC columns, as well as preliminary demonstrations of using these columns for model separations. This work, has produced several small-sized flow channels with a rectangular cross-section. Native glass and chemically modified gold thin films were used as stationary phases for the separation of two fluorescent dyes in miniaturized channels via an open-tubular liquid chromatography format. Electrochemically modulated liquid chromatography chip was constructed using a thin layer of gold as working electrode and stationary phase. The auxiliary and reference electrodes were also integrated inside the flow channel in a dual-comb arrangement. We showed that analyte retention was controlled by varying the applied potential to the chip.

Both the self-assembled monolayer stationary phases and the EMLC columns may have potential applications in the design and construction of combinatorial liquid chromatographic devices. For example, coating the inner walls of an array of microfluidic channels with a thin film of gold and flowing different thiol-containing modifiers into the different channels will form different monolayer-based stationary phases in a microchannel array. This microfluidic array can be used to analyze a sample mixture under different chromatographic conditions simultaneously. Combinatorial EMLC analyses can be performed by adding a set of electrodes to the microchannels and controlling the voltage applied to each electrode. In this device, separation can performed simultaneously on stationary phases of same chemical composition but with different surface charges. Both types of devices have the potential to increase the analysis throughput by performing combinatorial analyses in an array format.

Acknowledgments

J. N. gratefully acknowledges the support of the ACS Analytical Division Fellowship that is sponsored by the Eastman Chemical Company. We express our appreciation to Zhiyang Du, Mike Granger, and Janese O'Brein for their assistance in this work. This work was supported by NASA (Grant #NAGW4951) and by the Microanalytical Instrumentation Center of Iowa State University.

References

(1) Mastrangelo, C. H. *Adv. Sci. Technol.* **1999**, *26*, 465.

(2) Knapp, M. R.; Sundberg, S.; Kopf-Sill, A.; Nagle, R.; Gallagher, S.; Chow, C.; Wada, G.; Nikiforov, T.; Cohen, C.; Parce, J. W. *Am. Lab.* **1998**, *30*, 22.

(3) Manz, A.; Graber, N.; Widmer, H. M. *Sens. Actuators* **1990**, *B1*, 244.

(4) Schena, M.; Davis, R. W. In *PCR Appl.*, 1999, pp 445-456.

(5) Van Den Berg, A.; Lammerink, T. S. J. *Top. Curr. Chem.* **1998,** *194*, 21.

(6) Harrison, D. J.; van den Berg, A. *Proceedings of the Micro Total Analysis Systems '98*; Kluwer Academic: Banff, Canada, 1998.

(7) Howitz, S. *BioMethods* **1999,** *10*, 31-73.

(8) Kovacs, G. T. A.; Petersen, K.; Albin, M. *Anal. Chem.* **1996,** *38*, 407A.

(9) Mastrangelo, C. H.; Tang, W. C. In *Semiconductor Sensors*; Sze, S. M., Ed.; John Wiley and Sons: New York, 1994, pp 17.

(10) Stjernstrom, M.; Roeraade, J. *J. Micromech. Microeng.* **1998,** *8*, 33-38.

(11) Becker, H.; Gartner, C. *Electrophoresis* **2000,** *21*, 12-26.

(12) Chiang, Y.-M.; Bachman, M.; Chu, C. Y.; Li, G. *Proc. SPIE-Int. Soc. Opt. Eng.* **1999,** *3877*, 303-311.

(13) Martynova, L.; Locascio, L. E.; Gaitan, M.; Kramer, G. W.; Christensen, R. G.; MacCrehan, W. A. *Anal. Chem.* **1997,** *69*, 4783-4789.

(14) Martin, P. M.; Matson, D. W.; Bennett, W. D.; Lin, Y.; Hammerstrom, D. J. *J. Vac. Sci. Technol.* **1999,** *A17*, 2264-2269.

(15) Becker, H.; Heim, U.; Roetting, O. In *Proc. SPIE-Int. Soc. Opt. Eng.*, 1999; Vol. 3877, pp 74-79.

(16) Terry, S. C.; Jerman, J. H.; Angell, J. B. *IEEE Trans. Elec. Dev.* **1979,** *26*, 1880.

(17) Ruzicka, J.; Hansen, E. H. *Anal. Chim. Acta* **1984,** *161*, 1.

(18) Ruzicka, J.; Hansen, E. H. In *Anal. Chem.*, 2000; Vol. 72, pp 212A-217A.

(19) Deyl, Z.; Miksik, I.; Tagliaro, F. *Forensic Sci. Int.* **1998,** *92*, 89-124.

(20) Effenhauser, C. S.; Bruin, G. J. M.; Paulus, A. *Electrophoresis* **1997,** *18*, 2203-2213.

(21) Manz, A.; Verpoorte, E.; Effenhauser, C. S.; Burggraf, N.; Raymond, D. E.; Widmer, H. M. *Fresenius' J. Anal. Chem.* **1994,** *348*, 567-71.

(22) Regnier, F. E.; He, B.; Lin, S.; Busse, J. *Trends Biotechnol.* **1999,** *17*, 101-106.

(23) Kambara, H. *Curr. Top. Anal. Chem.* **1998,** *1*, 21-36.

(24) Paulus, A. *Am. Lab.* **1998,** *30*, 59-62.

(25) Chiem, N. H.; Harrison, D. J. *Clin. Chem.* **1998,** *44*, 591-598.

(26) Hadd, A. G.; Raymond, D. E.; Halliwell, J. W.; Jacobson, S. C.; Ramsey, J. M. *Anal. Chem.* **1997,** *69*, 3407-3412.

(27) Hadd, A. G.; Jacobson, S. C.; Ramsey, J. M. *Anal. Chem.* **1999,** *71*, 5206-5212.

(28) Manz, A.; Miyahara, Y.; Miura, J.; Watanabe, Y.; Miyagi, H.; Sato, K. *Sens. Actuators* **1990,** *B1*, 249.

(29) McEnery, M.; Tan, A.; Alderman, J.; Patterson, J.; O'Mathuna, S. C.; Glennon, J. D. *Analyst* **2000,** *125*, 25.

(30) Ryu, D. D. Y.; Nam, D.-H. *Biotechnol. Prog.* **2000,** *16*, 2.

(31) Ho, C.-M.; Tai, Y.-C. *J. Fluids Eng.* **1996,** *118*, 437.

(32) Shoji, S.; Esashi, M. *J. Micromech. Microeng.* **1994,** *4*, 157.

(33) Elwenspoek, M.; Lammerink, T. S. J.; Miyake, R.; Fluitman, J. H. J. In *J. Micromech. Microeng.*, 1994; Vol. 4, pp 227-45.

(34) Elwenspoek, M.; Lammerink, T. S. J.; Miyake, R.; Fluitman, J. H. J. In *Analusis*, 1994; Vol. 22, pp M9-M12.

(35) Porter, M. D.; Zhong, C.-J.; Ni, J.; Coldiron, S. J.; Tang, W. C. *SAE Technical Paper Series*, Lake Tahoe, Nevada, July 14-17, 1997 1997; 972420.

(36) Giancoli, D. C. In *Physics: Principles with Applications*; Prentice-Hall, Inc: Englewood Cliffs, NY, 1980, pp 147.

(37) Delamarche, E.; Bernard, A.; Schmid, H.; Bietsch, A.; Michel, B.; Biebuyck, H. *J. Am. Chem. Soc.* **1998,** *120*, 500.

(38) Adamson, A. W. *Physical Chemistry of Surfaces*; John Wiley and Sons: New York, 1990.

(39) Golay, M. J. E. In *Gas Chromatography*; Desty, D. H., Ed.: Butterworths, London, 1958, pp 36.

(40) Jorgenson, J. W.; Guthrie, E. J. *J. Chromatogr.* **1983,** *255*, 335.

(41) Reynolds, R. C.; O'Dell, C. A. *J. Chem. Edu.* **1992,** *69*, 989.

(42) Zhong, C.-J.; Porter, M. D. *Anal. Chem.* **1995,** *67*, 709 A.

(43) Ting, E.-Y.; Porter, M. D. *Anal. Chem.* **1998,** *70*, 94.

(44) Kesner, L. F.; Caldwell, K. D.; Myers, M. N.; Giddings, J. C. *Anal. Chem.* **1976,** *48*, 1834.

Figure Captions

Figure 1. Schematic representation of a microfluidic device.

Figure 2. Open tubular glass channel fabrication process.

Figure 3. Schematic representation of the three structured layers of an EMLC fluidic chip.

Figure 4. Comparison of (a) pattern printed directly from a 1200 dpi laser printer onto a transparency film, and (b) the pattern of same feature size obtained on the photonegative.

Figure 5. Microfluidic channels fabricated from wet chemical etching process. (a) flow channel layout, and (b) cross section depth profiles obtained at two adjacent section of the channel.

Figure 6. The photograph of a completed EMLC chip. The two red-pink lines running from left to right on the chip are the two flow channels.

Figure 7. Separation of RD and FL in the OTLC channel fabricated from wet chemical etching process. The native silanol groups on the glass surface served as stationary phase for normal phase separation. Average flow rate is ~5 mm/min.

Figure 8. Manipulation of flow rate and separation by modifying the gold surface with different self-assembled monolayers. (a) separation of RD and FL in hydrophilic channels modified with 11-mercapto-1-undecanol, at an average flow rate of ~300 mm/min, and (b) separation of RD and FL in hydrophobic channels modified with octanethiol, at an average flow rate of ~50 mm/min.

Figure 9. Cyclic voltammograms ferrocyanide/ferricyanide redox couple collected from 25 continuous scans at a rate of 0.1 V/s. See text for details.

Figure 10. Manipulation of separation by applying different potentials on the stationary phase. (a) comparing the separation of RD and FL at the negatively-biased bare

gold channels with that under open circuit condition, at an average flow rate of ~75 mm/min and (b) comparing the separation of RD and FL in positively-biased bare gold channels with that under open circuit condition, at an average flow rate of 88 mm/min. The open circuit potential of each of these test channels ranged between –150 mV to –200 mV.

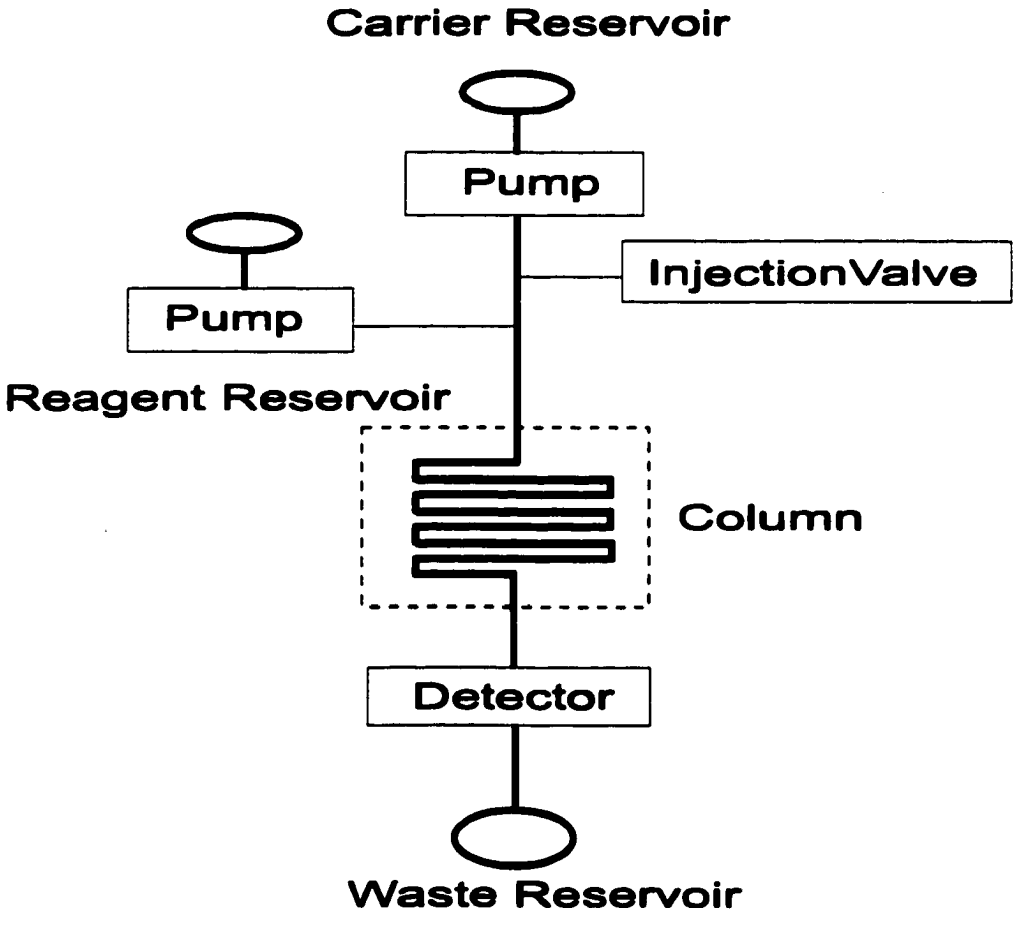
Carrier Reservoir
Pump
InjectionValve
Pump
Reagent Reservoir
Column
Detector
Waste Reservoir

Figure 1.

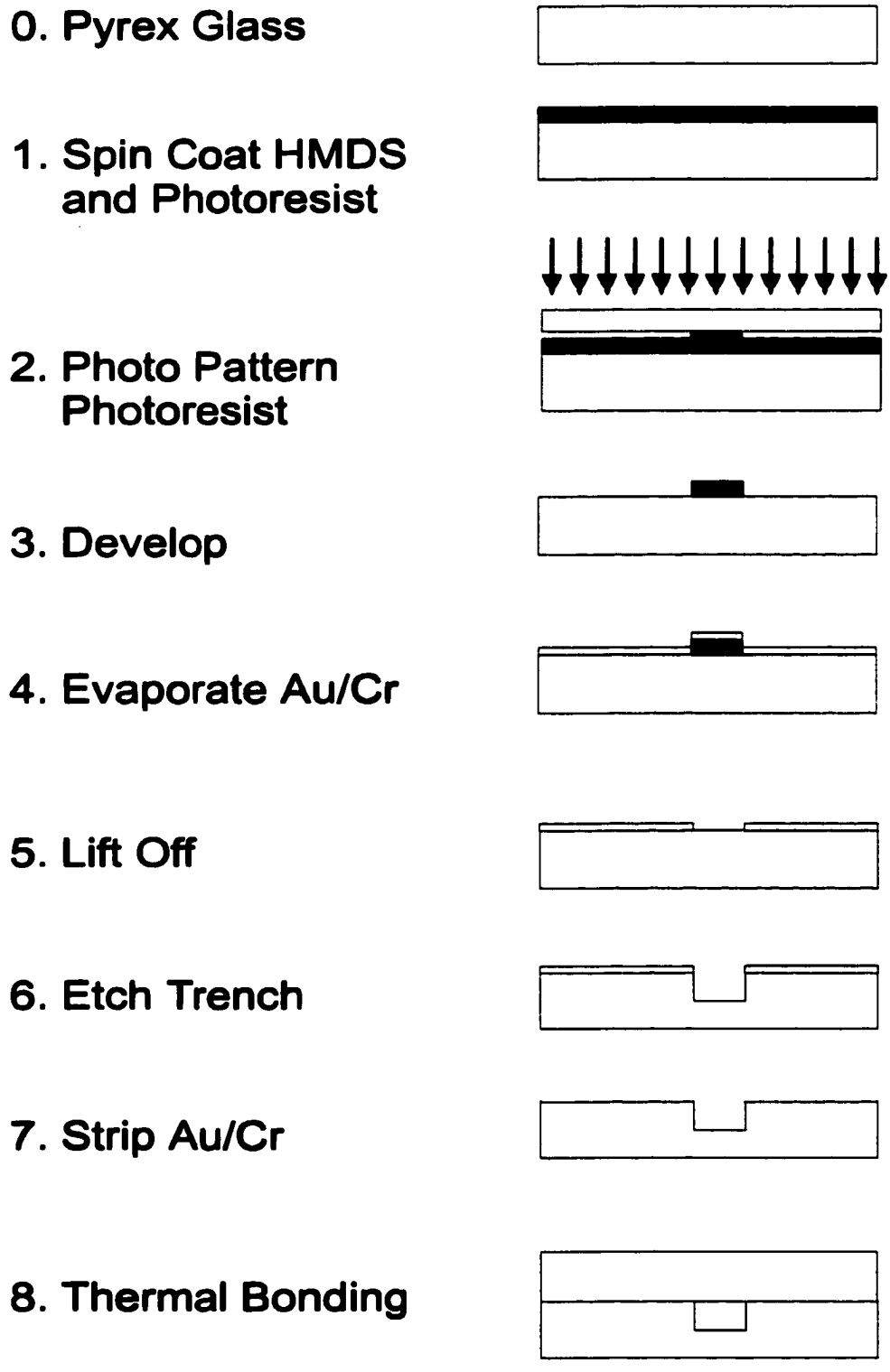
0. Pyrex Glass
1. Spin Coat HMDS and Photoresist
2. Photo Pattern Photoresist
3. Develop
4. Evaporate Au/Cr
5. Lift Off
6. Etch Trench
7. Strip Au/Cr
8. Thermal Bonding

Figure 2.

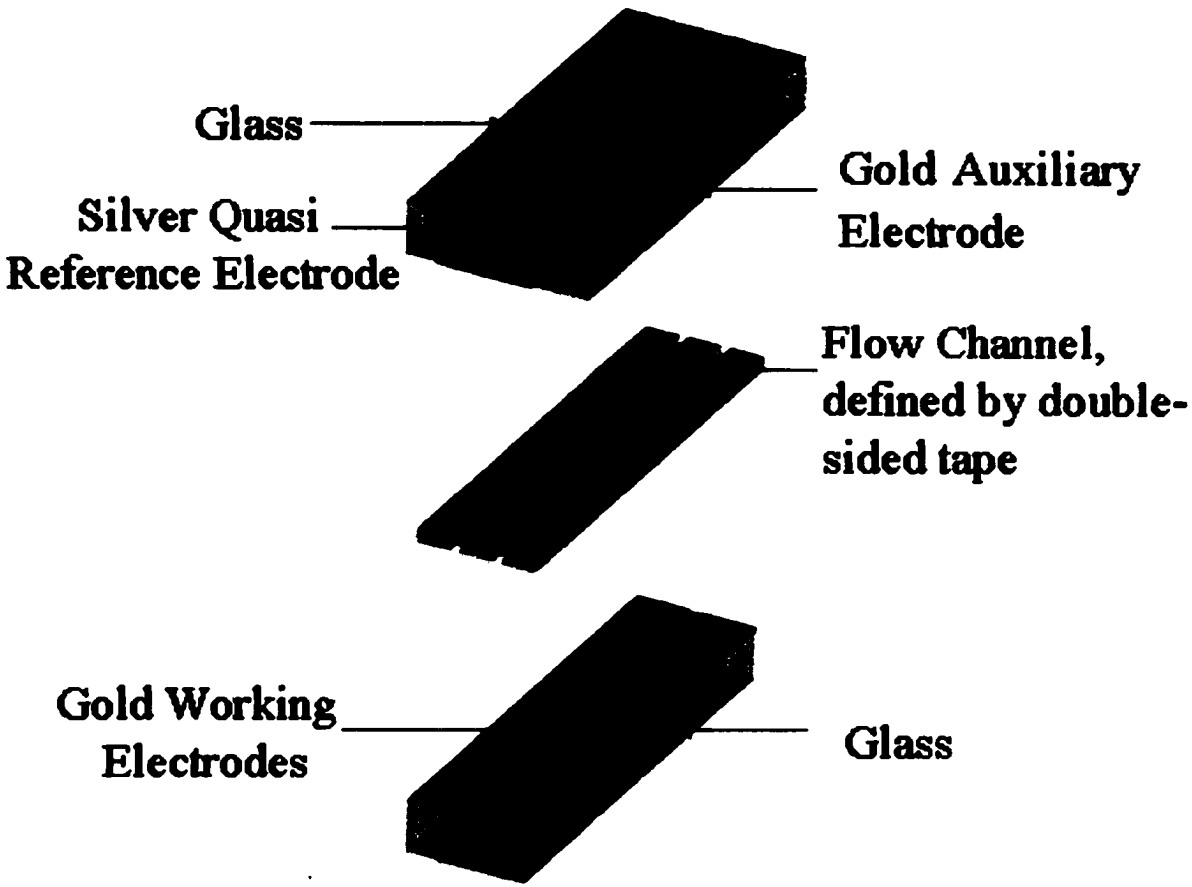
Glass
Silver Quasi Reference Electrode
Gold Auxiliary Electrode
Flow Channel, defined by double-sided tape
Gold Working Electrodes
Glass

Figure 3.

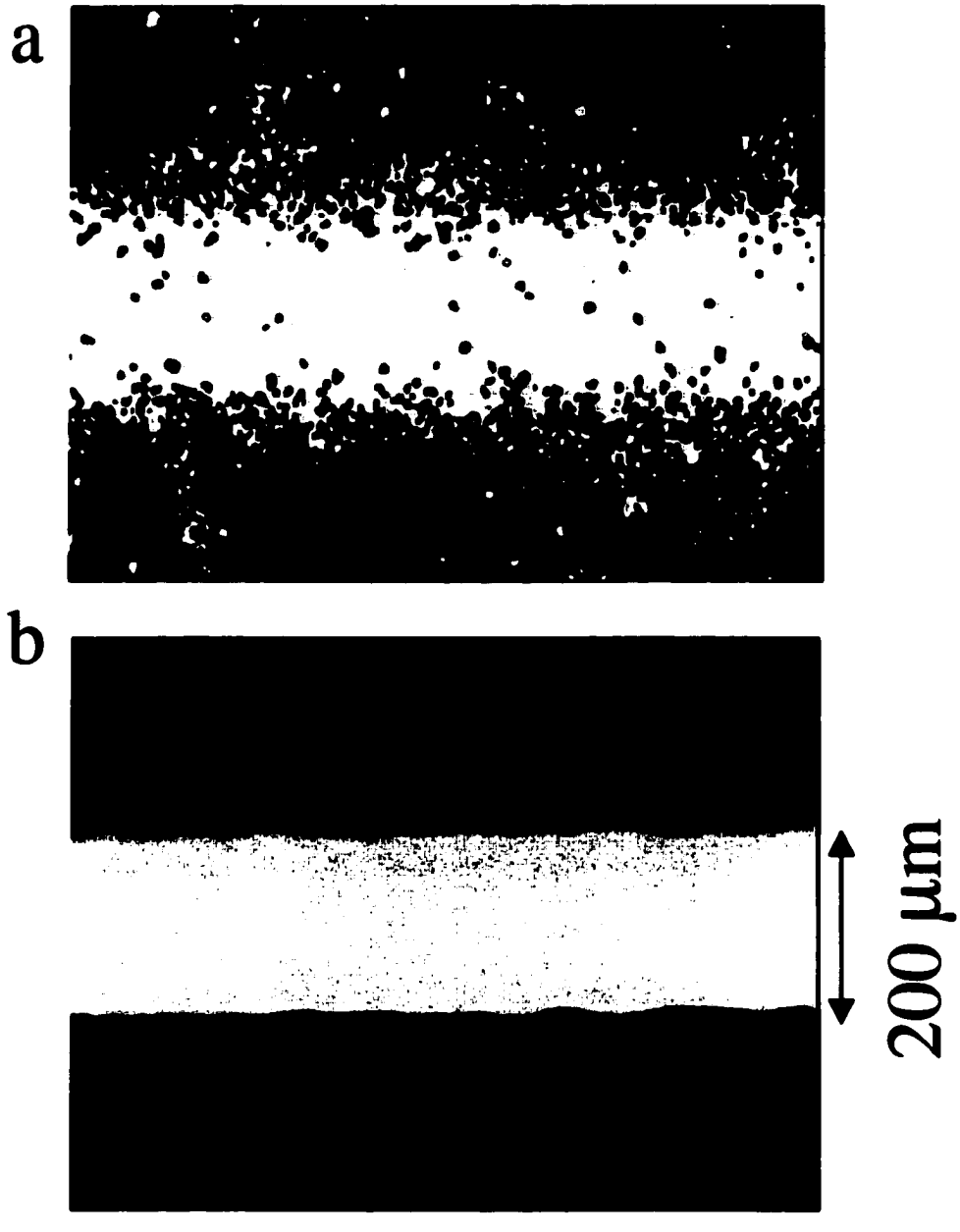

Figure 4.

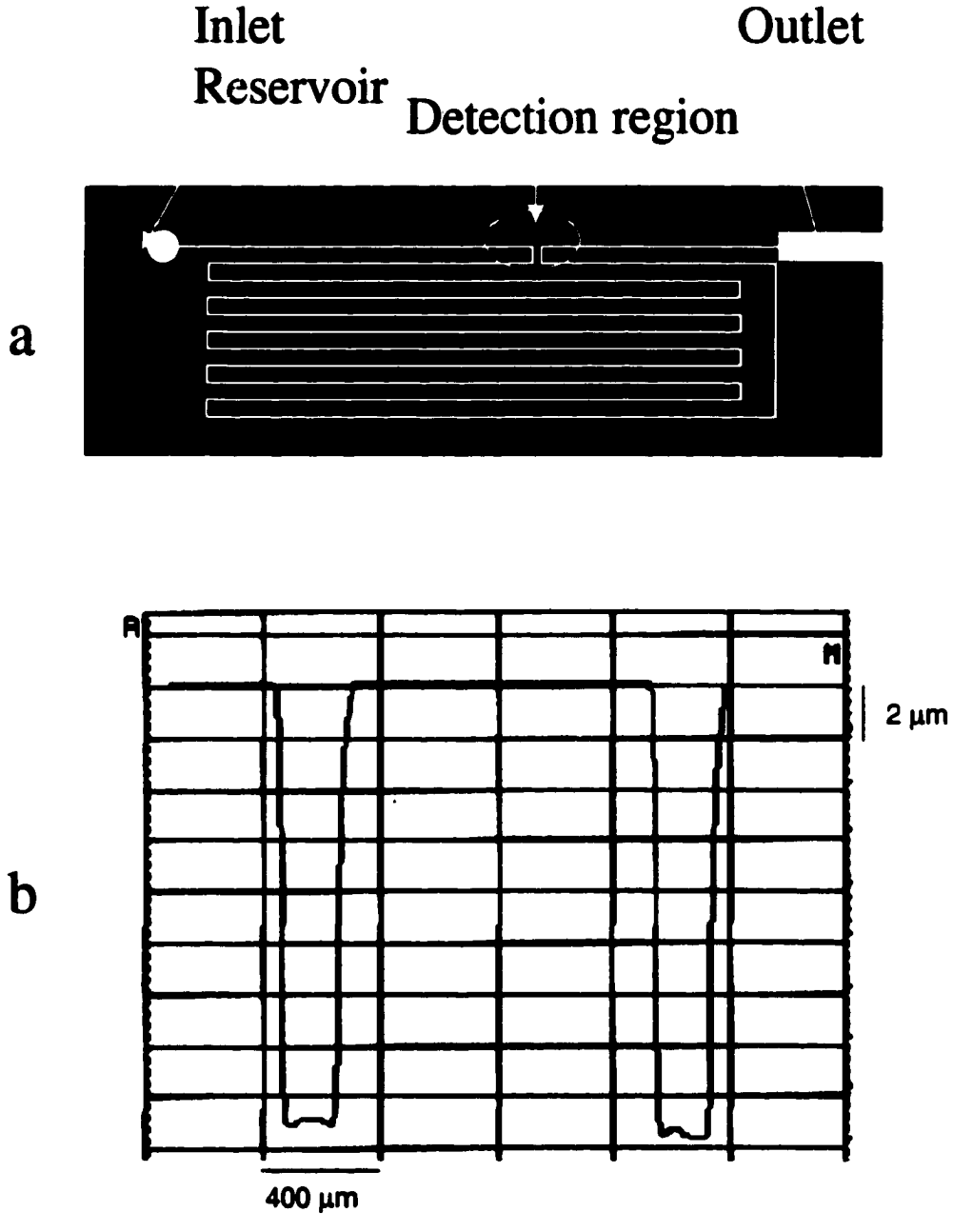

Figure 5.

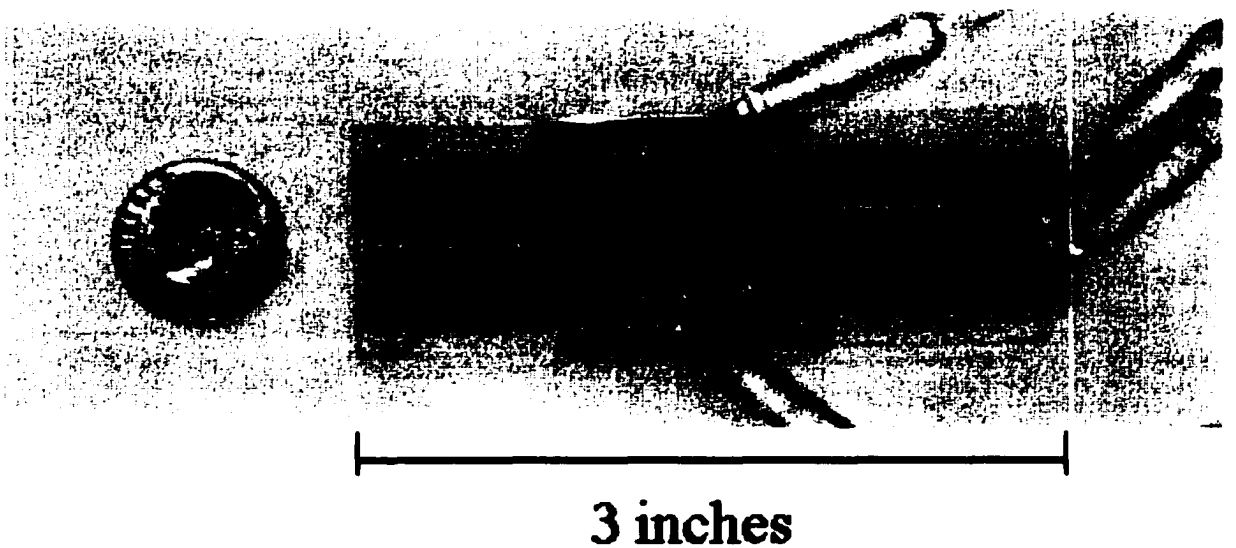

Figure 6.

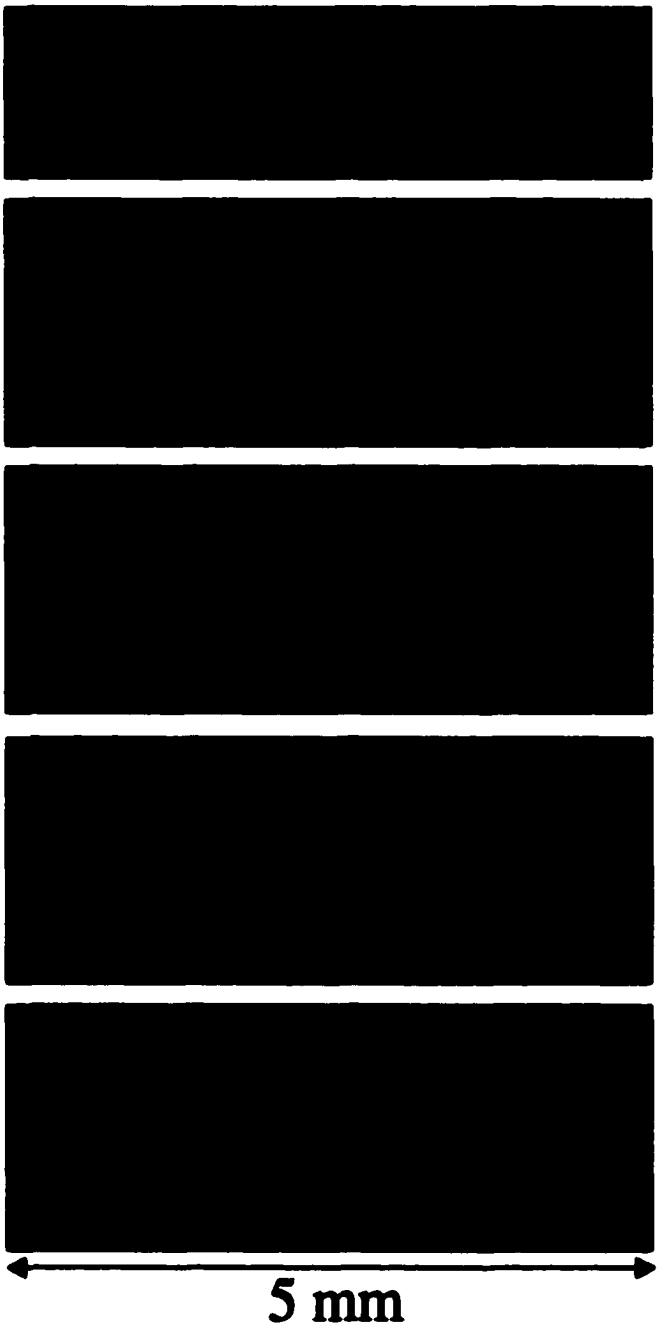

Figure 7.

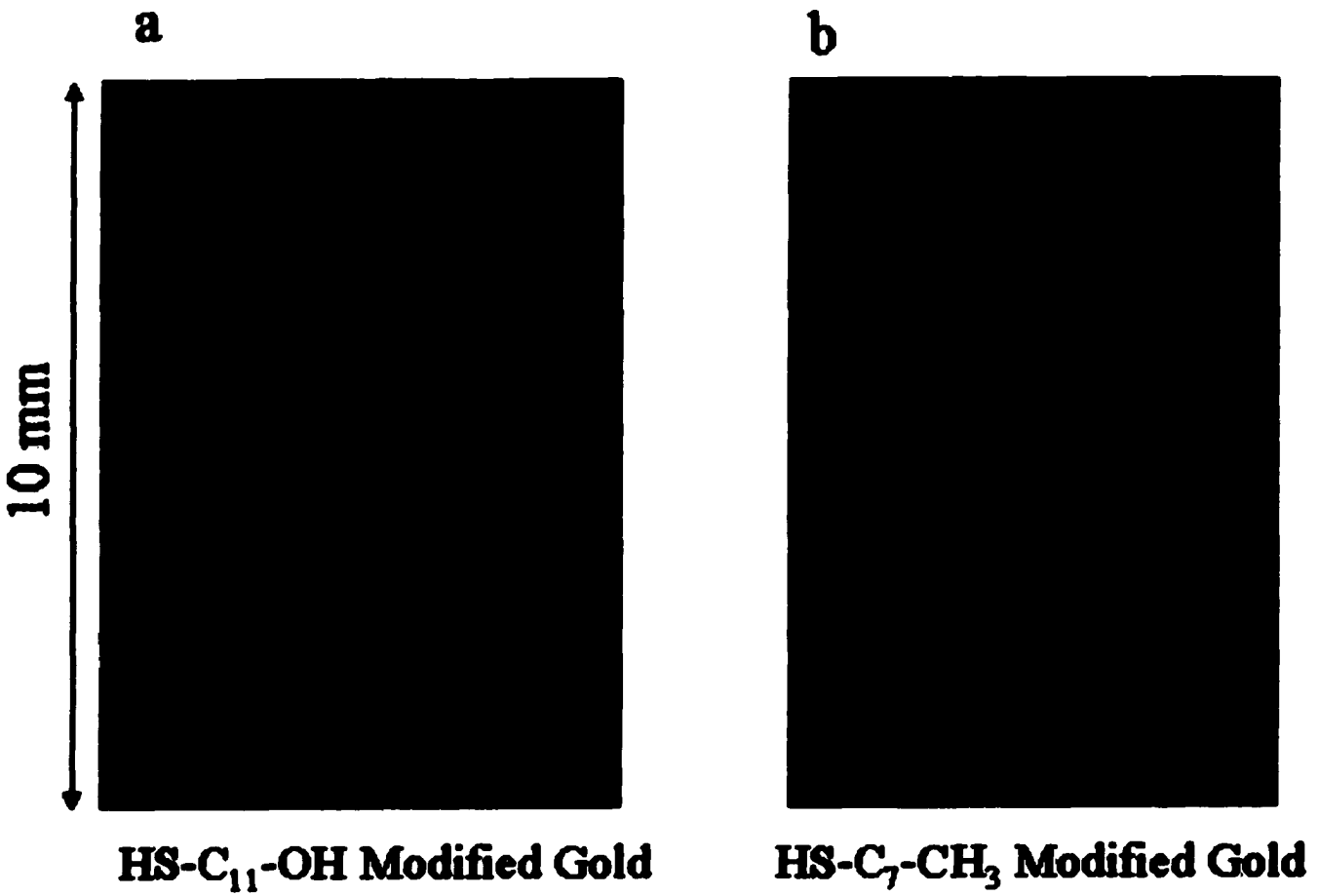

Figure 8.

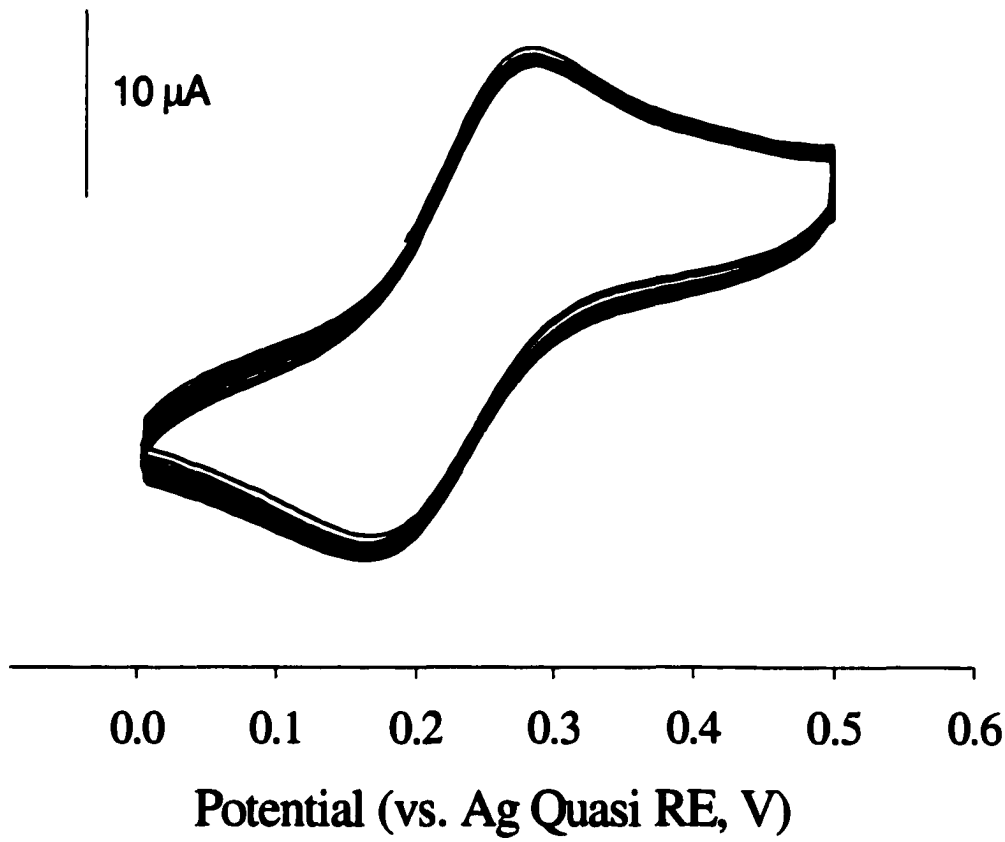

Figure 9.

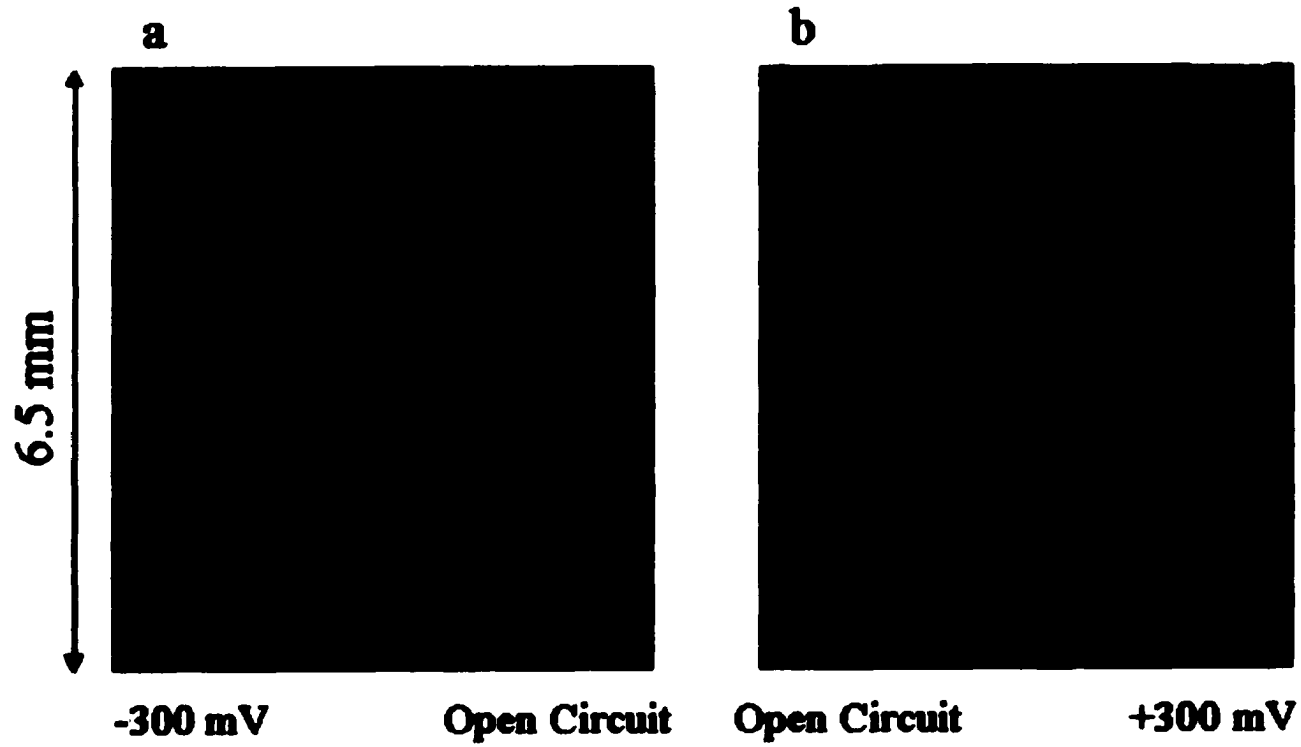

Figure 10.

CHAPTER 4. IMMUNOASSAY READOUT METHOD USING EXTRINSIC RAMAN LABELS ADSORBED ON IMMUNOGOLD COLLOIDS

A paper published in *Analytical Chemistry*[1]

Jing Ni,[2] Robert J. Lipert,[2] G. Brent Dawson,[2] and Marc D. Porter[2,3]

Abstract

An immunoassay readout method based on surface enhanced Raman scattering (SERS) is described. The method exploits the SERS-derived signal from reporter molecules that are co-immobilized with biospecific species on gold colloids. This concept is demonstrated in a dual-analyte sandwich assay, in which two different antibodies covalently bound to a solid substrate specifically capture two different antigens from an aqueous sample. The captured antigens in turn bind selectively to their corresponding detection antibodies. The detection antibodies are conjugated with gold colloids that are labeled with different Raman reporter molecules, which serve as extrinsic labels for each type of antibody. The presence of a specific antigen is established by the characteristic SERS spectrum of the reporter molecule. A near-infrared diode laser was used to excite efficiently the SERS signal while minimizing fluorescence interference. We show that by using different labels with little spectral overlap, two different antigenic species can be detected simultaneously. The potential of this concept to function as a readout strategy for multiple analytes is briefly discussed.

---

[1] Reprinted with permission from *Anal. Chem.* **1999**, 71, 4903-4908.

[2] Microanalytical Instrumentation Center, Ames Laboratory-USDOE, and Department of Chemistry, Iowa State University, Ames, IA 50011

[3] Corresponding author

Introduction

Many immunoassays (e.g., the screening of cancer markers, such as alphafetoprotein and carcinoembryonic antigen[1]) require the concomitant determination of several analytes. There are two general approaches to address this need. One approach immobilizes different antibodies on a solid support at spatially separated addresses. Multiple antigens can then be detected using the same label, with identification based on address location.[2, 3] Alternatively, different labels can be used to detect different analytes simultaneously in the same spatial area.[4-13] In this case, the labeled analyte is first separated from the sample and then analyzed by a variety of different approaches,[14] including scintillation counting,[5] fluorescence,[6, 7] absorption,[8] electrochemistry,[9] chemiluminescence,[11] Rayleigh scattering,[12] and Raman scattering.[13] Of these techniques, fluorescence spectroscopy has been one of the most widely used readout methods, primarily because of its high sensitivity.

Conventional Raman spectroscopy usually lacks sufficient sensitivity for use as a readout method for immunoassays. Surface enhanced Raman spectroscopy, on the other hand, has demonstrated its ability to detect picomole to femtomole amounts of materials adsorbed on several types of roughened metal surfaces.[15] Among the metallic substrates used for surface enhanced Raman scattering (SERS) are metal nanoparticles (e.g., gold and silver colloids). Impressively, recent reports have shown that certain nanoparticle substrates can yield SERS intensities comparable to or even exceeding those from fluorescence.[16, 17] Furthermore, metallic nanoparticles have been used in several forms of bioassays, with detection based on colorimetry,[18] photothermal deflection,[19-21] surface plasmon resonance[22], and scanning electron microscopy [23].

Based on these precedents, it is intriguing to speculate about the potential utility of SERS in the immunoassay arena. There are several characteristics of SERS that suggest it may be of value as a readout method.[15, 24, 25] Raman bands are generally 10-100 times narrower than most fluorescence bands, minimizing the potential overlap of different labels in a given spectral region. Second, the optimum excitation wavelength for SERS is not strongly dependent on the adsorbed analyte, allowing the use of a single excitation source for multiple species. Third, Raman scattering is not sensitive to humidity or affected by oxygen and other quenchers, facilitating applications in a variety of environments. Finally, the SERS signal is less subject to photobleaching, potentially enabling one to signal average for extended time periods to lower the limit of detection.

Surprisingly, there have been only a few reports on the application of SERS for detection in immunoassays.[13, 26] Both approaches used a sandwich-type assay, which coupled surface and resonance enhancements. Rohr et al. used labeled detection antibodies and roughened silver films coated with a capture antibody,[13] and Dou et al. exploited the adsorption on silver colloids of an enzymatically amplified product.[26] This paper describes an alternative approach using SERS together with labeled immunogold colloids as a readout method, which requires neither resonance enhancement nor enzymatic amplification. Scheme 1 depicts the three-step assay. It involves the immobilization of capture antibodies on a gold surface, the use of the immobilized antibodies to capture antigens from solution, and indirect Raman detection via gold nanoparticles labeled with both antibodies and intrinsically strong Raman scatterers (i.e., Raman reporter molecules). A different Raman scatterer is used to label extrinsically each of the different immunogold colloids, with the presence of different antigens detected by the characteristic Raman bands of the labels. This approach also takes advantage of long wavelength excitation operative for gold colloids,[16, 27, 28] which minimizes native fluorescence and

photobleaching complications. The potential of this concept to become a sensitive, high throughput readout method for immunoassays is discussed.

Experimental

Reagents. Suspensions of unconjugated colloidal gold (30 nm, 2×10^{11} particles/mL) and anti-rat IgG conjugated colloidal gold (30 nm, 8×10^{11} particles/mL) were purchased from Ted Pella, Inc. Polyclonal rat, rabbit, goat, goat anti-rat, and goat anti-rabbit IgG were acquired from Pierce. Thioctic acid (98%), 1-ethyl-3-[3-(dimethylamino)propyl] carbodiimide (EDC), Tween 80, 2-ethanolamine, thiophenol (TP), 2-naphthalenethiol (NT) and 4-mercaptobenzoic acid (MBA) were obtained from Aldrich. Sodium tetraborate decahydrate, potassium phosphate, tris(hydroxymethyl)aminomethane (Tris), sodium chloride, and magnesium chloride were purchased from Fisher. All reagents were used as received.

Preparation of Raman reporter-labeled immunogold colloids. Raman reporter-labeled immunogold colloids were prepared in a two-step process. In the first step, the uncoated gold colloids were labeled with Raman reporters through the spontaneous adsorption of thiol molecules on gold.[29-32] MBA, NT, and TP were chosen as reporters because of the large enhancements described in earlier SERS characterizations of these and related molecules and/or the minimal overlap of their spectral features.[33, 34] Typically, 2.5 μL of an ethanolic thiol solution (1 mM MBA or TP, 0.5 mM NT) were added to 1 mL of an unconjugated colloidal gold suspension and allowed to react for 12 h. The amount of thiol, based on an estimation of the colloidal surface area, was chosen to coat only a portion of the colloidal surface; fully coated colloids were found to be less stable as dispersions and had a tendency to aggregate during centrifugation. This process also left exposed portions of the colloidal surface available for IgG protein immobilization. The reporter-labeled

colloids were then separated from solution by centrifugation at 14,000 g for 4 min. The clear supernatant was discarded, and the loosely packed red gold sediment was resuspended in 1 mL of borate buffer (2 mM, pH = 9).

The second step of the preparation involved the immobilization of the different IgG proteins on the reporter-labeled colloids. While gently agitating, 23 μg of antibody (goat anti-rat or goat anti-rabbit IgG) were added to the 1 mL suspension of the reporter-labeled gold colloids. This amount of antibody is ~50% more than the minimum amount (determined according to the observed dispersion stability in flocculation tests[35]) for coating the unmodified portion of the colloidal gold surface. The mixture was incubated at room temperature for 60 min, during which the IgG proteins adsorbed onto the colloids through a combination of ionic and hydrophobic interactions.[35] Upon centrifugation at 14,000 g for 5 min, two phases were usually obtained: a clear supernatant of unbound antibody and a dark red, loosely packed sediment of the reporter-labeled immunogold. Occasionally, a dense, black sediment of metallic gold was also found; this sediment was attributed to aggregation of colloidal gold that was not effectively stabilized by the antibody coating.[35] Next, the loose sediment of reporter-labeled immunogold was rinsed by resuspending in 2 mM borate buffer and collected after a second centrifugation at 14,000 g for 5 min. Finally, the complex was resuspended in 0.5 mL of 10 mM Tris-buffered saline (Tris/HCl, NaCl 10 mM, $MgCl_2$ 1.5 mM, pH 7.6), with 0.1% Tween 80 added for minimizing nonspecific adsorption during the assays. The concentration of the reporter-labeled immunogold suspension was ~3×10^{11} particles/mL based on a calibration curve constructed using the colloid absorbance at 525 nm.[36] These suspensions were usually stable for 2-3 days when stored at 4 °C.

Preparation of capture antibody substrates. Glass microscope slides were first soaked in a dilute surfactant solution (Micro, Cole-Parmer) for 12 h, rinsed with deionized water and ethanol, and dried in a stream of nitrogen. The slides were then coated with 15

nm of chromium, followed by 300 nm of gold by resistive evaporation at a pressure of <1.3 X 10^{-4} Pa. The gold substrates were next cut into 1 cm x 1 cm sections and immersed in a 1 mM ethanolic solution of thioctic acid for ~12 h to form a carboxylic acid-terminated monolayer.[37]

The immobilization of the IgG proteins was accomplished by first immersing the monolayer modified substrates into 1% (w/w) EDC in anhydrous acetonitrile for 5 h. This step activates the free carboxyl groups of thioctic acid by forming an *O*-acylurea intermediate with EDC.[38] The activated surface was then modified by pipetting 100 μL of a mixture of goat anti-rat and goat anti-rabbit IgG (50 μg/mL of each in 0.1 M borate buffer, pH = 9) onto the 1 cm^2 substrate. The reaction was allowed to progress at 4 °C for 12 h. In the early stages of this investigation, the modified substrates were next soaked in 0.1 M borate buffer (pH 8.75) that contained 5% (v/v) 2-ethanolamine to block residual *O*-acylurea intermediates.[38] We found, however, that this step was not necessary since unreacted intermediates were effectively hydrolyzed during the IgG immobilization step. This finding was confirmed by infrared reflection-absorption spectroscopy, which was also used to verify the success of each modification step, including formation of the carboxylic acid-terminated monolayer, activation of the free carboxyl groups with EDC, and antibody immobilization. Finally, the antibody-coated substrates were rinsed with deionized water, and quickly dried under a stream of argon. All assays were conducted immediately after substrate drying. The activity of surfaces prepared in this way has been confirmed previously in our group by scanning probe microscopy and fluorescence imaging.[39]

Immunoassay protocol. The immunoassays were conducted by following the typical procedure for a sandwich-type assay.[14] Goat IgG, rat IgG, rabbit IgG, and a 1:1 mixture of rat and rabbit IgG were used as test antigens. In each case, 100 μL of IgG

solution (1 μg/mL total antibody) in 50 mM PBS buffer (KH_2PO_4/K_2HPO_4, 150 mM NaCl, pH = 7.6) was pipetted onto the capture antibody-coated substrate and allowed to react for 1 h at room temperature. After rinsing with copious amounts of water, the sample was exposed to 100 μL of reporter-labeled immunogold solution for 3 h. All samples were then rinsed with deionized water and dried under argon before SERS characterization.

SERS measurements. SERS was excited using a diode laser (Hitachi HL7851G, Thorlabs). The laser was mounted in a commercial housing (ILX Lightwave Model LDM-4412) that was equipped with a collimating lens and thermoelectric cooler. The operating temperature was held at 20 °C by an ILX Lightwave temperature controller (Model LDT-5910). An ILX current source (Model LDX-3207B) maintained the operating current at 120 mA. These conditions produced 50 mW of output power at the sample with a wavelength of 785.13 nm. A pair of Pellin-Broca prisms and an iris were used to remove background laser diode emission. The laser output was focused onto the sample with a 50 mm focal length cylindrical lens at an angle of ~60° with respect to the surface normal. The illuminated area on the sample was roughly 3 mm by 0.25 mm. The Raman scattered light was collected at *f*/2 and imaged onto the entrance slit (200 μm slit width) of a 300 mm *f*/4 spectrograph (SpectraPro 300i, Acton Research Corp.). A 1200 grooves/mm grating that was blazed for 750 nm produced a nominal dispersion of 2.7 nm/mm. Rayleigh scattering was blocked using a holographic notch filter (HSPF-785.0, Kaiser Optical Systems). The spectrograph was equipped with a thinned, back-illuminated, liquid nitrogen-cooled CCD (LN/CCD-1100PB, Princeton Instruments). The positions of the reporter molecule Raman bands were determined by calibration using the known band positions of solid naphthalene.

Results and Discussion

SERS of reporter-labeled immunogold. Three types of reporter-labeled immunogold colloids were prepared: (a) MBA/anti-rat IgG, (b) NT/anti-rat IgG, (c) TP/anti-rabbit IgG. Each type of colloid was then immobilized onto its corresponding antigenic substrate by sandwich formation (e.g., the sequential exposure of the gold substrate coated with anti-rat IgG to a solution of rat IgG and then to a solution of MBA/anti-rat IgG immunogold) for SERS characterization. A sample using the commercially prepared anti-rat IgG labeled gold colloids was also prepared for comparison.

One set of results for these characterizations (10 s integration time) is shown in Figure 1 between 980 cm^{-1} and 1610 cm^{-1}. Several strong aromatic vibrational bands are present within this spectral region that are diagnostic of the three different labels. Indeed, all of the bands in each spectrum can be assigned to either C-H or ring in-plane bending, ring in-plane bending coupled with C-S stretching, or ring C=C stretching of the labels.[40] For example, two distinct bands, one at 1075 cm^{-1} and the other at 1587 cm^{-1}, are observed in the spectrum for the sample containing the immobilized MBA/anti-rat IgG particles (Figure 1a). Similarly, the samples with the NT-labeled particles exhibit strong bands at 1067 cm^{-1} and 1377 cm^{-1} (Figure 1b), and the TP-labeled particles have bands at 999 cm^{-1}, 1022 cm^{-1}, 1071 cm^{-1}, and 1568 cm^{-1} (Figure 1c). Experiments also demonstrated that there was no detectable change in SERS intensity for samples continuously illuminated for 60 min at 50 mW.

On the other hand, there are no detectable features evident in the same spectral region for the sandwich composed of colloids coated only with anti-rat IgG (i.e., gold colloids devoid of a reporter molecule, Figure 1d). This observation is consistent with earlier investigations on the use of SERS in characterizing protein adsorption on gold.[41, 42] It likely arises from a combination of the lower surface enhancement factor for gold relative to silver

and the rapid decay of the strongly enhanced electromagnetic field with distance from the metal surface. The absence of detectable Raman scattering from the proteins adsorbed on colloidal gold demonstrates the necessity of extrinsic labeling.

There are several important observations from the results in Figure 1. First, strong Raman bands are detectable for all three of the labels. These signal strengths are consistent with enhancements for adsorbates bound to gold colloids,[15, 27, 43] and varied in magnitude by 5% across an individual sample surface and by 12% between two different sets of samples. Second, the MBA-labeled sample gives a stronger Raman signal than the NT-labeled sample, followed by the TP-labeled sample. While this trend may be a result of the intrinsic differences in the scattering properties of the labels, it may also reflect a difference in the relative coverage and/or orientation of the labels adsorbed on the colloid, assuming the number of immobilized colloids is the same on each substrate. Third, the location of the vibrational bands identifies the labels most effective for a multianalyte immunoassay, which requires minimal spectral overlap between labels. In terms of minimal overlap, the most useful combination is the 1377 cm^{-1} band for the NT-labeled gold and the 995 cm^{-1} band for the TP-labeled gold. Together, these results begin to establish the viability of our proposed concept.

Specificity. The experiments described in this section demonstrate the feasibility of combining SERS and reporter-labeled immunogold to detect the presence of specific antigenic species in aqueous samples. These experiments used gold colloids that were labeled with MBA as the Raman reporter and with goat anti-rat IgG for immunorecognition. Polyclonal goat anti-rat IgG and goat anti-rabbit IgG were used as capture antibodies and were co-immobilized onto three separate gold substrates as described earlier. One of the substrates was then exposed to a solution of rat IgG, another to a rabbit IgG solution, and the third to a goat IgG solution. After incubation for 1 h, the samples were developed in the

MBA-labeled immunogold suspension for 3 h. The results of the SERS characterization (1 s integration time) are presented in Figures 2a-c for the samples exposed to rat IgG, rabbit IgG, and goat IgG, respectively.

The rat IgG sample shows very strong SERS bands at 1075 cm^{-1} and 1587 cm^{-1}. These bands, by inspection of Figure 1a, are diagnostic of the MBA reporter that is co-immobilized with anti-rat IgG on the colloids. This result is consistent with the binding specificity in a sandwich-type assay for rat IgG.

The specificity of our assay concept was also tested by the experiments using rabbit IgG and goat IgG samples (Figures 2b,c). Rabbit IgG can be captured by the substrate, but should not strongly bind to the goat anti-rat IgG immobilized on the gold colloids. In contrast, goat IgG should not be captured by the substrate nor specifically bind with goat anti-rat IgG colloids. The bands evident in these latter two spectra for either goat IgG or goat anti-rat IgG are barely above background and are in agreement with the expected lack of specificity. We attribute these weak features to nonspecific adsorption and/or the possible cross-reactivity of polyclonal antibodies. More importantly, the combined weight of the results in Figure 2 further establishes the viability of our assay concept.

Dual-analyte assay. As noted earlier, another distinct feature of Raman spectroscopy is that the widths of the vibrational bands are usually much narrower than those of fluorescence bands. The Raman bands of MBA (Figure 1a) have a full-width-at-half-maximum (FWHM) of 20 cm^{-1} or 1 nm. In comparison, the fluorescence emission of fluoresceinisothiocyanate (FITC), a common fluorescence label, has a FWHM of 50 nm under ambient conditions.[44] The large widths of fluorescence bands therefore often limit the ability to easily distinguish such labels from each other, a situation that hinders the implementation of a sensitive multianalyte assay. There are only a few classes of compounds (e.g., fluorescent lanthanide complexes, 10 nm FWHM) with sufficiently narrow

emission bands that can be used as labels in a simultaneous multianalyte detection scheme.[7] In most cases, several different light sources and related optical components (e.g., filters) are required for a multianalyte immunoassay that uses different fluorescent labels. The intrinsically narrower widths of Raman bands present the potential of distinguishing many more Raman labels than is possible with fluorescent labels.[45]

To test the feasibility of our concept for dual-analyte assays, two different analytes were detected simultaneously by using two different Raman reporters, i.e., NT and TP. In these experiments, gold substrates that were coated with a mixed layer of goat anti-rat and goat anti-rabbit IgG were used to capture analytes from solution. These substrates were exposed to solutions of PBS buffer (i.e., a blank), rat IgG (1 μg/mL), rabbit IgG (1 μg/mL), or a mixture of rat (0.5 μg/mL) and rabbit IgG (0.5 μg/mL). Gold colloids that were coated with NT/anti-rat IgG or TP/anti-rabbit IgG were first prepared individually and then mixed in Tris buffer at equal amounts (a final level of ~1.5×10^{11} particles/mL for each type of colloid) for use as a detection reagent.

Figure 3a shows the spectrum of the blank sample. Ideally, the spectrum should be featureless since the sample has not been exposed to either rat IgG or rabbit IgG. As before, however, a low level of nonspecific adsorption results in the observation of low intensity vibrational bands from the labeled colloids.

The spectrum for the substrate exposed to rat IgG and the mixture of the two labeled immunogold colloids is shown in Figure 3b. This sample should capture only the colloids labeled with anti-rat IgG, so a spectrum containing only the features in Figure 1b should be obtained. The presence of the strong band at 1377 cm^{-1} for NT is consistent with this expectation. However, a much weaker band (10% of the intensity of the band at 1377 cm^{-1}) is also evident at 999 cm^{-1}. Similarly, only bands diagnostic of the TP label (Figure 1c) should be found for the sample exposed to rabbit IgG. The presence of the strong band at

999 cm^{-1} is in agreement with this prediction (Figure 3c). A weak band at 1377 cm^{-1} indicative of NT-labeled immunogold, which is probably from nonspecific adsorption, is also present (16% of the intensity of the band at 999 cm^{-1}). In comparison, when an equal amount of rat IgG and rabbit IgG are exposed to the gold substrate, both the NT ring stretching band at 1377 cm^{-1} and the TP ring in-plane bending band at 999 cm^{-1} dominate the spectrum (Figure 3d). Their intensities are roughly half of those in Figure 3b and 3c, as expected from the differences in antigen concentrations. This finding indicates that both the NT-labeled anti-rat IgG and TP-labeled anti-rabbit IgG gold colloids have bound to the substrate, demonstrating that two analytes can be simultaneously detected using easily distinguishable Raman scatterers as labels.

As noted, the bands for TP in Figure 3b and for NT in Figure 3c are probably the result of nonspecific adsorption and/or the cross-reactivity of polyclonal antibodies. It is also possible, though less likely, that there may be "cross-talk" between the two types of nanoparticles. We define cross-talk as the dissociation and re-adsorption of a weakly bound antibody from one type of labeled colloid onto another type of labeled colloid when dispersed together in the two-component detection reagent.[46] Cross-talk can be minimized by covalently coupling the antibody to the gold particles as well as by a more effective separation of the reporter-labeled immunogold from unbound antibody. Experiments to this end are underway.

Estimated detection limits. One argument favoring a fluorescence over a Raman-based detection scheme is the inherent detection capability of fluorescence measurements. However, by combining the SERS effect and the use of reporter molecules with a relatively large Raman scattering cross section as extrinsic labels, trace amounts of intrinsically weak Raman scatterers (e.g., antibodies) can be indirectly detected. For example, the presence of the weak scatterer rat IgG (1 μg/mL) was indirectly detected in Figure 2a through the

spectral signature of the MBA labels that were co-immobilized with anti-rat IgG on the surface of colloidal gold. Indeed, the extrinsic label MBA produced a strong band at 1075 cm^{-1} with signal-to-noise ratio (S/N) over 100 for an integration time of 1 s. This S/N, coupled with the concentration of rat IgG, translates to an estimated detection limit of ~30 ng/mL (0.2 nM) under these experimental conditions. We believe that by increasing modestly the signal integration time (e.g., from 1 s to 100 s), optimizing the assay conditions (e.g., incubation time and temperature), and carefully adjusting the reporter molecule coverage on the colloid surface, an even lower detection limit, which could be competitive with the detection limit based on enzymatic amplification, should be obtainable. Experiments towards a more sensitive immunoassay method are planned.

Conclusions

An alternative immunoassay readout method using SERS has been demonstrated. This indirect method employs Raman scatterers as labels bound to gold colloids that are also modified with immunospecific reagents. Two different analytes were detected simultaneously with TP and NT as their extrinsic Raman labels. The detection limit of this approach is around 10^{-9} M at current experimental conditions. By carefully designing additional Raman labeled immunogold systems, this approach has the potential to become an alternate detection method for multiple label-based immunoassays. Experiments along these lines are underway.

Acknowledgements

We express our appreciation for helpful discussions with J. R. Kenseth. This work was supported in part by NASA (Grant NAG5-6353), the Microanalytical Instrumentation Center, and the Chemical Science Division of U.S. Department of Energy. The Ames

Laboratory is operated for the U.S. Department of Energy by Iowa State University under Contract W-7405-eng-82.

References

(1) Kricka, L. J. In *Immunoassay*; Diamandis, E. P., Christopoulos, T. K., Eds.; Academic Press: New York, 1996, pp 389.

(2) Donohue, J.; Bailey, M.; Gray, R.; Holen, J.; Huang, T.-M.; Keevan, J.; Mattimiro, C.; Putterman, C.; Stalder, A.; DeFreese, J. *Clin. Chem.* **1989,** *35*, 1874.

(3) Baslund, B.; Wieslander, J. *J. Immunol. Methods* **1994,** *169*, 183.

(4) Blake, C.; Al-Bassam, M. N.; Gould, B. J.; Marks, V.; Bridges, J. W.; Riley, C. *Clin. Chem.* **1982,** *28*, 1469.

(5) Gutcho, S.; Mansbach, L. *Clin. Chem.* **1977,** *23*, 1609.

(6) Vuori, J.; Rasi, S.; Takala, T.; Vaananen, K. *Clin. Chem.* **1991,** *37*, 2087.

(7) Xu, Y.-Y.; Pettersson, K.; Blomberg, K.; Hemmila, I.; Mikola, K.; Lovgren, T. *Clin. Chem.* **1992,** *38*, 2038.

(8) Varenne, A.; Vessieres, A.; Salmain, M.; Durand, S.; Brossier, P.; Jaouen, G. *Anal. Biochem.* **1996,** *242*, 172.

(9) Hayes, F. J.; Halsall, H. B.; Heineman, W. R. *Anal. Chem.* **1994,** *66*, 1860.

(10) Beavis, A. J.; Pennline, K. J. *Cytometry* **1994,** *15*, 371.

(11) Brown, C. R.; Higgins, K. W.; Frazer, K.; Schoelz, L. K.; Dyminski, J. W.; Marinkovich, V. A.; Miller, S. P.; Burd, J. F. *Clin. Chem.* **1985,** *31*, 1500.

(12) Fotiou, F. K. *Anal. Chem.* **1992,** *64*, 1698.

(13) Rohr, T. E.; Cotton, T.; Fan, N.; Tarcha, P. J. *Anal. Biochem.* **1989,** *182*, 388.

(14) Christopoulos, T. K.; Diamandis, E. P. In *Immunoassay*; Diamandis, E. P., Christopoulos, T. K., Eds.; Academic Press: New York, 1996, pp 227.

(15) Garrell, R. L. *Anal. Chem.* **1989,** *61*, 401 A.

(16) Kneipp, K.; Kneipp, H.; Manoharan, R.; Hanlon, E. B.; Itzkan, I.; Dasari, R. R.; Feld, M. S. *Appl. Spectrosc.* **1998,** *52*, 1493.

(17) Nie, S.; Emory, S. R. *Science* **1997,** *275*, 1102.

(18) Elghanian, R.; Storhoff, J. J.; Mucic, R. C.; Letsinger, R. L.; Mirkin, C. A. *Science* **1997,** *277*, 1078.

(19) Kimura, H.; Matsuzawa, S.; Tu, C.-Y.; Kitamori, T.; Sawada, T. *Anal. Chem.* **1996,** *68*, 3063.

(20) Sakashita, H.; Tomita, A.; Umeda, Y.; Narukawa, H.; Kishioka, H.; Kitamori, T.; Sawada, T. *Anal. Chem.* **1995,** *67*, 1278.

(21) Tu, C.-Y.; Kitamori, T.; Sawada, T.; Kimura, H.; Matsuzawa, S. *Anal. Chem.* **1993,** *65*, 3631.

(22) Lyon, L. A.; Musick, M. D.; Natan, M. J. *Anal. Chem.* **1998,** *70*, 5177.

(23) Park, K.; Simmons, S. R.; Albrecht, R. M. *Scanning Microsc.* **1987,** *1*, 339.

(24) Lyon, L. A.; Keating, C. D.; Fox, A. P.; Baker, B. E.; He, L.; Nicewarner, S. R.; Mulvaney, S. P.; Natan, M. J. *Anal. Chem.* **1998,** *70*, 341 R.

(25) Vo-Dinh, T. *Trends Anal. Chem.* **1998,** *17*, 557.

(26) Dou, X.; Takama, T.; Yamaguchi, Y.; Yamamoto, H.; Ozaki, Y. *Anal. Chem.* **1997,** *69*, 1492.

(27) Kneipp, K.; Dasari, R. R.; Wang, Y. *Appl. Spectrosc.* **1994,** *48*, 951.

(28) Zeman, E. J.; Schatz, G. C. *J. Phys. Chem.* **1987,** *91*, 634.

(29) Weisbecker, C. S.; Merritt, M. V.; Whitesides, G. M. *Langmuir* **1996,** *12*, 3763.

(30) Grabar, K. C.; Smith, P. C.; Musick, M. D.; Davis, J. A.; Walter, D. G.; Jackson, M. A.; Guthrie, A. P.; Natan, M. J. *J. Am. Chem. Soc.* **1996,** *118*, 1148.

(31) Chen, S.; Murray, R. W.; Feldberg, S. W. *J. Phys. Chem. B* **1998,** *102*, 9898.

(32) Hostetler, M. J.; Zhong, C.-J.; Yen, B. K. H.; Anderegg, J.; Gross, S. M.; Evans, N. D.; Porter, M. D.; Murray, R. W. *J. Am. Chem. Soc.* **1998,** *120*, 9396.

(33) Szafranski, C. A.; Tanner, W.; Laibinis, P. E.; Garrell, R. L. *Langmuir* **1998,** *14*, 3570.

(34) Lin-Vien, D.; Colthup, N. B.; Fateley, W. G.; Grasselli, J. G. In *The Handbook of Infrared and Raman Characteristic Frequencies of Organic Molecules*; Lin-Vien, D., Colthup, N. B., Fateley, W. G., Grasselli, J. G., Eds.; Academic Press: New York, 1991, pp 277.

(35) Baudhuin, P.; Smissen, P. V. d.; Beauvois, S.; Courtoy, P. J. In *Colloidal Gold Principles, Methods, and Applications*; Hayat, M. A., Ed.; Academic Press: New York, 1989; Vol. 2, pp 1.

(36) Bohren, C. F.; Huffman, D. R. *Absorption and Scattering of Light by Small Particles*; John Wiley & Sons: New York, 1983.

(37) Zhong, C.-J.; Porter, M. D. *Anal. Chem.* **1995,** *67*, 709 A.

(38) Duan, C.; Meyerhoff, M. E. *Anal. Chem.* **1994,** *66*, 1369.

(39) Jones, V. W.; Kenseth, J. R.; Porter, M. D.; Mosher, C. L.; Henderson, E. *Anal. Chem.* **1998,** *70*, 1233.

(40) Varsanyi, G. *Assignments for Vibrational Spectra of Seven Hundred Benzene Derivatives*; John Wiley & Sons: New York, 1974.

(41) Ahern, A. M.; Garrell, R. L. *Langmuir* **1991,** *7*, 254.

(42) Keating, C. D.; Kovaleski, K. M.; Natan, M. J. *J. Phys. Chem.* **1998,** *102*, 9404.

(43) Dou, X.; Jung, Y. M.; Yamamoto, H.; Doi, S.; Ozaki, Y. *Appl. Spectrosc.* **1999,** *53*, 133.

(44) Hemmila, I. A. *Applications of Fluorescence in Immunoassays*; John Wiley & Sons: New York, 1991.

(45) Sijtsema, N. M.; Duindam, J. J.; Puppels, G. J.; Otto, C.; Greve, J. *Appl. Spectrosc.* **1996,** *50*, 545.

(46) Park, K.; Park, H.; Albrecht, R. M. In *Colloidal Gold Principles, Methods, and Applications*; Hayat, M. A., Ed.; Academic Press: New York, 1989; Vol. 1, pp 490.

(1) Creation of capture antibody surface

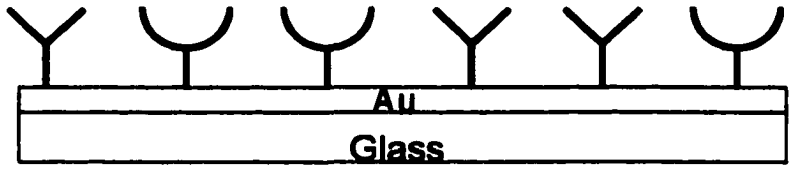

(2) Exposure to analyte

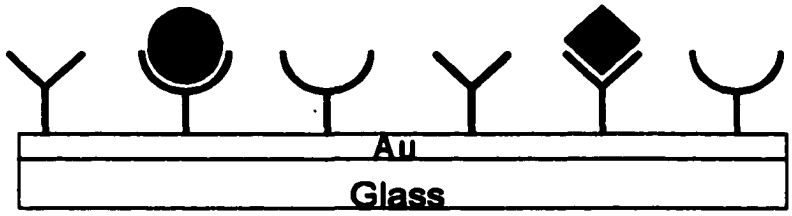

(3) Development with reporter labeled immunogold

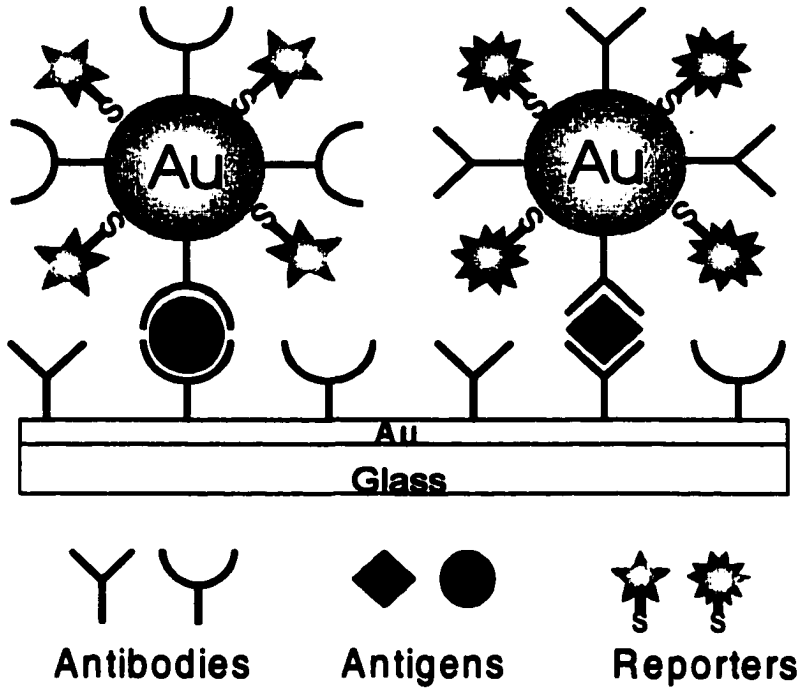

Scheme 1.

Figure Captions

Figure 1. SERS signatures of the immobilized reporter-labeled immunogold colloids: (a) gold colloids conjugated with MBA/goat anti-rat IgG, (b) gold colloids conjugated with NT/goat anti-rat IgG, (c) gold colloids conjugated with TP/goat anti-rabbit IgG, and (d) commercial gold colloids conjugated with goat anti-rat IgG. These spectra (10 s integration time) were acquired by immobilizing the labeled colloids on substrates through sandwich formation (see text for details).

Figure 2. SERS spectra from specificity tests of the reporter-labeled immunogold colloids. Gold colloids conjugated with MBA/goat anti-rat IgG were used as a detection reagent and gold substrates modified by the co-immobilization of goat anti-rat IgG and goat anti-rabbit IgG (1:1) were used as capture antibodies. SERS spectra for samples exposed to 100 μL solution (1μg/mL) of: (a) rat IgG, (b) rabbit IgG, and (c) goat IgG. All spectra were acquired under the same experimental conditions with 1 s integration times.

Figure 3. Sandwich immunoassay demonstration of the dual-analyte immunoassay concept. Gold colloids conjugated with NT/goat anti-rat IgG and gold colloids conjugated with TP/goat anti-rabbit IgG were mixed in a 1:1 ratio and used as the detection reagent. Gold substrates modified by the co-immobilization of goat anti-rat IgG and goat anti-rabbit IgG (1:1) were used as capture antibodies. SERS spectra of samples exposed to 100 μL solutions containing: (a) PBS buffer, (b) rat IgG (1 μg/mL), (c) rabbit IgG (1 μg/mL), and (d) mixture of rat IgG (0.5 μg/mL) and rabbit IgG (0.5 μg/mL). All spectra were acquired under the same experimental conditions with 10 s integration times.

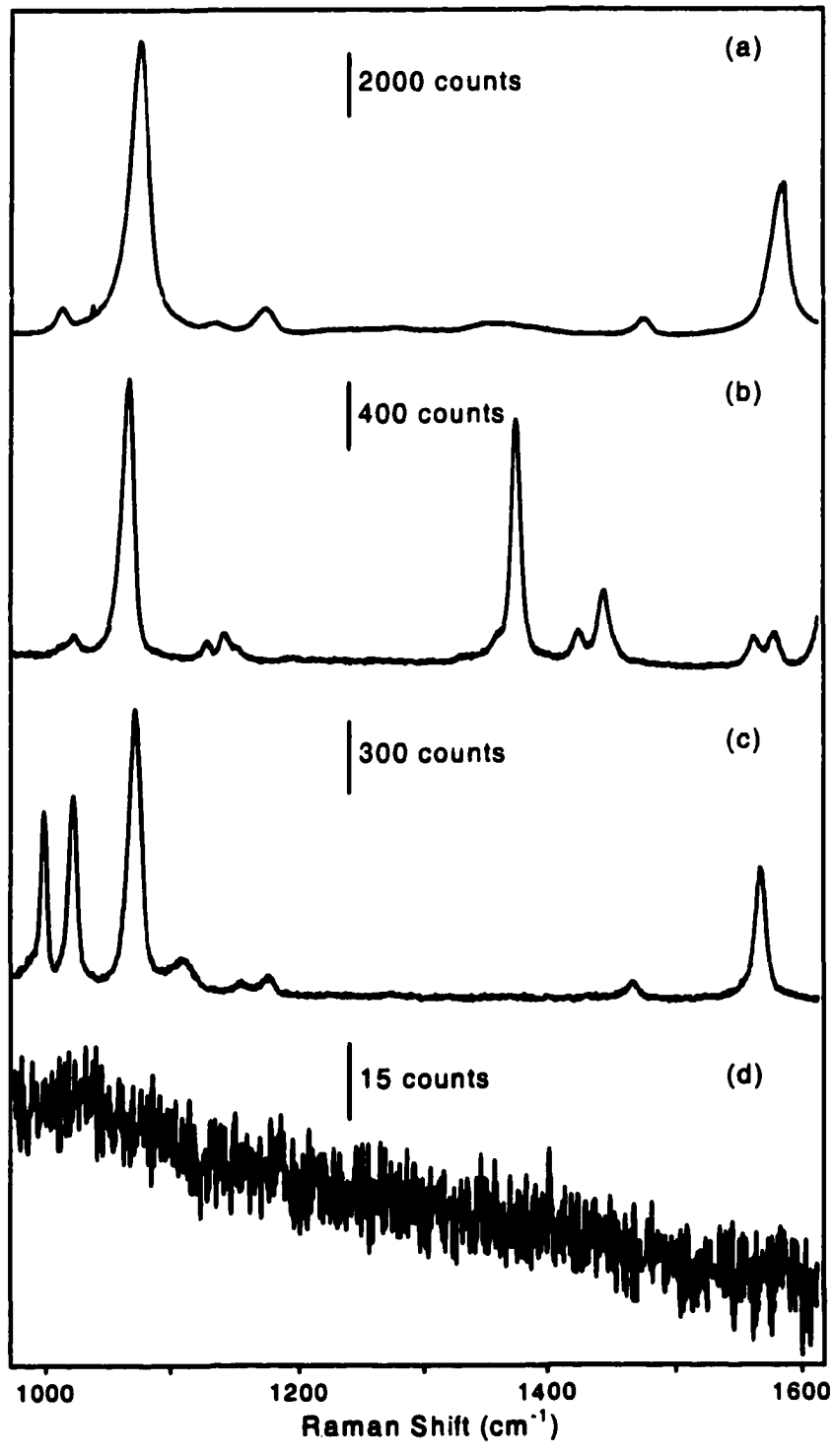
(a)
2000 counts
(b)
400 counts
(c)
300 counts
(d)
15 counts
1000
1200
1400
1600
Raman Shift (cm-1)

Figure 1.

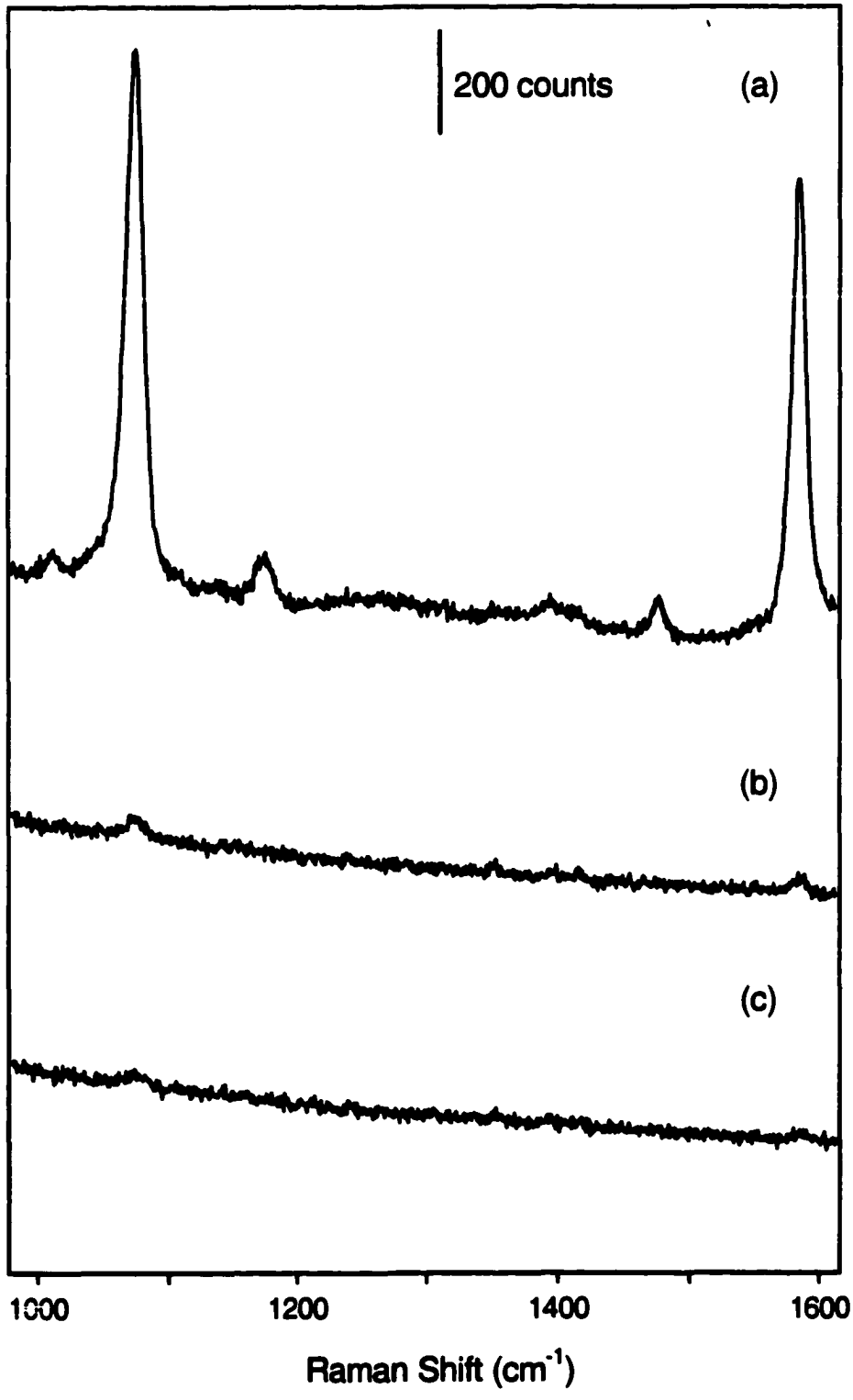

Figure 2.

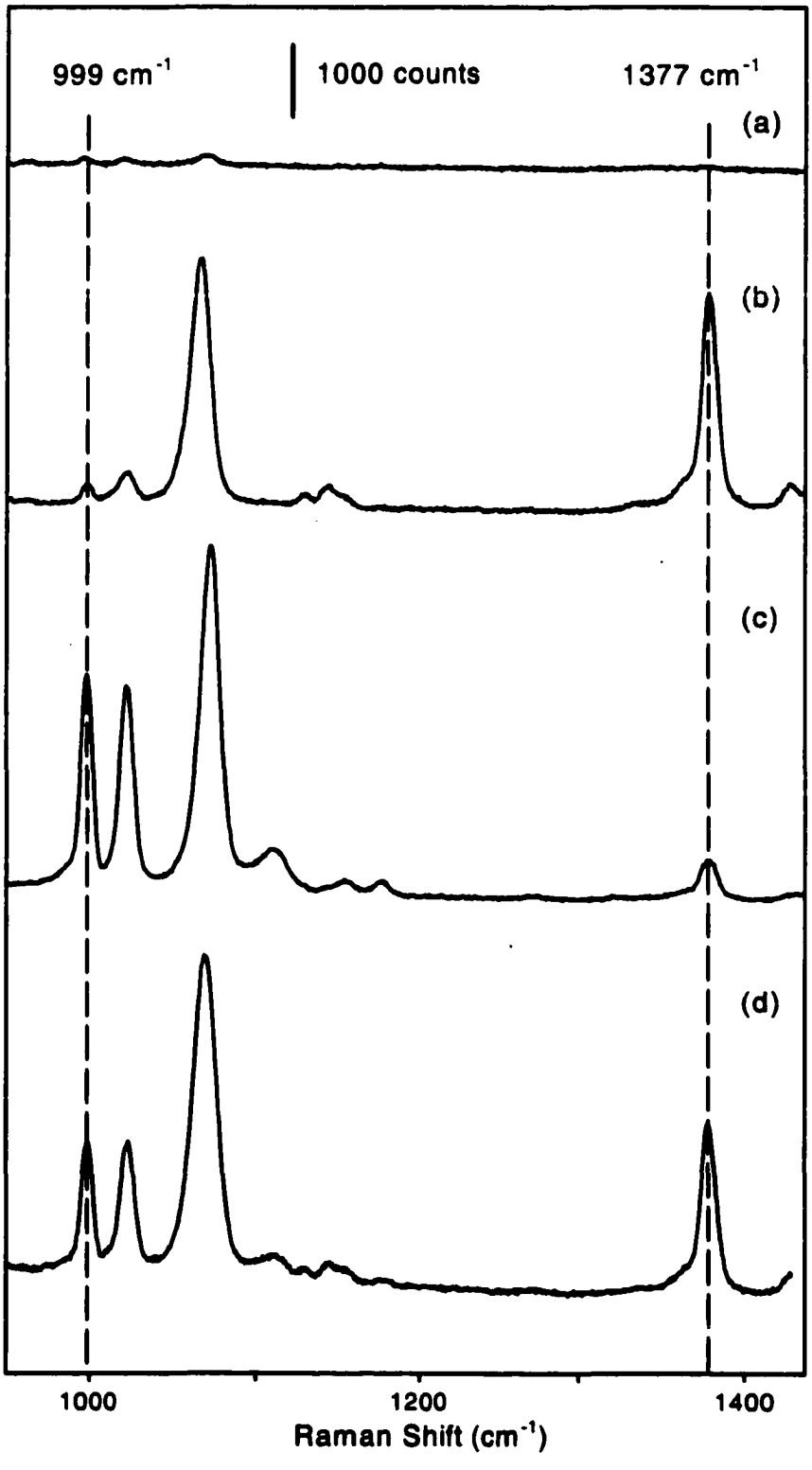
999 cm-1
1000 counts
1377 cm-1
(a)
(b)
(c)
(d)
1000
1200
1400
Raman Shift (cm-1)

Figure 3.

CHAPTER 5. RAMAN-ACTIVE COLLOIDAL GOLD REAGENTS USED FOR QUANTITATIVE IMMUNOASSAYS

A manuscript in preparation for submission to *Analytical Chemistry*

Jing Ni,[1] Robert J. Lipert,[1] Jennifer A. Harnisch,[1] and Marc D. Porter[1,2]

Abstract

An in-depth study of using surface enhanced Raman scattering (SERS) to obtain quantitative immunoassay results is presented. Two types of Raman-active immunogold colloids were used in this study. One type relied on the co-immobilization of antibodies and reporter molecules directly on the same colloidal particles; the other was based on the covalent linking of antibodies to colloids through N-succinimide groups of the reporter molecules that were pre-adsorbed on the gold colloids. The Raman-active immunogold colloidal reagent was used to detect model antigens at different concentrations in sandwich-type immunoassays, and the presence of the antigen was established by the SERS signals of the reporter molecule. The dose-response curves obtained from the sandwich assay demonstrated a large dynamic range and sub ng/mL limits of detection with colloidal detection reagents prepared by either method. The covalently-linked immunogold colloids, however, exhibited improved specificity and stability.

[1] Microanalytical Instrumentation Center, Ames Laboratory-USDOE, and Department of Chemistry, Iowa State University, Ames, IA 50011
[2] CORRESPONDING AUTHOR

Introduction

Surface enhanced Raman scattering (SERS) has demonstrated its sensitivity to detect picomole to femtomole amounts of materials on a wide range of metallic substrates (e.g., evaporated metal thin films, roughened electrodes, and metallic nanoparticles).[1, 2] A growing interest is to exploit SERS as an alternative readout method for immunoassays. This interest is not only due to the demonstrated high sensitivity of SERS, which opens the possibility of using this technique to detect trace amounts of biomolecules, but also because of its potential advantages as a broadly applicable readout method in comparison to the widely used fluorescence detection schemes.[3-5] For example, Raman scattering is not affected by oxygen and other quenchers, simplifying its use in many different experimental environments. Since the SERS signal is less subject to photobleaching, lower detection limits can be obtained by increasing the signal integration time. Moreover, Raman-active vibrational modes usually yield bands one to two orders of magnitude narrower than most fluorescence bands. This feature offers the possibility of distinguishing a much large number of different Raman labels than likely with fluorescent labels.[6, 7]

A major barrier that prohibits using SERS for the direct detection of biological samples is that the surface enhancement effect diminishes rapidly with increasing distance from metallic surfaces. In other words, strong SERS signals are observed only if the scattering centers are brought into close proximity (50-100 Å) to the surface. Although Raman spectra of biomolecules can be obtained on silver surfaces when coupling SERS and resonance enhanced scattering,[8, 9] the spectra are usually lacking of sufficient chemical content and/or signal amplitude to be used for immunoassays purposes.

Therefore, rather than relying on the SERS signal of the antibody/antigen itself, our group[6] and others[10, 11] have reported an alternative approaches to SERS-based readouts for immunoassays. Both Rohr and Dou used silver substrates and coupled surface and

resonance enhancements in a sandwich assay format. Rohr et al. employed labeled antibodies and roughened silver films coated with a capture antibody,[10] and Dou et al. exploited the adsorption on silver colloids of an enzymatically amplified immunoassay product.[11]

We have also followed the steps of a sandwich immunoassay. However, our detection approach relied solely on the SERS effect by utilizing immunogold colloids that have been labeled with Raman-active molecules as detection reagents. In this approach, gold colloids are labeled with both antibodies for bio-recognition and Raman active molecules for signal transduction. A key feature of this concept is that the scattering center of the label is positioned in close proximity of the colloid surface, which strongly enhances the signal. The presence of the antigen is therefore recognized by its detection antibody, and the SERS signal of the co-immobilized Raman active species "reports" the ligation of the antibody with the antigen.

We chose to use colloidal gold as our SERS substrate for several reasons. First, the large surface enhancement observed on some metallic nanoparticles results in SERS intensities comparable to or even exceeding those for fluorescence.[1, 2] Such a level of enhancement, which may lead to a high detection sensitivity, together with the ease of handling, make metallic nanoparticles more promising than most other types of SERS substrates for use in immunoassay applications. Second, of the varieties of metallic nanoparticles, we focused on gold over silver colloids, despite the fact that silver colloids provide larger enhancements than gold.[12] However, the size and shape distributions of colloidal gold are more uniform than that of silver,[13] which suggests a more reproducible enhancement factor, opening the possibility of using gold nanoparticles for quantitation. We note that immunogold colloids have been widely used in assays based on colorimetry,[14] photothermal deflection,[15-17] surface plasmon resonance[18], and scanning electron

microscopy[13] detection mechanisms. Nevertheless, the potential of using colloidal gold in quantitative immunosensing has not be extensively investigated.[13]

Our previous report focused on the demonstration of a simultaneous multianalyte detection concept by using different Raman reporters in conjunction with different detction antibodies.[6] It also estimated a limit of detection (LOD) of ~30 ng/mL using different IgG as antibodies and antigens. This report extends our previous work by focusing on obtaining quantitative immunoassay results using two different types of extrinsically labeled Raman-active immunogold colloids. One type was prepared following the same method used in our previous report,[6] which relied on the co-immobilization of antibodies and reporter molecules directly onto the same gold colloids. The other type was based on the covalent linking of antibodies to the colloids via functionalized reporter molecules, which was pre-chemisorbed onto the colloidal gold. Sandwich assays were performed to quantify the amount of a model antigen, and the dose-response curves obtained with colloidal reagents prepared by both methods are presented and compared.

Experimental

Reagents. Suspensions of unconjugated colloidal gold (30 nm, 2×10^{11} particles/mL) were purchased from Ted Pella, Inc. Polyclonal rat IgG, used as the antigenic analyte, and goat anti-rat IgG, used as the capture and detection antibody, were acquired from Pierce. The reporter molecule dithiobisbenzonic acid (DBA) was purchased from Toronto Research Chemicals, Inc, and 4,4'-dithiobis(succinimidylbenzoinate) (DSB) was synthesized according to literature procedures (see below). Thioctic acid (98%), 1-ethyl-3-[3-(dimethylamino)propyl] carbodiimide (EDC), N-hydroxysuccinimide (NHS), 1,3-dicyclohexylcarbodiimide (DCCD), and Tween 80 were obtained from Aldrich. Sodium tetraborate decahydrate, potassium phosphate, tris(hydroxymethyl)aminomethane (Tris),

sodium chloride, and magnesium chloride were purchased from Fisher. All biological reagents were used within 6 months after purchasing.

Instrumentation. The experimental setup for the SERS measurements is shown in Figure 1. The signal was excited with a diode laser (Hitachi HL7851G, Thorlabs) operated at 20 °C and 120 mA. These conditions produced 50 mW of output power at the sample with a wavelength of 785.13 nm. A polarization rotator adjusted the polarization direction of the laser to minimize reflection losses at the Pellin-Brocha prisms. The prisms were used to remove background laser emission. The laser beam was then directed by a mirror through an aperture and focused by a 50-mm focal length cylindrical lens to a 3 mm by 0.25 mm line on the sample surface. The laser beam irradiated the sample at an angle of ~60° with respect to the surface normal, and the scattered light was collected and focused onto the entrance slit of the monochromator with a *f*/2 lens. A holographic notch filter (HSPF-785.0, Kaiser Optical Systems) was used to block the Rayleigh scattering light, while the Raman scattered light passed through the entrance slit (200 μm slit width) of a 300 mm *f*/4 spectrograph (SpectraPro 300i, Acton Research Corp.) and illuminated onto a 1200 grooves/mm grating. The grating was blazed for 750 nm and produced a nominal dispersion of 2.7 nm/mm. A thinned, back-illuminated, liquid nitrogen-cooled CCD (LN/CCD-1100PB, Princeton Instruments) was controlled by a PC for spectra acquisition. The positions of the reporter molecule Raman bands were determined by calibration using the known band positions of solid naphthalene.

Synthesis of 4,4'-dithiobis(succinimidylbenzoate) (DSB). The synthesis of DSB followed a procedure similar to that used for preparing dithio-bis(succinimidylundecanoate).[19] Briefly, 0.50 g of DBA (1.6 mmol), 0.67 g of DCCD (3.2 mmol), 0.37 g of NHS (3.2 mmol), and 60 mL of tetrahydrofuran were added to a 100 mL round-bottom flask equipped with a magnetic stir bar and drying tube. The reaction mixture

was stirred at room temperature for three days. The solution was then filtered and the solvent was removed under reduced pressure to give an oily yellow residue. The crude product was dissolved in hot acetone and filtered again. Hexane was added to the filtrate until the solution became cloudy and the acetone:hexane mixture was stored in the refrigerator at 4 °C overnight. The product separated as an orange oil. ^{1}H-NMR (400 MHz, $CDCl_3$): δ 7.86 (d, 4H), 7.41 (d, 4H), 2.71 (s, 8H). Infrared reflection spectroscopy: 1810 cm^{-1} ($\nu_{(C=O)}$ of the ester), 1772 cm^{-1} ($\nu_{s(C=O)}$ of the succinimide), 1746 cm^{-1} ($\nu_{as(C=O)}$ of the succinimide), 1585 cm^{-1} ($\nu_{(C=C)}$ of the benzene ring).[20, 21]

Preparation of Raman-active immunogold colloids. Raman-active immunogold colloids were prepared by two approaches shown in Scheme 1.

(i) Co-immobilization approach. The co-immobilization approach, we also used in our previous report,[6] consists of the two steps depicted in Scheme 1a. First, 25 μL of ethanolic Raman reporter solution (0.5 mM DBA) was added to 10 mL of a suspension of uncoated gold colloids (~30 nm diameter). The mixture was allowed to react for 5 h at room temperature. During this step, the reporter molecules bind via self-assembly onto the colloid surface through the formation of sulfur-gold linkages.[22-25] We note that this amount of reporter, based on an estimation of the colloidal surface area, will only partially cover the colloid, leaving portions of the uncoated colloidal surface available for protein immobilization. After separating the reporter-labeled colloids from solution by centrifugation at 14,000 g for 4 min, the loosely-packed, red-colored sediment was resuspended in 10 mL of borate buffer (2 mM, pH 9).

These Raman-active colloids were next immuno-labeled by adding 230 μg of goat anti-rat IgG to 10 mL of the above suspension. The mixture was incubated at 4°C for 12 h, during which the IgG protein adsorbs directly onto the exposed colloidal surface through a

combination of ionic and hydrophobic interactions.[26] The incubation was followed by centrifugation at 14,000 g for 5 min, and the loose sediment of reporter-labeled immunogold was rinsed by resuspending in 2 mM borate buffer and collected after a second centrifugation. Finally, the labeled colloids were suspended in 10 mM Tris-buffered saline (Tris/HCl, NaCl 10 mM, $MgCl_2$ 1.5 mM, pH 7.6) giving a concentration of ~2 x 10^{11} particles/mL. Tween 80 (1%) was also added to the suspension to minimize nonspecific adsorption in the assays. The suspensions usually remained uniformly dispersed for 2-3 days when stored at 4 °C.

(ii) Covalent linking approach. The DSB molecules were used as both Raman reporters and antibody linkers. The succinimide group of the DSB molecule can readily react with the primary amine group of an amino acid, such as the lysine, presented in antibodies like IgG to form a covalent bond. As shown in Scheme 1b, the preparation of the covalently-linked colloidal reagent follows a process very similar to that used for the co-immobilized reagents. However, with the covalent linking approach, the antibodies indirectly attached to the colloid through the reporter molecules rather than directly adsorbed onto the colloidal surface. Briefly, 25 μL of a reporter-linker solution (5 mM DSB in $CHCl_3$) was added to 10 mL of bare gold suspension (30 nm) under vigorous agitation. The molecules self-assemble onto the colloid surface, with their succinimide end groups available for protein immobilization. It is noted that this amount of the reporter-linker is estimated to be more than enough to cover the entire colloidal surface. The reporter-linker labeled colloids were centrifuged, and resuspended in the aforementioned borate buffer.

Similar to the co-immobilization approach, 230 μg of goat anti-rat IgG were added to the 10 mL suspension of the DSB-labeled gold colloids, followed by a incubation at 4°C for 12 h. This step covalently couples anti-rat IgG molecule to the colloid surface via amide linkages that are formed by the reactions of its amine groups with the succinimde groups of

DSB. Finally, the Raman-active immunogold was rinsed and resuspended in Tris buffer, and the final concentration of the colloids was adjusted to ~2 x 10^{11} particles/mL. The suspensions were usually stable for a few weeks when stored at 4 °C.

Preparation of gold films. Gold films were deposited onto clean glass microscope slides by resistive evaporation at a pressure of <1.3 x 10^{-4} Pa. Gold island films, which were used as the SERS substrates in Raman reporter characterization experiments, were prepared by evaporating ~5 nm of gold directly onto the glass substrate. These island films were then derivatized with reporter molecules by immersion in 1 mM DBA (in ethanol) or 1 mM DSB (in chloroform) solutions for 24 h, and subsequently rinsed with the corresponding neat solvents before SERS characterization. Smooth gold films were prepared by first coating a glass substrate with 15 nm of chromium followed by 300 nm of gold. These substrates were used to prepare capture antibody substrates for the immunoassay experiment described below.

Preparation of capture antibody substrates. Capture antibody substrates were prepared as previously described.[6] In summary, a thioctic acid monolayer was first formed on a smooth gold substrate, and activated with EDC in anhydrous acetonitrile. The surface was then modified with capture antibody by pipetting 100 μL of goat anti-rat IgG (100 μg/mL, 0.1 M borate buffer, pH 9) onto ~1 cm^2 of the activated substrate. This reaction was allowed to progress at 4 °C for 12 h. Finally, the antibody-coated substrates were rinsed with deionized water, and quickly dried under a stream of argon. All assays were conducted using freshly prepared substrates.

Immunoassay protocol. The dose-response curve was constructed based on the results of a set of sandwich assays.[27] Samples containing Rat IgG as a model antigen were prepared at concentrations ranging from 0.01 ng/mL to 1 mg/mL in 50 mM PBS buffer (KH_2PO_4/K_2HPO_4, 150 mM NaCl, pH = 7.6). A 100 μL aliquot of each sample solution was

pipetted onto separate capture antibody substrates and allowed to react for 1 h at room temperature. After rinsing with copious amounts of water, the substrates were then exposed to 100 μL of reporter-labeled immunogold solution for 3 h. All substrates were rinsed with deionized water and dried under argon before SERS characterization.

Results and Discussion

UV-Vis characterization of gold island films. Gold island films were used as SERS-active substrates to examine the scattering properties of the acid-terminated DBA and succinimide-terminated DSB reporters. To minimize differences caused by substrate variability, the gold island films (~5 nm thick) were first examined using UV-Vis spectrometer. Figure 2 shows the spectra of two such films (spectra a and b) before immersion in the reporter molecule solution. For comparison, spectrum c was collected from 5 nm colloidal gold suspended in aqueous solution. Both island films exhibited a plasmon resonance band with a maximum of 597 nm, while that for colloidal gold was at 519 nm. The plasmon bands from the island films were also wider than that observed from uniformly dispersed 5 nm colloidal gold. The difference in the spectra of the 5 nm-thick gold island films and the 5-nm diameter gold colloid suspension can be explained by the distribution of sizes and shapes of the nanostructures on the two different types of samples. Evaporated gold islands usually have a broad size distribution with different irregular shapes.[28] Colloidal gold, on the other hand, is reported to be more uniform in size and have a near-spherical shape.[13]

It is more important to note that the spectra for the two island films are effectively superimposable. This agreement argues that the average sizes and shapes of the islands on the two substrates are strongly similar. As a result, both substrates should have similar

surface plasmon properties and therefore produce similar magnitudes of surface enhancement for Raman scattering.[12]

SERS characterization of DBA and DSB reporter molecules. The purpose of this set of experiments was to determine the difference in the reporter scattering properties as a result of altering the terminal functional groups in the reporter molecule. SERS spectra (10 s integration time) of self-assembled monolayers of DBA and DSB on the gold island films are shown in Figure 3. Several strong aromatic vibrational bands from the benzene ring are present within this spectral region. The strongest band at 1075 cm^{-1} is from the aromatic C-H in-plane bending, and another major band at 1585 cm^{-1} is from the C=C ring stretching.[29] To obtain maximum sensitivity, signals at 1075 cm^{-1} were used as readout in both the DBA and DSB-based immunoassays. The similar intensities of this band in the two spectra of Figure 3 agree to what we expected based on the similarity in the molecular structures of the two types of reporters. We also note that the intensity ratios of the peak at 1075 cm^{-1} to the peak 1585 cm^{-1} in the two spectra are slightly different, possibly reflecting the orientation difference of the two types molecules when adsorbed on surface.

There are two additional bands observed in the DBA spectrum, both with very low intensities. The band at 1420 cm^{-1}, which appears as a shoulder on the broad glass band (i.e., Si-O stretches) around 1390 cm^{-1}, is strongly characteristic of a COO^- symmetric vibration, while the 1150 cm^{-1} band in the DBA spectra is tentatively assigned to a C-OH stretching mode. In summary, replacing the carboxylate group with succinimide group has only a minor influence on SERS signal derived from the benzene structure in the DBA and DSB molecules. The Raman signatures from the carboxylate group diminished in the DSB spectrum, verifying the synthesis product.

Dose-response curves. The strongest SERS band at 1075 cm^{-1} was used as readout in the immunoassay experiments. Figure 4 plots the intensity of this band versus

the concentration of the antigen, rat IgG, with either the co-immobilized (4a) or the covalently-linked colloids (4b) as detection reagent. In both experiments, SERS signals show proportional response to the antigen concentration almost over the entire tested concentration range, representing a dynamic range of nearly 8 orders of magnitude. The solid lines represent the curve fitting of the immunoassay data based the four-parameter logistic model, a common regression model used for describing sandwich type immunoassays.[30] The slope of the curve suggests how the readout signals quantify samples of different concentration; the larger the slope, the easier the distinction. Two important parameters obtained from the curve fitting will be discussed with more details in the later sections. One is the expected signal at zero dose, which is also called the negative control signal, the other is the expected signal at infinitely high or saturation dose, which is also called the positive control signal.

Limits of detection. When working with samples at low concentration, we found it was more difficult to distinguish the analyte signal (S) accurately from that at zero dose than from the spectral noise (N). For example, even the signals from the negative control samples, were readily distinguishable from the noise in the spectra with S/N larger than 3 in both experiments. We therefore define the limit of detection (LOD) as the concentration associated with a response three times the mean response obtained at zero dose. The LOD is around 0.22 ng/mL when employing the co-immobilized reagent, but lowered to 0.04 ng/mL with the use of the covalently-linked reagent.

The difference in LOD is largely due to the different SERS intensities observed for the two negative control samples, which were obtained through the same assay procedure, using samples at a concentration of zero (i.e., buffer only). Indeed, the difference in the negative control signals, which reflect different extents of nonspecific binding, is a major difference between the two sets of results. The colloidal reagent prepared using the co-

immobilization approach seemed to yield a more pronounced nonspecific binding, and therefore, a higher Raman signal (145 counts) for the negative control sample (from curve fitting, S is 164 counts at zero concentration). In comparison, the colloids modified via the covalent linking approach yielded a much lower signal (22 counts) from the negative control (32 counts based on curve fitting).

Scanning Electron Microscopy images of these sample surfaces showed that a higher colloid density was observed on the capture antibody substrate when using the co-immobilized reagent, supporting the conclusion that a higher extent of nonspecific binding occurs with these samples. We attribute the increased nonspecific binding of the co-immobilized colloids to the weak interaction between the antibody and the colloid surface. This interaction is weakened due to the partial coverage of the reporter molecules on the colloid surface, which reduces the surface area on a colloid that can interact with the antibody and hence weakens the binding. This weak interaction can result in vacancies on the reporter-labeled immunogold colloid, and lead to its nonspecific binding with the antibodies on the capture substrate. Covalent coupling reduces this complication, which in turn, lowers the amount of nonspecific binding.

In addition to the negative control signal, all the spectra obtained with the covalently-linked colloidal reagent were of lower intensity than those obtained with the co-immobilized colloid for samples of same concentration. Based on the characterizations on the gold island film in Figure 3, we do not believe that the lower intensity observed with the covalently-linked immunogold is due to the difference in the Raman scattering intensity between the DSB and DBA molecules. We suspect that the lower signal in Figure 4b may arise from an increased extent of antibody denaturation due to covalent linking, which lowers the "active" detection antibody levels on the colloid surface. It is also possible that

the difference in intensities reflects a more extensive nonspecific binding when using the co-immobilized colloids.

It is important to note that, although the co-immobilized colloids yielded much higher absolute Raman signals, the relative signals that normalized to the signal at zero dosage were always higher when using the covalently-linked reagent for detection. The curve fitting results show, for example, that the expected signal at the saturation dosage for the co-immobilized reagent is almost 2.5 times higher than that obtained using the covalently-linked reagent. However, the ratio for the signals at saturation dosage with respect to those at zero dosage is 50% larger for the covalently-linked reagent. The higher ratio suggests a sharper contrast between the positive and the negative control signal and therefore a more accurate distinction between an analyte and a blank sample.

Reproducibility. The colloidal suspension prepared from the covalent linking approach was also more stable in solution and less susceptible to aggregation. These observations explain the lower run-to-run variation observed when using the covalently-linked reagent (~10%) compared to that when using the co-immobilized reagent (>20%). We also noted that when starting with a new batch of reporter-labeled immunogold reagent, the batch-to-batch variation was even more significant and sometimes up to 100% when using the co-immobilized reagent. We suspect this difference represents the importance of the first step in the colloid modification. It is less critical in the covalent linking approach because DSB was always added at a level to ensure the exhaustive coverage of the reporters on every colloid. However, it is very critical in the co-immobilization approach since the dosage of DBA determined the reporter coverage on each colloid and hence the signal intensity per colloid.

Conclusions

Raman active immunogold colloids were prepared via two different approaches and used in sandwich-type immunoassays. The co-immobilized reagent relied on the direct adsorption of antibodies and reporter molecules onto the same colloid, while the covalently-linked reagent was based on the covalent linking of antibodies to colloids through N-succinimide groups of the reporter molecules. Dose-response curves of the model antigen rat IgG showed dynamic ranges of more than eight orders of magnitude with either type of colloid. The LOD was 0.04 ng/mL when using the covalently-linked reagent, and 0.22 ng/mL when using co-immobilized reagent. The covalently-linked reagent also had longer shelf life, and showed better specificity and reproducibility in the immunoassay. Experiments aimed at detecting analytes in more complex matrices are planned to evaluate the potential usage of such colloidal detection reagent in a range of important applications.

Acknowledgments

J. N. gratefully acknowledges the support of the ACS Analytical Division Fellowship that is sponsored by the Eastman Chemical Company. This work was supported in part by NASA (Grant NAG5-6353), the Microanalytical Instrumentation Center, and the Chemical Science Division of U.S. Department of Energy. The Ames Laboratory is operated for the U.S. Department of Energy by Iowa State University under Contract W-7405-eng-82.

References

(1) Kneipp, K.; Kneipp, H.; Manoharan, R.; Hanlon, E. B.; Itzkan, I.; Dasari, R. R.; Feld, M. S. *Appl. Spectrosc.* **1998**, *52*, 1493.

(2) Nie, S.; Emory, S. R. *Science* **1997**, *275*, 1102.

(3) Lyon, L. A.; Keating, C. D.; Fox, A. P.; Baker, B. E.; He, L.; Nicewarner, S. R.; Mulvaney, S. P.; Natan, M. J. *Anal. Chem.* **1998,** *70*, 341 R.

(4) Garrell, R. L. *Anal. Chem.* **1989,** *61*, 401 A.

(5) Vo-Dinh, T. *Trends Anal. Chem.* **1998,** *17*, 557.

(6) Ni, J.; Lipert, R. J.; Dawson, B.; Porter, M. D. *Anal. Chem.* **1999,** *71*, 4903.

(7) Sijtsema, N. M.; Duindam, J. J.; Puppels, G. J.; Otto, C.; Greve, J. *Appl. Spectrosc.* **1996,** *50*, 545.

(8) Hashimoto, S.; Nakajima, R.; Yamazaki, I.; Kotani, T.; Ohtaki, S.; Kitagawa, T. *FEBS Lett.* **1989,** *248*, 205.

(9) Lee, N.-S.; Hsieh, Y.-Z.; Morris, M. D.; Schopfer, L. M. *J. Am. Chem. Soc.* **1987,** *109*, 1358.

(10) Rohr, T. E.; Cotton, T.; Fan, N.; Tarcha, P. J. *Anal. Biochem.* **1989,** *182*, 388.

(11) Dou, X.; Takama, T.; Yamaguchi, Y.; Yamamoto, H.; Ozaki, Y. *Anal. Chem.* **1997,** *69*, 1492.

(12) Bohren, C. F.; Huffman, D. R. *Absorption and Scattering of Light by Small Particles*; John Wiley & Sons: New York, 1983.

(13) Park, K.; Simmons, S. R.; Albrecht, R. M. *Scanning Microsc.* **1987,** *1*, 339.

(14) Elghanian, R.; Storhoff, J. J.; Mucic, R. C.; Letsinger, R. L.; Mirkin, C. A. *Science* **1997,** *277*, 1078.

(15) Kimura, H.; Matsuzawa, S.; Tu, C.-Y.; Kitamori, T.; Sawada, T. *Anal. Chem.* **1996,** *68*, 3063.

(16) Sakashita, H.; Tomita, A.; Umeda, Y.; Narukawa, H.; Kishioka, H.; Kitamori, T.; Sawada, T. *Anal. Chem.* **1995,** *67*, 1278.

(17) Tu, C.-Y.; Kitamori, T.; Sawada, T.; Kimura, H.; Matsuzawa, S. *Anal. Chem.* **1993,** *65*, 3631.

(18) Lyon, L. A.; Musick, M. D.; Natan, M. J. *Anal. Chem.* **1998,** *70*, 5177.

(19) Wagner, P.; Hegner, M.; Kernen, P.; Zaugg, F.; Semenza, G. *Biophys. J.* **1996,** *70*, 2052.

(20) Kenseth, J.; Wong, S.-S.; Takano, H.; Jones, V.; Porter, M. , Tokyo, Japan 1999; Waseda University Press, Tokyo, Japan; 179.

(21) Frey, B. L.; Corn, R. M. *Anal. Chem.* **1996,** *68*, 3187.

(22) Weisbecker, C. S.; Merritt, M. V.; Whitesides, G. M. *Langmuir* **1996,** *12*, 3763.

(23) Grabar, K. C.; Smith, P. C.; Musick, M. D.; Davis, J. A.; Walter, D. G.; Jackson, M. A.; Guthrie, A. P.; Natan, M. J. *J. Am. Chem. Soc.* **1996,** *118*, 1148.

(24) Chen, S.; Murray, R. W.; Feldberg, S. W. *J. Phys. Chem. B* **1998,** *102*, 9898.

(25) Hostetler, M. J.; Zhong, C.-J.; Yen, B. K. H.; Anderegg, J.; Gross, S. M.; Evans, N. D.; Porter, M. D.; Murray, R. W. *J. Am. Chem. Soc.* **1998,** *120*, 9396.

(26) Baudhuin, P.; Smissen, P. V. d.; Beauvois, S.; Courtoy, P. J. In *Colloidal Gold Principles, Methods, and Applications*; Hayat, M. A., Ed.; Academic Press: New York, 1989; Vol. 2, pp 1.

(27) Christopoulos, T. K.; Diamandis, E. P. In *Immunoassay*; Diamandis, E. P., Christopoulos, T. K., Eds.; Academic Press: New York, 1996, pp 227.

(28) Parmigiani, F.; Samoggia, G.; Ferraris, G. P. *J. Appl. Phys.* **1985,** *57*, 2524.

(29) Varsanyi, G. *Assignments for Vibrational Spectra of Seven Hundred Benzene Derivatives*; John Wiley & Sons: New York, 1974.

(30) Christopoulos, T. K.; Diamandis, E. P. In *Immunoassay*; Diamandis, E. P., Christopoulos, T. K., Eds.; Academic Press: New York, 1996, pp 25.

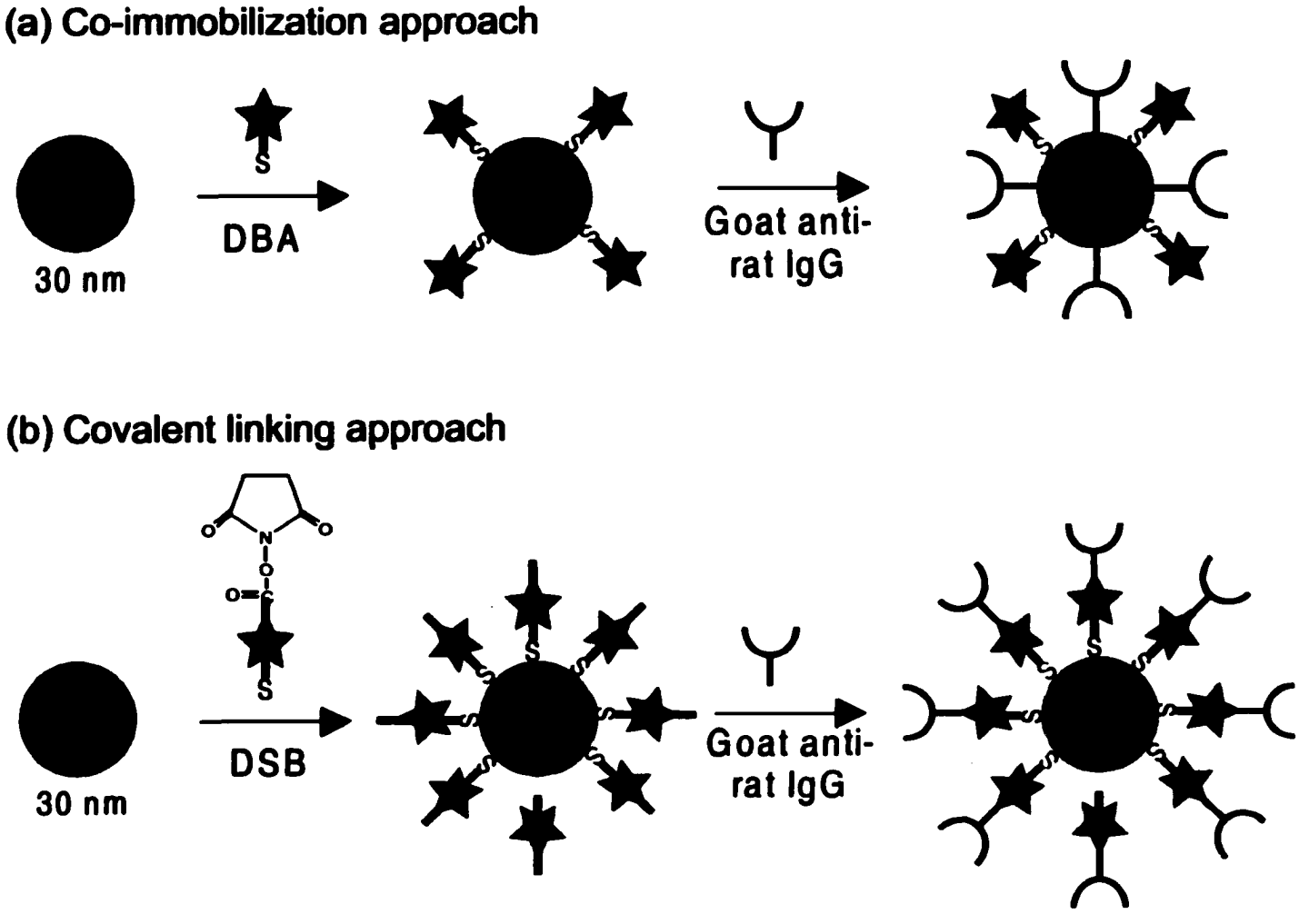
(a) Co-immobilization approach
30 nm
S
DBA
Goat anti-
rat IgG
(b) Covalent linking approach
O
N
O
O=C
S
30 nm
DSB
Goat anti-
rat IgG

Scheme 1.

Figure Captions

Figure 1. Experimental setup for SERS measurements. P: polarization rotator; PB1 and PB2: Pellin Brocha prisms; M: mirror; A: aperture; L1: cylindrical lens; S: sample slide; L2: collection lens; NF: notch filter. See text for details.

Figure 2. UV-Vis spectra for SERS substrate characterization. (a) and (b) were obtained from ~5 nm thick gold island films evaporated onto glass slides; a bare glass slide was used as the spectral blank. (c) was obtained from a colloidal gold (5 nm) suspension in a 1 cm path length glass cuvett; deionized water was used as the blank.

Figure 3. SERS spectra of the DBA and DSB reporter molecules adsorbed on gold island film substrates: (a) DBA, (b) DSB. Both spectra were acquired under the same experimental conditions with 10 s integration times (see text for details).

Figure 4. Dose-response curves of the intensity of the strongest SERS band (1075 cm^{-1}) versus the rat IgG concentration: (a) using the colloidal detection reagent prepared via the co-immobilized approach, (b) using the colloidal detection reagent prepared via the covalent linking approach. All the experimental data was acquired under the same experimental conditions with 10 s integration times. The error bars represent the variation of SERS signal for five different measurements across the same sample surface. The solid lines represent the curve fitting results of the experimental data based a four-parameter logistic model.

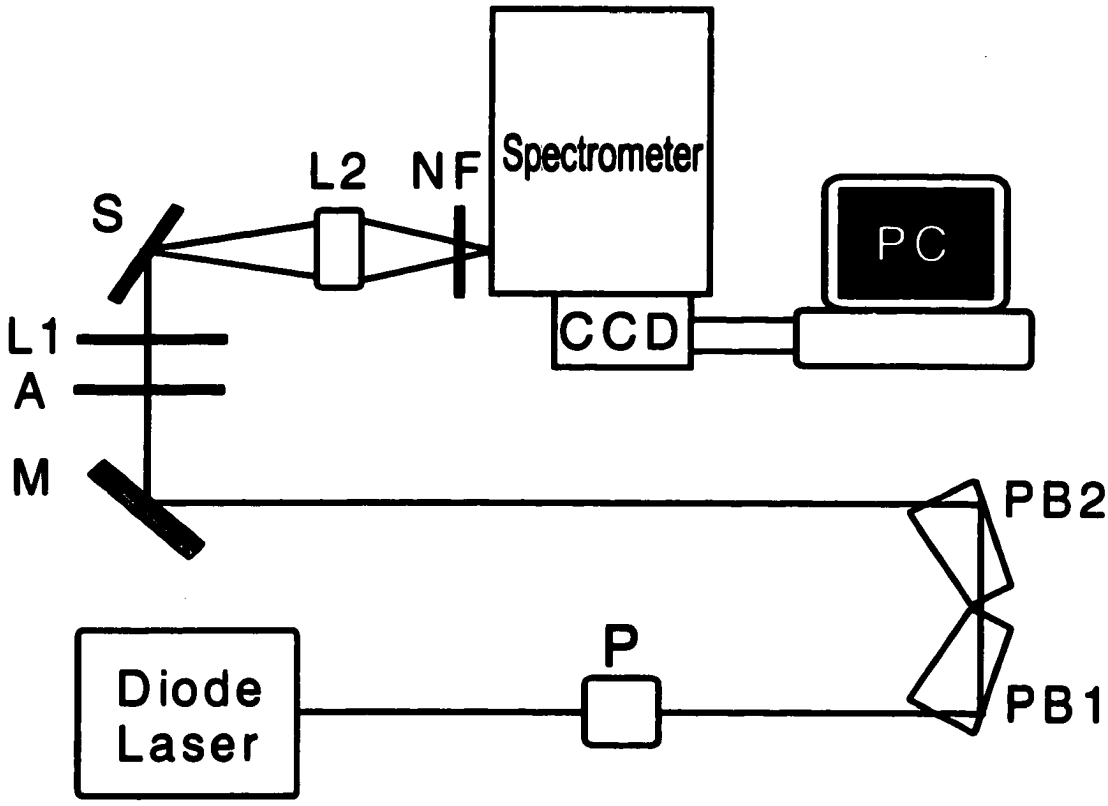

Figure 1.

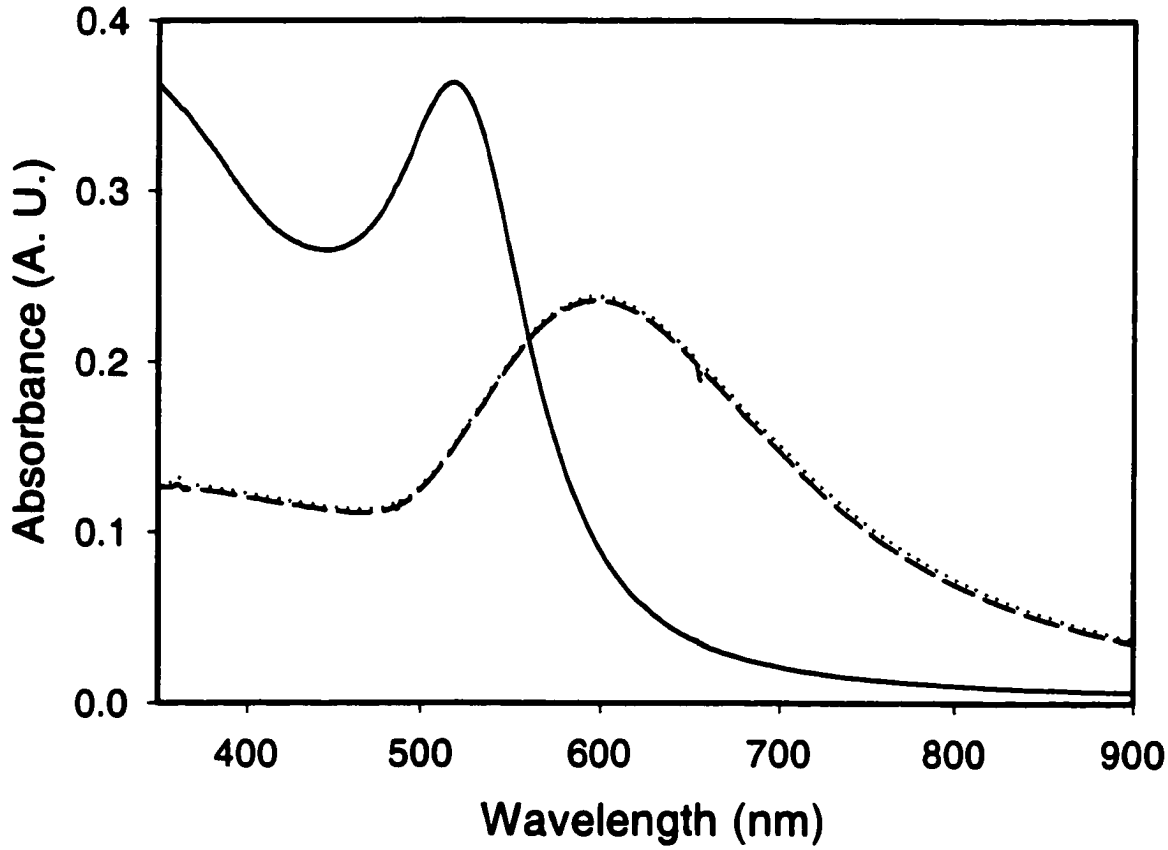
0.4
0.3
0.2
0.1
0.0
Absorbance (A. U.)
400
500
600
700
800
900
Wavelength (nm)

Figure 2.

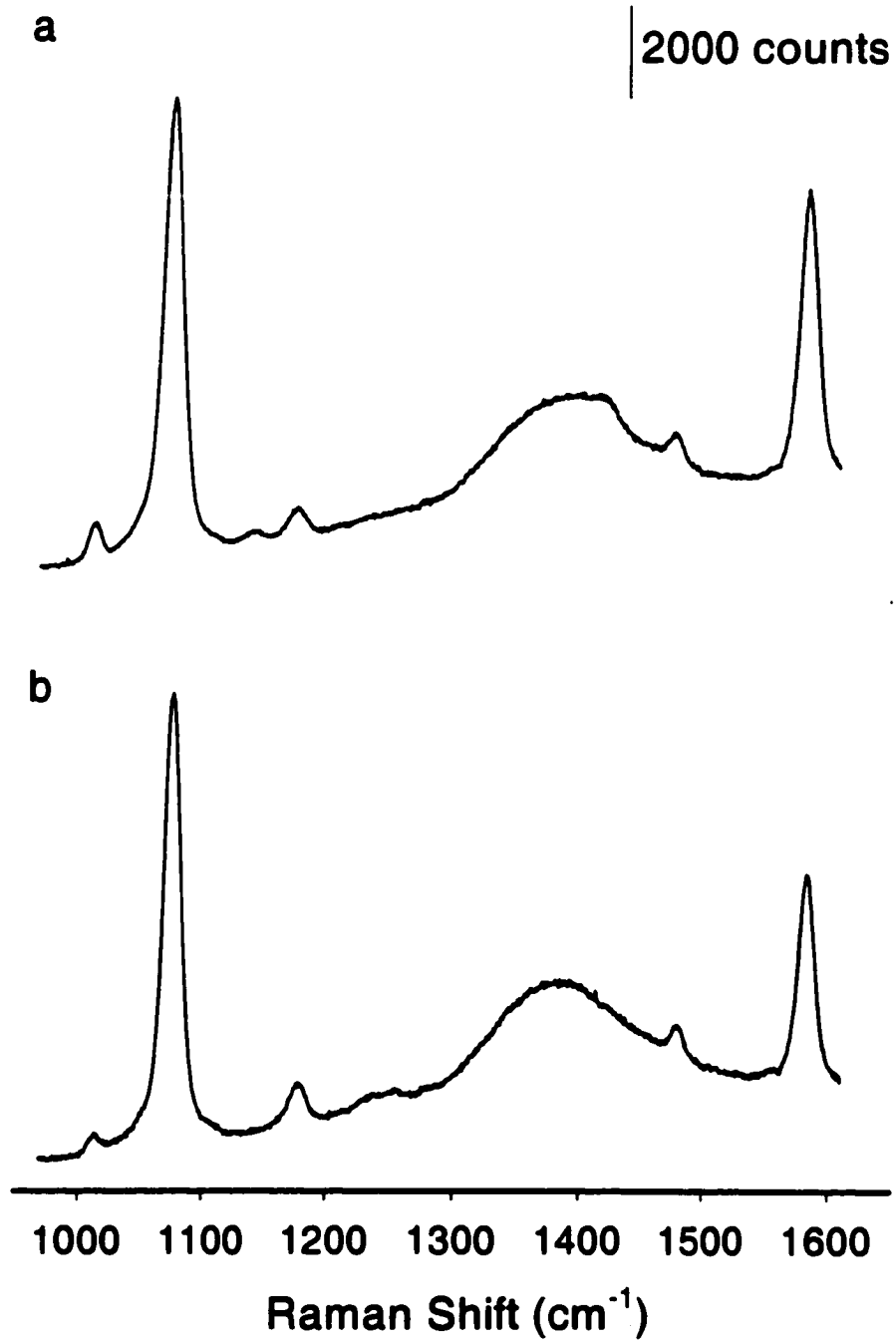
a
2000 counts
b
1000
1100
1200
1300
1400
1500
1600
Raman Shift (cm-1)

Figure 3.

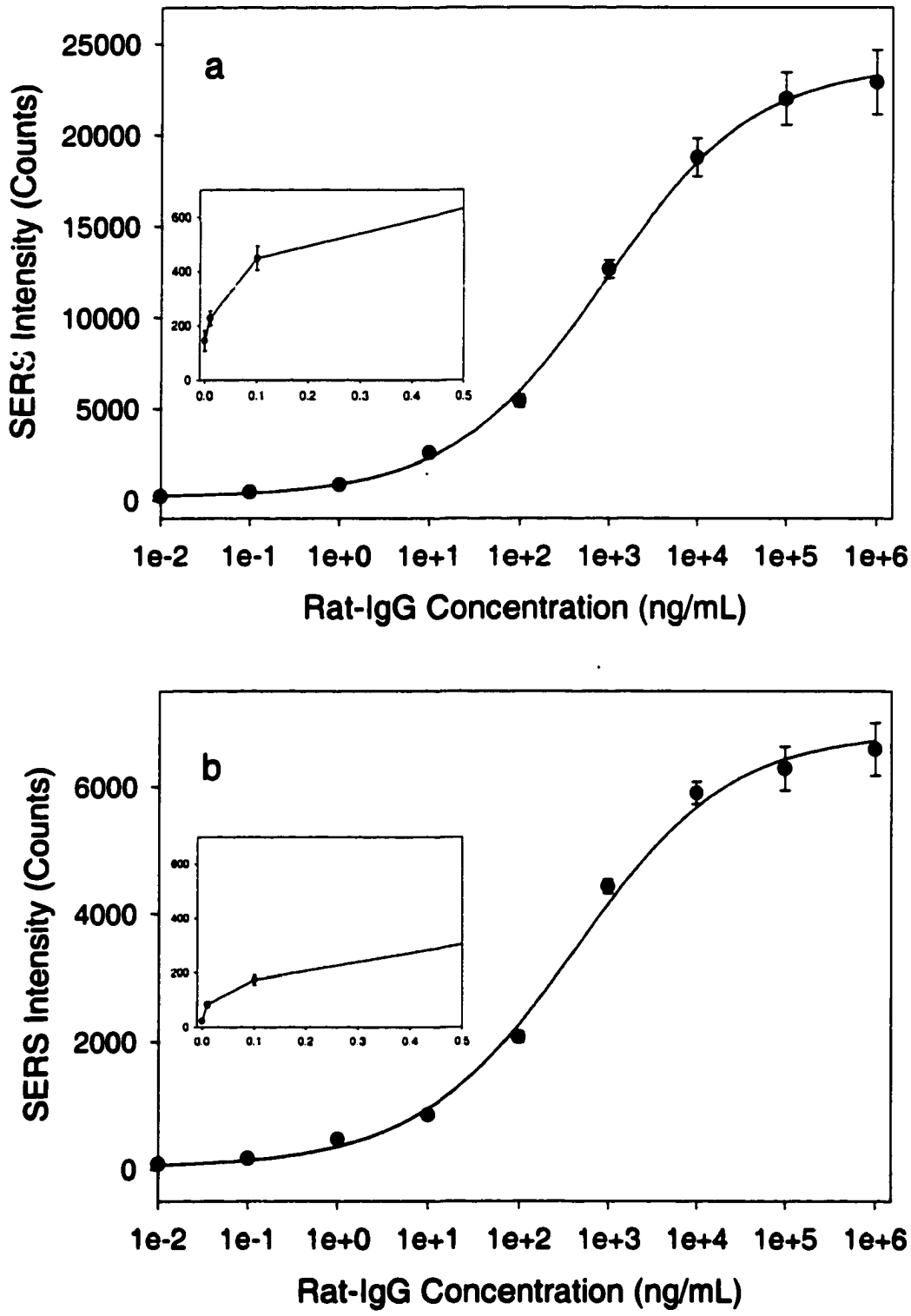
a
SERS Intensity (Counts)
25000
20000
15000
10000
5000
0
600
400
200
0
0.0
0.1
0.2
0.3
0.4
0.5
1e-2
1e-1
1e+0
1e+1
1e+2
1e+3
1e+4
1e+5
1e+6
Rat-IgG Concentration (ng/mL)
b
SERS Intensity (Counts)
6000
4000
2000
0
600
400
200
0
0.0
0.1
0.2
0.3
0.4
0.5
1e-2
1e-1
1e+0
1e+1
1e+2
1e+3
1e+4
1e+5
1e+6
Rat-IgG Concentration (ng/mL)

Figure 4.

GENERAL CONCLUSIONS

Research Overview

The main objective of my doctoral research is to design, create, and test new methods for high throughput chemical and biological analyses. Approaches have taken two parallel directions. The first approach takes advantage of micromachining technology to miniaturize widely used analytical instruments. This new class of instruments not only represents an extensive size reduction for payload minimization but also greatly reduces the consumption of materials and the generation of wastes. Specifically, this effort focused on developing a chip-scale liquid chromatographic (LC) device, in which analyte retention can be manipulated electrochemically. The second approach aimed at obtaining a high throughput of information by the simultaneous detection of multiple species. It targets the development of a multi-analyte immunoassay detection scheme using surface enhanced Raman spectroscopy (SERS) and labeled gold colloids in "biochip" format.

LC-on-a-Chip

This project couples the well-known analysis capabilities of LC instrumentation with opportunities for miniaturization using micromachining techniques for integration of the key functional components (i.e., column, detector, pump, and injector) onto a chip-scale platform. Miniaturized pump and valves based on electrochemically controlled mercury surface tension changes were constructed, chip scale LC columns were fabricated, and separations of two fluorescent dyes were demonstrated in this project.

The first phase of this project involved the construction and testing of mercury-based small fluidic controlling components, such as pump and valves. The pumping principle relies on the electrochemically-induced changes in surface tension at the

mercury/electrolyte interface, which is translated into a piston-like actuation of the mercury column. Chapter 1 summarizes the development of such pumps.

The mercury pump was also reconfigured to function in a valve format by incorporating a glass piston into the pump. Here, mercury actuation induces movement of the piston, which can be adjusted by varying the mercury surface tension through changes in applied potential. The extent of the displacement of the piston opens, closes, or partially opens the flow channel, altering the fluid flow rate. The performance characterizations and applications to flow injection analysis are given in Chapter 2.

The second portion of this project targeted at the design and fabrication of chip-scale LC columns as well as demonstrating the use of these columns for separation purposes. This work, part of which was done in a collaboration with micromachining experts at the Jet Propulsion Laboratory, has produced several small diameter (20-1000 μm) flow channels in different types of substrates, such as glass, silicon, glassy carbon and polydimethylsiloxane (PDMS), and with different cross section shapes. Two fluorescent dyes were successfully separated within some of these channels in an open tubular liquid chromatography (OTLC) format.

Encouraged by the separation results obtained with the OTLC columns, a chip for electrochemically modulated liquid chromatography (EMLC) was constructed by depositing a thin layer of gold or carbon at the bottom of the glass trench, as working electrode and stationary phase. The auxiliary and reference electrodes were also integrated inside the flow channel in a dual-comb arrangement. We showed that the analyte retention was controlled by varying the applied voltage on the working electrode in such a system. In addition, we found that modifying the gold surface with different self-assembled monolayers also changed the separation behavior, as a resulted flow rate and stationary phase differences. These results were detailed in Chapter 3.

Multianalyte Readout Scheme

Instead of reducing the size of analytical instruments, this project takes the approach of increasing the readout capability of conventional instrumentation to increase information output from a single address of a biochip. It focuses on the development of an immunoassay readout system, which exploits the SERS signal from reporter molecules that are co-immobilized with biospecific species on gold colloids. The narrow width of the Raman bands and the rich chemical information in a Raman spectrum offer an opportunity to distinguish several different species simultaneously.

The first effort of this project concentrated on the demonstration of a simultaneous multianalyte detection concept by using different Raman reporters in conjunction with different detection antibodies. Two molecules were picked as reporters because of their strong spectral intensity and minimal spectral overlap. The detection reagent was then prepared by conjugating antibodies to the reporter-labeled gold colloids. The concept was demonstrated in a dual-analyte sandwich immunoassay. We show in Chapter 4 that by using two different labels with little spectral overlap, two antigenic species could be detected simultaneously on a biochip.

In Chapter 5, this work was extended to a focus on obtaining quantitative immunoassay results. Two different types of extrinsically labeled Raman-active immunogold were compared in terms of reagent stability, sensitivity, and specificity. One relied on the co-immobilization of antibodies and reporter molecules directly on the same gold colloid; the other was based on the covalent linking of antibodies to the colloids via functionalized reporter molecules. The covalently linked immunogold reagent demonstrated an improved specificity and reproducibility in assay.

Prospectus

The presented work opens two research fields within our group: microfluidics and Raman spectroscopy. Like every new concept, it offers a great opportunity of exploration, and there are still many things can be done to further the work.

For example, current work demonstrates the concept of using the integrated mercury-based pump and valves for controlled fluid delivery. However, a stand alone micropump/valve does not offer much more benefits than the commercially available small pumps offered by Lee Company. The strength of novel types of micropumps, therefore, lies on its compatibility in the integration with other microcomponents, such as microchannels and microdetectors. Due to the limited access to fabrication facilities, the mercury pump developed so far is only "meso-scale" in size. So in order for it to be integrated with other microcomponents, this mercury-based fluidic delivery system needs to be further miniaturized to micron dimensions. In theory, the "downscaling" of the pump/valve to this size will result a system whose performance matches the needs (e.g., pressure and flow rate) of microfluidic devices.

Perhaps the most promising aspect in this work is the potential application of the described microfluidic channels to combinatorial liquid chromatographic devices. For example, coating the inner walls of an array of microfluidic channels with a thin film of gold and flowing different thiol-containing modifiers into different channels, will form different monolayer-based stationary phases in the microchannel array. This microfluidic array can then be used to analyze a sample mixture under different chromatographic conditions simultaneously. By extension, combinatorial EMLC analyses can be performed by adding a set of electrodes to the microchannels and controlling the voltage applied to each electrode. In this device, separation can perform simultaneously on stationary phases of same chemical composition but with different surface charge densities. Both types of devices will

be able to increase the analysis throughput by performing combinatorial analysis using microfluidic arrays.

The SERS active immunogold reagent described in Chapter 4 and 5 may have the potential to be developed into a standard immunoreagent for research and clinical uses, as an addition to the widely exploited fluorescent-tagged immunoreagents. The stability and specificity of these reagents as well as the sensitivity of the technique still needs to be assessed using more complicated, real working samples. Other types of Raman labels with strong signal intensity but minimum spectral overlap need to be identified in order to detect many more species simultaneously, therefore increasing the readout throughput.

In summary, I believe the microfluidic and the SERS-base immunoassay are two promising research topics that merit further exploration. The success in either field could eventually benefit areas such as drug discovery, disease diagnosis, and environmental monitoring.